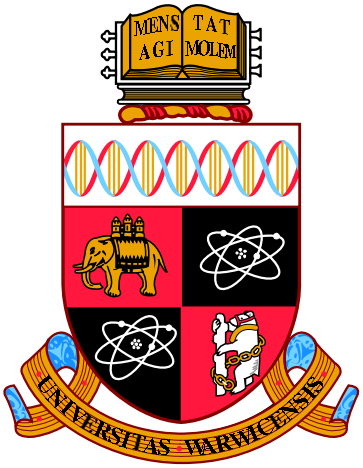


# High-Sensitivity Eddy-Current Testing Technology for Defect Detection in Aerospace Superalloys

by

**Robert R. Hughes**

**Thesis**

Submitted to the University of Warwick

for the degree of

**Engineering Doctorate**

**The Department of Physics**

October 2015

THE UNIVERSITY OF WARWICK

# Contents

# List of Tables

# List of Figures

# Acknowledgments

I would like to dedicate this thesis to coffee, without whom none of this would have been possible. I would also like to thank the following for their support and contributions to the work herein.

From the University of Warwick: Tobias Ericsson for his assistance in the tedious task of taking the probability of detection (PoD) measurements while I went for job interviews. Yichao Fan for his advice and technical support in the development of the NERSE experimental setup and the design and manufacture of in-house eddy-current probes. Rachel Edwards for her thorough and encouragingly ruthless feedback on reports and thesis drafts. And Steve Dixon for his unwavering support, guidance and frank words of encouragement throughout the EngD.

From Rolls-Royce plc, Aerospace NDE Lab, I wish to thank: Gian-Luca Piroddi for his assistance in characterising eddy-current arrays. Kit Lane for his infallible industrial support, practical advice and encouragement throughout. Tony Dunhill for the funding, passion and enthusiasm he had for the work I carried out. And Chris Batten for his advice and lessons on eddy-current probe design.

I would also like to thank Jethro Coulson for supplying the SRAS grain boundary data and always being up for a pint on EngD courses.

Final thanks go to my family and friends for their encouragement, support and assistance, throughout my EngD. Without their continued support I would have slipped another few rungs on the ladder toward sanity.

Please Note: If it wasn't for the Rugby World Cup, this would have been finished many weeks earlier.

# Declarations

I, Robert Hughes, do declare that the work presented in this thesis is my original research. Every effort is made to clearly indicate where contributions from others were involved, with due reference to the literature, and acknowledgement of collaborative research and discussions. The work was performed under the guidance of: Prof. Steve Dixon from the Department of Physics, at the University of Warwick, and Dr. Kit Lane, NDE Lab, Rolls-Royce plc., during the period between October 2011 and September 2015.

No part of this work has been previously submitted to the University of Warwick, or any other academic institution, for the admission to a higher degree. Some of the work has already appeared in the forms of publications, and those are listed below.

**Published Papers**

- R. Hughes and S. Dixon, *Developments in Near Electrical Resonance Signal Enhancement (NERSE) Eddy-Current Methods*, AIP Conference Proceedings, Vol. 1650, 2015, Pages 345-352

- R. Hughes and S. Dixon, *Near Electrical Resonance Signal Enhancement (NERSE) For Sub-Millimetre Detection In Aerospace Superalloys*, International Journal of Aerospace and Lightweight Structures (IJALS), Vol. 4, No. 2, 2014, Pages 107-120.

- R. Hughes, Y. Fan, and S. Dixon, *Near Electrical Resonance Signal Enhancement (NERSE) in Eddy-Current Crack Detection*, NDT & E International,

Vol. 66, 2014, Pages 82-89

- R. Hughes and S. Dixon, *Eddy-Current Crack Detection at Frequencies Approaching Electrical Resonance*, AIP Conference Proceedings, Vol. 1581, 2014, Pages 1366-1373

**Submitted Papers**

- R. Hughes, Y. Fan, and S. Dixon, *Investigating Electrical Resonance in Eddy-Current Array Probes*, AIP Conference Proceedings, A Review of Quantitative Non-Destructive Evaluation (QNDE), Minneapolis, MN, July 2015.

# Abstract

Industrial eddy-current testing (ECT) inspections of aerospace superalloys, such as Titanium 6Al-4V, must reliably detect sub-millimetre surface breaking defects. The sensitivity of such measurements is hindered by the materials' low conductivity and high coherent background material noise, making the high sensitivity standards required by industry harder to achieve.

It is demonstrated herein that using eddy-current array (ECA) technology also introduces inspection "blind-spots", whereby small defects could be missed. This supports the motivation to develop techniques for enhancing the sensitivity of typical ECT and ECA measurements. The early stage research and development of a novel ECT measurement method is presented, and shown to improve the standard measurement sensitivity of industrial ECT inspections.

A defect signal enhancement phenomenon within a band of frequencies close to the electrical resonance of an ECT probe, termed near electrical resonance signal enhancement (NERSE), was observed and characterised. This phenomenon was demonstrated to be a direct result of the shifting resonant frequency of the probe in the presence of material discontinuities.

Frequency sweeping chirp signals were used to generate electrical resonance traversing frequency spectra measurements of the inspection probe in the presence of material discontinuities. Critical feature analysis of the results demonstrated a correlation between defect dimensions and peak NERSE amplitude, but failed to draw any conclusive trends between discontinuity dimensions and the resonant frequency shift. This was attributed to the relatively small defect sample set used and the size of many of the machined defects being smaller than the diameter of the inspection coil.

An ECT probe was excited at a single frequency carefully selected to correspond to the NERSE peak frequency. A study was performed to statistically analysis the sensitivity of this NERSE measurement compared to a standard excitation frequency measurement used in industry. The results demonstrated that a NERSE frequency inspection was able to reliably detect a defect size of 0.82 mm, compared to 1.09 mm achieved by a standard operating frequency.

# Abbreviations

NDT = Non-Destructive Testing

NDE = Non-Destructive Evaluation

EC = Eddy-Current

ECT = Eddy-Current Testing

ECA = Eddy-Current Array

PEC = Pulsed Eddy-Current

UT = Ultrasonic Testing

PoD = Probability of Detection

NER = Near Electrical Resonance

NERSE = Near Electrical Resonance Signal Enhancement

RF = Radio Frequency

AC = Alternating Current

DC = Direct Current

HVM = High Value Manufacturing

FE = Finite Element

Ti6-4 = Titanium 6Al-4V

# Chapter 1

# Introduction

## 1.1 Nomenclature

Below is a list of some of the common symbols used within this thesis. Vectors are represented in bold and scalars are in plain text.

$t$ = Time $(s)$

$f$ = Frequency $(Hz)$

$\omega = 2\pi f$ = Angular frequency $(rad \cdot s^{-1})$

$\varepsilon = \varepsilon_r \varepsilon_0$ = Permittivity $(Fm^{-1})$

$\varepsilon_r$ = Relative Permittivity

$\varepsilon_0$= Permittivity of free space $(Fm^{-1})$

$\mu = \mu_r \mu_0$ = Permeability $(Hm^{-1})$

$\mu_r$ = Relative Permeability

$\mu_0$ = Permeability of free space $(Hm^{-1})$

$\sigma$ = Conductivity $(Sm^{-1})$

$\rho = 1/\sigma$= Resistivity $(\Omega m)$

$\mathbf{A}$ = Magnetic Vector Potential $(Vsm^{-1})$

$\mathbf{H}$ = Magnetic field $(Am^{-1})$

$\mathbf{B} = \nabla \times \mathbf{A} = \mu\mathbf{H}$ = Magnetic flux density $(T)$

$\mathbf{E}$ = Electric field $(Vm^{-1})$

$\mathbf{D} = \varepsilon\mathbf{E}$= Electric displacement Field $(Cm^{-1})$

$\mathbf{J} = \sigma\mathbf{E}$= Current Density $(Am^{-2})$

$R$ = Resistance $(\Omega)$

$L$ = Inductance $(H)$

$C$ = Capacitance $(F)$

$i = \sqrt{-1}$ = Complex number

$Z$ = Impedance $(\Omega)$

$X = \Im\{Z\}$ = Reactance $(\Omega)$

## 1.2 Motivation

High strength superalloys are used to make safety critical industrial components that are routinely subjected to intense stresses, strains and extreme environments. Jet engine turbine components are a perfect example, whose mechanical failure can come at significant financial and human cost [3, 4, 5, 6]. Development engineers carefully design these components so as to minimise failures, thus ensuring its economic viability and increasing its service life [7]. However, if left unchecked, even very small discontinuities within these structures could result in disastrous consequences. This leaves engineers with the important challenge of locating and detecting small defects before they can propagate and become critical. This must be done without compromising the functionality of the components, and so, are therefore inspected using methods from the field of non-destructive testing (NDT).

There are many NDT techniques to choose from when inspecting for defects. Each has its advantages and disadvantages that will determine its suitability for a certain type of inspection. Some inspections are purely surface techniques (dye penetrant, eddy-current testing, and magnetic particle inspection) whereas others can

probe the bulk of the material (ultrasonics and radiography). Many factors must be considered when choosing a technique. Foremost amongst these are the location and dimensions of the cracks being inspected which ultimately determines the minimum resolution required of the inspection. Other limiting factors include; cost, speed of inspection, ease of use, type of indications produced and any material limitations (e.g. material conductivity or grain structure) [8].

Eddy current testing (ECT) is used for the surface and near surface inspection of jet engine components made of high strength superalloys such as Titanium 6Al-4V (Ti6-4), a workhorse material of the aerospace industry. High inspection standards for these safety-critical components stipulate that the techniques used must achieve certain threshold sensitivities. However, advances in manufacturing design (single part components with complex geometry), microstructure, electrical anisotropy and defect growth counter measures (shot-peening and coatings) have made reaching these sensitivity targets more complicated [9, 10, 11]. As a result, the limits of traditional ECT inspection sensitivity are being reached, and so more advanced methods must be explored in order to meet the sensitivity requirements set by industry.

In addition, there is an increasing trend towards the use of multiple ECT coil elements in eddy current array (ECA) probes in order to improve inspection speeds. However, array probes often compromise on sensitivity in favour of coverage.

The aim of this EngD project is to:

1. Understand the limitations of typical ECA probe designs and operating modes so as to assist in the development of high sensitivity inspection techniques for complex jet engine components.

2. Investigate the application of novel eddy-current measurement techniques on aerospace superalloy materials in an effort to develop improved sensitivity to surface breaking cracks.

## 1.3 Non-Destructive Testing (NDT)

Many industry sectors, such as energy and aerospace, depend on the reliable performance of material components. The failure of one of these components can be costly and even cause a halt to normal operations resulting in a significant financial toll on the company while the failure is identified and fixed. There are two main maintenance approaches that can be employed by industry to mitigate the costs of critical component failure. They are, corrective (fixing components when they fail) or preventative (routine inspection of component quality). The approach applied to any given component is dependent on many factors to do with the cost of manufacture and impact a components failure would have on the sectors operations. Non-destructive testing (NDT) is the general name given to a field of engineering methods that can be used to evaluate a component's quality or structural integrity without impairing it's future use. NDT is an essential preventative tool in the manufacture and maintenance of high risk and high cost industrial components, otherwise known as high value manufacturing (HVM). There are numerous techniques that can be used to inspect critical HVM parts depending on the requirements and limitations of the application. In the following section the main NDT techniques implemented in the Aerospace industry are summarised along with their benefits and limitations.

## 1.4 Review of NDT Techniques

There are a whole range of NDT techniques that can be used to inspect components. Each has their own advantages and disadvantages of use depending on the type of inspection required, and so rarely will one technique be used alone to inspect a component. Instead multiple techniques are used to compliment one another so that a complete evaluation of a component can be made. What follows is a brief overview of the some of the most common methods in industrial NDT, detailing their benefits and limitations.

### 1.4.1 Visual and Optical Inspection

Visual inspection counts as the oldest, simplest and therefore most widely used NDT method around [7]. It involves the direct visual examination of a part or object to see if there is any visible signs of damage. It is therefore often the cheapest inspection available to NDT engineers. It is used every day in a range of different contexts, from checking food quality standards before they are sold in shops to inspecting the outside of an aircraft before take-off. They all use a form of visual inspection. However, due to the inherently subjective nature of visual inspection, the technique requires special training and validation of inspectors to ensure that a reliable standard of inspection is performed [8, 12]. As a result visual inspections are more often used as a guide for other NDT methods in identifying areas where potential degradation may have occurred but where further analysis is required to evaluate the extent of the damage. In the case of dye penetrant inspection however, visual inspection is used to locate and measure defects from this method (see section 1.4.2).

One of the disadvantages of visual inspection, which is common across many NDT techniques, is ease of access to the surface. There are many more advanced techniques derived from direct visual inspection, making use of optical aids such as mirrors, lenses, microscopes, borescopes and digital cameras that can be used to solve these issues [12].

More recent research and development has lead to other optical methods such as shearography (or shearing interferometry) whereby a coherent light source is reflected off the surface of a material through an interferometer lens system to provide information about the vibrational behaviour of the component which changes with load and the presence of defects [13].

The main disadvantages of visual inspection are that the inspection is only capable of identifying surface damage. For some component surfaces this may require some preparation such as cleaning or coating removal. Visual inspection also

struggles to identify hairline fractures and is better suited to large area damage.

### 1.4.2 Penetrant Testing

Penetrant testing is a widely used NDT method for locating and sizing surface-breaking defects [8]. In the aerospace industry, typical tests involve the application of a fluorescent liquid dye to the surface of a sample, which seeps into any surface-breaking cracks via capillary action. The excess dye is removed and a developer is then used to draw the liquid from the crack and the sample is examined under appropriate lighting (i.e. UV light for fluorescent penetrants) to locate and size cracks [12]. Penetrant testing is sensitive to small surface breaking cracks of all orientations and is unconfined by the properties of the material or its geometry. Large areas can be inspected relatively rapidly using penetrant testing and deliver an accurate indication of the size and shape of cracks (Figure 1.1).

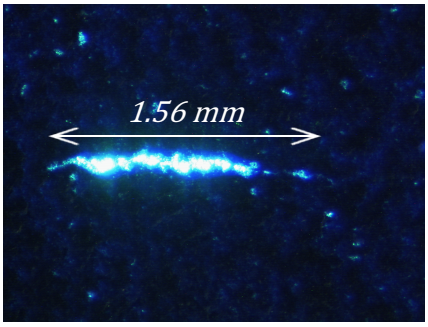


Figure 1.1: Fluorescent Dye penetrant crack indication in Nickel alloy bar [Rolls-Royce plc. NDE lab stock photo].

However, penetrant testing has its limitations. It is unable to detect non-surface-breaking cracks and does not give information as to the extent or shape of the crack within the bulk of the material. It is also inefficient at detecting closed or partially-closed discontinuities which can lead to misrepresentation of the full extent of the defect.

Penetrant testing requires the removal of any coatings and the component surface must be thoroughly cleaned or sometimes etched before the inspection can

take place. Such preparations prolong the length of time the component is out-of-service and make the process more expensive. The reliability and sensitivity of penetrant testing is often dependant on the precise application and careful storage and treatment of the penetrant chemicals.

### 1.4.3 Thermography

Thermography is used in the aerospace industry for the rapid inspection of large areas. There area a number of methods for performing thermography measurements however the basic principle involves heating a component's surface using flash lamps, hot-air guns or sometimes eddy-current heating, and then using infra-red cameras to measure the heat dissipation as a function of time after initial heating. The rate of dissipation depends on the thermal properties of the material being inspected as well as the component structure. Defects, such as cracks or voids in a material form an insulating air gap within the parent material, slowing the dissipation of heat in that region and trapping heat at the surface for a longer period. This appears as a localised "hot-spot" on the infra-red image of the surface and signal-analysis can be performed on the time-domain infra-red images to investigate the rate of dissipation and phase of hot-spots within an inspection. The deeper the defect is, the longer it will take for the heat to dissipate from the surface and reach the defect. This can be used to calculate the depth of defects [12, 14, 15, 16].

Thermography inspections are dependant on the area of the discontinuity parallel to the heated surface. Tight cracks perpendicular to the surface of thermal excitation will not obstruct the diffusion of heat down into the material and are unlikely to be detected [17]. Although technically a non-contact technique, test samples often require a dark coating to be added so that the heat is absorbed by the material and not reflected from the surface [18]. Depending on the test material, high frame rate infra-red cameras may be needed in order to capture the rapid diffusion of heat. These systems often require liquid nitrogen cooling and are therefore very

expensive [12, 16].

### 1.4.4 Ultrasonic Testing (UT)

UT inspections can be performed *in situ* and are capable of detecting discontinuities in both the surface and bulk of components [19]. There are multiple methods for generating and detecting ultrasound in materials; piezoelectric transducers, laser ultrasonics and Electromagnetic Acoustic Transducers (EMATs) being the most commonly used [19, 20, 21, 22].

Piezoelectric transducers use piezoelectric elements that will mechanically vibrate when supplied with a voltage impulse and will similarly generate a voltage response when they mechanically vibrate. In this way piezoelectric-transducers are used to transmit and receive vibrations into and from a material. However, piezoelectric transduction UT is traditionally limited by its need for direct contact with the sample, often requiring a coupling layer between the transducer and the test material [22]. As a result, contact conditions can be highly variable, reducing repeatability and making rapid inspections prone to error. Contact transducers are not suitable for inspections in extreme environments or where insulating coatings protect the component [22, 23].

EMATs generate and detect ultrasound in conducting materials through electromagnetic induction, and so do not require direct contact with the material. This makes EMATs suitable for high speed, repeatable inspections, and for inspections in hostile environments or through coatings and rough surfaces [23]. However, EMATs suffer from a comparatively low generation and detection efficiency compared to piezoelectric transducers [21]. This is in part due to the stand-off from the component surface which rapidly reduces the electromagnetic coupling required for ultrasonic generation and detection. Although, contact is not necessary for ultrasonic generation, EMATs must still be within a few millimetres for electromagnetic induction to take place.

Another non-contact ultrasonic technique is laser UT. There are two laser UT generation regimes, thermoelastic and ablation. The former uses a high-power laser impulse to locally heat a point on the surface causing sudden thermal expansion and relaxation, thereby generating ultrasonic pulses within the material. The ablation method locally heats the material beyond its boiling point, evaporating a small amount of material, and generating ultrasound by the recoil effect of the material loss [19, 24]. The frequency content of the ultrasonic waves is dependant on the generation regime. Ultrasonic detection can be done by measuring the displacement of the material using a number of methods including laser interferometry. For further details on the exact mechanisms of laser UT generation and detection the reader is directed to Scruby and Drain [24]. Laser UT is a high resolution technique that does not require material contact. However, the limitations are that the material surfaces must often be highly polished for sensitive ultrasonic detection, and the laser systems are often expensive and carry certain safety considerations with them.

UT techniques are sensitive to both surface and sub-surface flaws, and can be used to inspect large areas with a single probe [25]. Many authors have demonstrated the use of surface ultrasonic waves for the detection of surface defects [20, 26, 27]. UT bulk wave inspections are capable of resolving defects of sizes equivalent to the wavelength of the ultrasound generated. Reducing the wavelength (increasing the frequency) will therefore allow a greater sensitivity to smaller features, but ultrasound becomes highly attenuated as the wavelength tends towards the grain size of the material (or fibre layup in composite materials) [22, 28]. Many high strength, super alloys used in industry such as Inconel, Waspaloy and Titanium 6Al-4V, have coarse grain structures, leading to greater attenuation of higher frequency ultrasonic signals, thus limiting the smallest defects detectable [7]. High strength alloys are frequently used in safety critical components, and in harsh environments, such as turbine blades in jet engines [29, 30]. These materials are also often treated

by processes such as shot peening or burnishing which generates a layer of residual stress within the surface that will allow cracks to close themselves. Ultrasound can be transmitted through closed cracks [28] making the detection of very tight defects even more difficult.

### 1.4.5 Radiography

One of the most widely used and revealing NDT techniques is Radiography. Penetrating radiation (X-ray or gamma-ray) is directed at a specimen and developed on film or imaged on a sensor after having passed through the target sample. The intensity of the radiation is attenuated by its passage through the material leading to reduced irradiation of the developing film. The result is a two-dimensional intensity profile related to the density of the material that the radiation passed through. Cracks are equivalent to a reduction in the amount of material the radiation travels through, and thus show up as a darker region to the surrounding material (i.e. more radiation gets through leading to greater exposure). Radiographic images are often produced for multiple orientations of the component to fully characterize any defects. The contrast between defects and the surrounding material allows the operator to accurately locate, classify (i.e. porosity, crack, inclusion etc.) and size defects [8, 31].

Although Radiography is capable of accurately detecting and sizing defects anywhere within a specimen, it is dependant on the orientation of the defects. Defects in plane with the radiation propagation can go undetected. The highly penetrating radiation is also a considerable health risk. Radiographic NDT must therefore be performed in strictly controlled environments where safety is the key concern. While *in situ* inspections can be performed using radiography, the practicality is limited by safety regulations. As such, most inspections are performed in shielded rooms to protect operators during inspection. Any specimen being inspected must first be dismantled and transported to the radiographic room which,

along with other safety precautions, makes Radiography a relatively expensive technique.

### 1.4.6 Magnetic Flux Leakage (MFL)

Magnetic flux leakage (MFL) is an electromagnetic technique whereby a uniform magnetic field is applied to a magnetically permeable test material. This can be done with a permanent magnet or electromagnet. Discontinuities obstructing the magnetic flux lines within the test material cause the flux contained within it to find other routes around the discontinuity and so cause the magnetic flux to leak out of the surface. A diagram of how MFL works is shown in figure 1.2.

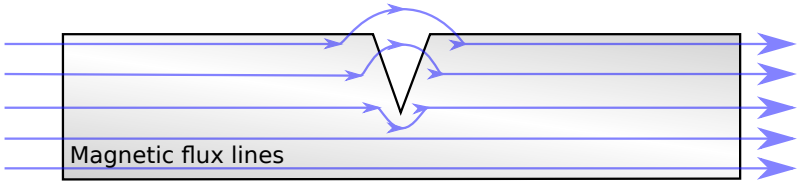


Figure 1.2: Magnetic flux leakage diagram showing magnetic flux lines within a magnetically permeable test material containing a surface defect.

The magnetic flux that leaks out of the surface can be detected either with a magnetic field sensor i.e. inductive coil, hall effect sensor etc (see section 2.3) [32], or using magnetic particle fluids which contain ferromagnetic particles in solution which are attracted to the leaked field. The latter method is known as magnetic particle inspection (MPI). MFL measurement methods are limited to ferromagnetic and magnetically permeable materials and is only capable of detecting near surface discontinuities orientated perpendicular to the direction of magnetic flux [8, 12, 33].

### 1.4.7 Eddy-Current Testing (ECT)

ECT techniques offer an attractive alternative for the surface inspection of high strength alloys. ECT is a very repeatable, non-contact inspection technique, which is highly sensitive to small surface, near-surface and under-coating discontinuities in

electrically conducting materials. ECT uses a similar principle of electromagnetic induction to EMATs to measure the electrical properties of the test material, and as such the technique is not subject to the variable contact conditions experienced by piezoelectric UT [19]. Eddy-current technology is relatively cheap compared to many of the other NDT inspection methods discussed above. However, ECT techniques do have their disadvantages. They are limited to the inspection of electrically conducting materials, are highly sensitive to variations in lift-off (distance between the probe tip and the surface of the test material) and tilt of the probe, and can be inefficient at detecting closed or partially contacting cracks. This is a common issue for many NDT including X-ray, UT and penetrant inspections.

ECT works by supplying a coil with alternating current while positioned above an electrically conducting material, thereby inducing localised electrical charge flow (eddy-currents) within the surface of the material (figure 3.1). The mutual interaction between the magnetic fields of the eddy-currents and the coil can be measured via the electrical properties of the coil and will change when the eddy-currents are obstructed by a discontinuity [34, 35]. While UT inspection techniques often require sophisticated analysis to extract defect positions from complicated time-traces [36], ECT only detects surface or near surface discontinuities[1] directly beneath the probe, which makes locating defects straight-forward. ECT gives an immediate quantitative indication of defect size and position during inspection which can also be used to size defects [37]. However, single probe inspections of large areas can be time consuming to perform. Due to the localized nature of the generated eddy-currents, the probe must scan over the whole of the whole inspection surface. Arrays of eddy current elements (see section 2.2.3 can be used to achieve greater coverage thus allowing larger areas to be scanned in one sweep, further increasing the speed of inspection [38]. Although highly sensitive to small defects, ECT inspections are limited to surface and near-surface inspections due to the skin-effect

[1] ECT measurements are also capable of detecting defects beneath coatings.

(see section 3.3) [39] which is dependant on the material conductivity, permeability and the frequency of excitation.

## 1.5 Summary

In this chapter the main NDT techniques were presented and their advantages and disadvantages discussed. Due to the high quality standards required, ECT methods are commonly relied upon for the surface inspection of safety critical superalloys in the aerospace industry. However, the uptake of more advanced ECT methods within industry has been poor over the past decade, and the sensitivity limits of these techniques are plateauing. Developments, and industrial interest, in multi-coil, arrayed eddy-current probes has provided the ideal opportunity for a critical examination of ECT/ECA technique sensitivity and the development of more advanced, higher-sensitivity eddy-current techniques.

The following chapter discusses the field of eddy-current testing in greater detail and highlights key areas of research and development.

# Chapter 2

# Eddy-Current Techniques

## 2.1 Introduction

Eddy-current inspection measurements can be performed using a wide variety of probe designs and operational techniques. The basic principles for performing an ECT inspection require the measurement of the secondary magnetic field generated by the eddy-currents in the inspection material. In this chapter a detailed explanation and review of the main ECT measurement probes and methods is presented. The latest advances in novel ECT research methods are also highlighted where appropriate and a summary of the relevant properties for the ECT inspection of the material of interest, Titanium 6Al-4V (Ti6-4), are detailed.

Due to the many variations of ECT inspection methods for different inspection geometries, materials and defect properties, this chapter will concentrate predominately on reviewing surface inspection methods for detecting surface breaking defects on nominally flat, non-ferromagnetic materials.

## 2.2 Electromagnetic Coils

The first ECT inspections used electromagnetic coils to generate and detect eddy-currents in the surface of materials. These simple probes are still most commonly

used method of inducing eddy-currents in a test specimen and for measuring their magnetic fields. This is due to coils offering good sensitivity at high frequency at low cost. There are many different types and approaches to consider when designing an electromagnetic coil ECT inspection, the most significant of which are presented in the following sections.

### 2.2.1 Coil Design

The size, shape, material backing and drive frequency of a coil all affect the eddy-current density profile generated within the test material and will influence how sensitive the probe is to defects. When a coil is energized above a conducting materials surface, localized eddy-currents are induced within the footprint of the wire. Larger coil footprints offer a greater area of coverage at the expense of defect sensitivity [42]. Figure 2.1 shows schematic, top-down diagrams of three different coil designs (spiral pancake, solenoid, and meander). Also shown are cross-sectional views of the coils above a conductive material surface, the corresponding mirror eddy-current flow and the magnitude of eddy-current density at a constant depth $z$, $|J_e|_{z=const}$, as a function of radial surface distance (x-direction).

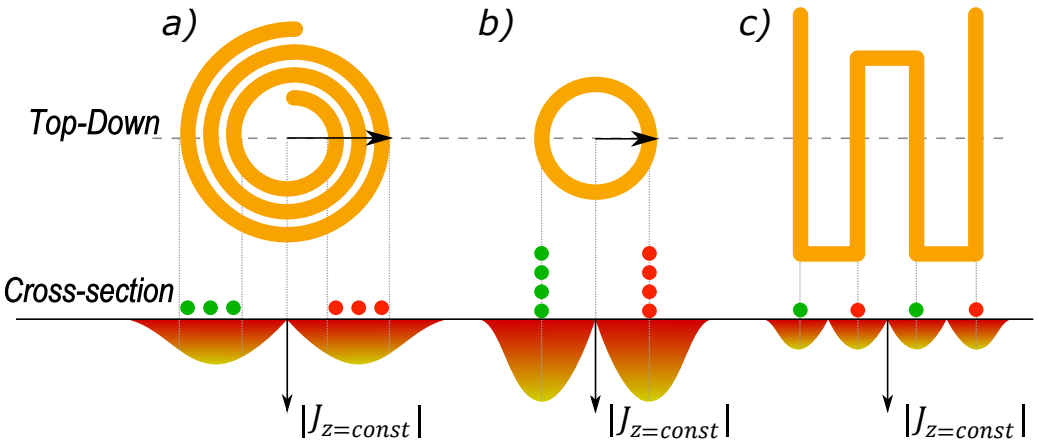


Figure 2.1: Top down and cross-sectional diagrams of three eddy-current coil designs with eddy-current density at a constant depth $|J_e|_{z=const}$ as a function of position beneath the coil. a) Spiral pancake coil, b) Solenoid coil and c) Meander coil.

### Solenoid-Type Coils

Solenoid coils have their axis perpendicular to the surface of the test sample. Solenoid coils are cylindrical turns of wire, often a few layers thick. They generate strong magnetic fields in their footprint, producing high eddy-current densities in the material directly beneath the coil turns and thus exhibit good signal strength (figure 2.1.b). Solenoids are therefore very sensitive to small cracks. Solenoid coils are ordinarily very sensitive to tilt and lift-off (see figure 2.2) from the material surface which are the major contributors to noise in EC surface inspections [43].

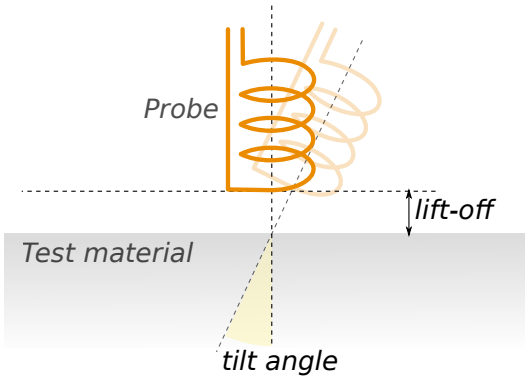


Figure 2.2: Diagram of probe position relative to the surface of the test material.

Solenoid-type coils are commonly used as encircling probes where they are wrapped around or within test bars or tubes. The encircling probe generates ECs in the azimuthal direction of the sample bar axis, making them sensitive to discontinuities parallel to the axis of the coil but insensitive to defects orientated circumferentially. Pipes are often inspected for internal damage using encircling coils pulled through the interior [44]. The inductance of a simple solenoid coil of $N$ turns, cross-sectional area $A$ and axial length $l$, can be estimated using the equation [45],

$$L = \mu \frac{N^2 A}{l} \tag{2.1}$$

where $\mu$ is the magnetic permeability of the coil core.

### Pancake-Type Coils

Pancake coils also have their axis perpendicular to the surface of the sample, but are wound in flat spirals as shown in figure 2.1.a. They offer better coverage than solenoids but suffer a loss in intensity of eddy-current density, resulting in reduced signal strength. The increased coverage of pancake coils, compared with solenoid coils, also comes at the cost of spatial resolution [42]. Depending on the coil size, if a small crack (smaller than the footprint of the coil) is picked up by a spiral coil it cannot be determined exactly where within the footprint the defect will be.

### Rectangular coils

In the past decade the use of rectangular coils in ECT has increased [38, 46, 47]. Their directional properties and ability to generate uniform EC distributions makes them an attractive option for certain inspections. Rectangular coils also offer good sensitivity to scratches and other minor surface damage, as well as being easily manufactured by printed circuit techniques [47]. One innovative approach to EC inspection using rectangular coils has been pioneered by the company Jentek Sensors Inc. [48]. A transmit-receive probe (see section 2.2.3) floods a relatively large area of test material with eddy currents by generating a spatially periodic magnetic field. This is achieved using a single primary meander coil (figure 2.1.c) excited with alternating current. Rectangular receiver coils, closely following the loops of the primary coil, pick up any changes in the magnetic field due to discontinuities [48, 49, 50]. The simple design of the coils makes it easy to model the system and provides a much larger effective dipole giving better insensitivity to lift-off. However, due to their low turn number, much higher currents must be used in order to achieve appropriate coupling to the material.

**Ferrite Cores**

The sensitivity of an ECT coil is dependent on the inductance, $L$, of the coil, which can be raised significantly by using a core with a high magnetic permeability ($\mu$). Ferrites are ceramic compounds of iron oxides, which are ferrimagnetic but non-conductive. These can be used as coil cores offering a very high permeability, even at high frequencies, unlike iron or steel. Their low conductivities, many orders of magnitude less than that of metals, suppress the generation of eddy-currents within the ferrite [45]. Higher permeability cores concentrate the magnetic flux of the coil, promoting greater flux linkage between the coil and the material, which improves lift-off sensitivity and the dynamic range of the probe [51]. Ferrites are even effective when used as a backing to pancake-type coils [52].

Low core conductivity is important for reducing losses within a core. Eddy-currents and magnetic hysteresis are key mechanisms of loss represented by an imaginary component of impedance [51]. When designing ECT coils with ferrite cores it is important to select a ferrite material that has a small imaginary component of permeability at the frequencies being operated at, so as to minimise losses. However, the complex permeability is also dependent on the dimensions of the material [53] such that the apparent permeability of smaller cores can be significantly different from that of a larger core. This dimensional effect is caused by the combination of intrinsic permeability and permittivity. All of these factors make modelling and determining the complex permeability of ferrite cores complicated, with many authors carrying out research in the area [53, 54, 55, 56, 57, 58].

### 2.2.2 Coil Sensitivity

In NDT it is often important to be able to accurately evaluate the size of defects. Janousek et al. [59] describe a novel ECT approach for sizing defects, using two probes generating differing eddy-current distributions in order to gain increased dimensional information. Ramos et al. [60] looked at manipulating the depth of

penetration to characterise defect depths, and Yusa et al. [61] have developed a method of extending the ECT sensitivity to defects much deeper than the depth of penetration making it possible to distinguish between EC signals from defects of different depths. Yusa et al. [61] use coils perpendicular and parallel to the material surface in conjunction to send and receive eddy-currents respectively. The set up reportedly overcomes some of the limitations of conventional ECT. For typical ECT inspections in the aerospace industry, a high risk component will fail an inspection if any defects are detected above a pre-determined detection threshold. It is therefore vital to use highly sensitive inspections for these components.

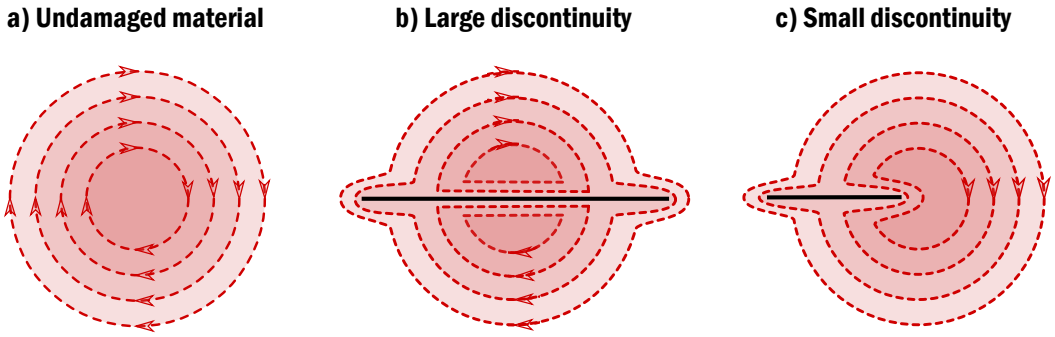


Figure 2.3: Simplified eddy current flow in material surface when a) No defect is present, b) a deep defect greater than the diameter of the coil is present, c) a defect smaller than the diameter of the coil is present, and d) a defect smaller than the diameter of the coil and parallel to the flow of current.

It should be noted that defects smaller than the size of the probe will produce double peaked defect indications as demonstrated in figure 2.4.

One of the main limits of ECT sensitivity is the coil size. When eddy-currents encounter a crack comparable to the diameter of their circular path they are forced to find a new path around or under the defect. Any cracks smaller than this diameter can be directly beneath the coil and still leave the eddy-currents relatively unperturbed therefore producing negligible signal (figure 2.3.c). The sensitivity is also orientation dependent. A defect smaller than the diameter of the coil offers less of an obstacle to the flow of current so will only perturb the flow slightly (figure 2.3).

The greatest defect signals are achieved when the defect offers the greatest obstruction to current flow i.e. when the crack axis is perpendicular to the flow of current. This is the ultimate physical limit of many ECT probes. Uchanin [62] demonstrated that spatial changes occurred in ECT signals along long defects and highlighted the need for ECT coils to be smaller than the target defect size.

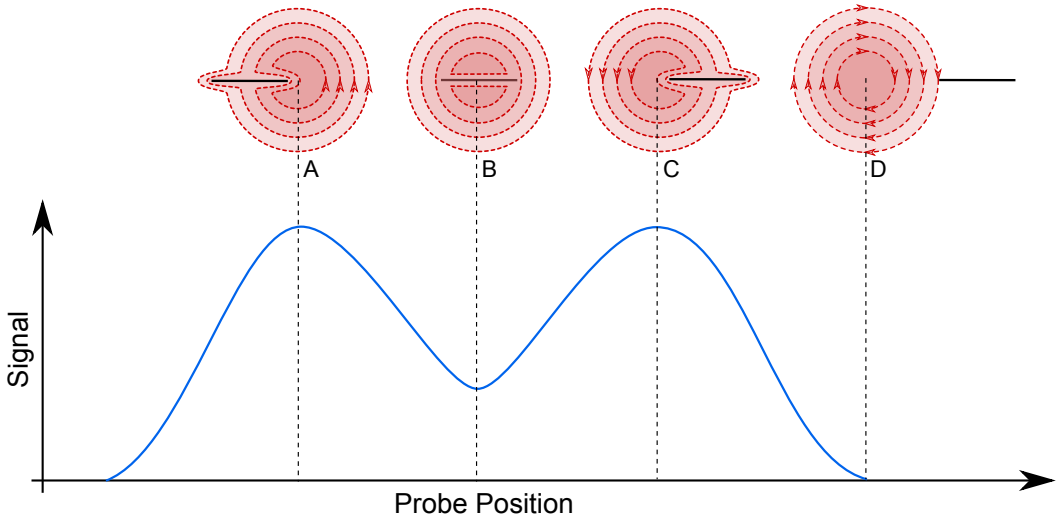


Figure 2.4: Representation of eddy-current measurement of a defect smaller than the diameter of the coil showing the equivalent signal response at four positions. The result is a double peak signal.

### 2.2.3 Mode of Operation

There are a number of different measurements that can be made with electromagnetic coil probes, depending on the purpose or limitations of the application. The main measurement techniques commonly implemented are summarised in the following sections.

#### Absolute (Reflection) Probe

Absolute (sometimes called Double-function, or reflection) probes use a single coil to generate and detect the ECs in the test specimen (figure 2.5.a). This is the most basic and most common mode of operation of an EC probe and is the mode that

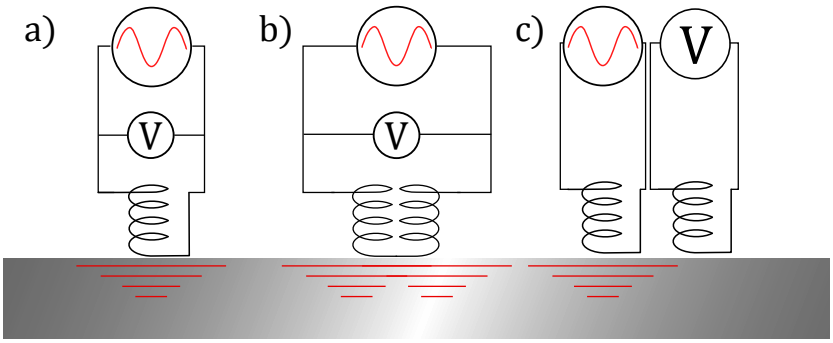


Figure 2.5: Circuit configurations for three modes of operation for EC probes, a) Absolute, b) Differential and c) Transmit-Receive, after [64].

has been used to explain the fundamental concept of ECT so far in this report. The output of the probe is the absolute voltage across the coil, which changes in the presence of a defect. However, this configuration is highly sensitive to variations in temperature. Absolute-mode probes are often used in conjunction with a reference coil removed from the inspection area. The reference coil is designed to have the same impedance in air as the inspection coil and to compensate the voltage so as to reduce fluctuations from changes in local temperature (see figure 2.7.a). For perfectly matched inspection and reference coils, the system will return zero voltage when there is no defect, thereby enhancing the dynamic range and thus the probes sensitivity to defects [44]. This approach is a form of differential probe (see section 2.2.3).

### Differential Probe

Differential probes measure the voltage difference between the voltages of two coils inspecting adjacent sections of a test specimen (figure 2.5.b). They can be wound as two separate coils and their absolute voltages subtracted post inspection, or wound as a single circuit of two coils with opposing direction turns. The latter probe configuration equalizes the induced voltage due to the primary excitation field, resulting in zero output in the absence of a defect. Differential probes can be

used as double-function probes or as passive sensor coils to a separate excitation coil in a separate-function probe. Differential probes are highly sensitive to small defects but can be insensitive to long defects (i.e. if both coils sense the defect and therefore cancel the signal out). They are very stable, relatively lift-off insensitive, probes, offering less noise and allowing higher sensitivity to smaller signals, but can be insensitive to defects of certain orientations [45].

### Transmit-Receive Probe

Transmit-receive or separated-function probes use one coil to excite eddy-currents and another (or a few others) as a passive detector of the EC response (figure 2.5.c). The benefit of separated-function probes is that the generation and detection coils can each be optimized separately to enhance the sensitivity of the probe, whereas absolute probes require a compromise between strong, uniform EC generation, good coverage and sensitivity to defects.

### Array Probes

One of the major disadvantages of single coil operation is the time it takes to scan a two-dimensional surface. Eddy-current arrays (ECAs) can significantly reduce this inspection time by increasing the area covered in a single scan [70]. ECAs comprise a number of identical, uniformly spaced sensing elements which are scanned across a surface to inspect large areas quickly. Array elements can be driven in any of the modes above, dependent on the type of defect being sought. It is then a matter of multiplexing between elements (or groups of elements) in turn to electronically scan through all the elements of the array. Multiplexing is performed in a pattern so as to avoid the detrimental effects of cross-talk experienced between adjacent elements being simultaneously driven. Many authors have seen the benefits of ECAs and have striven to improve both probe design and post-processing defect characterisation [38, 48, 70, 71]. In more recent years conformable ECAs have been developed to

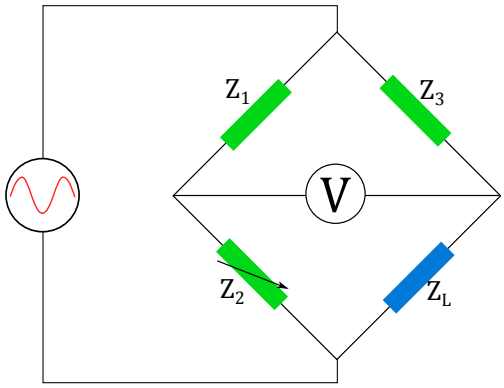


Figure 2.6: Schematic of a Wheatstone impedance bridge showing two fixed impedance components ($Z_1$ & $Z_3$), one variable impedance component ($Z_2$) and the load component ($Z_L$).

achieve enhanced coverage for the inspection of complex and inaccessible surfaces by manufacturing printed circuit coils [48, 72, 73].

### 2.2.4 Eddy-Current Instrumentation

Electromagnetic coils can be integrated into sensitive measurement circuits that can be adapted for the specific application being considered.

Bridges are a frequently-used method of achieving relatively stable ECT inspections. There are many different types of bridge that can be implemented, the aims of which are to balance the impedance of the probe coil over undamaged specimens, producing a very accurate difference measurement in response to defects. A basic bridge is composed of two circuit arms each containing components for impeding the flow of current (figure 2.6). One arm comprises components of known impedance ($Z_1$ and $Z_2$) and the other contains one component of known impedance, $Z_3$, and another is the unknown ECT coil ($Z_L$).

The voltage difference between the two arms will be zero if the total impedances of each arm are equal, otherwise a voltage difference is observed. The system can be tuned to balance the unknown arm by varying $Z_2$ in the known-arm (i.e. variable resistor, comparable inductor or reference coil). The aim of such bridges is

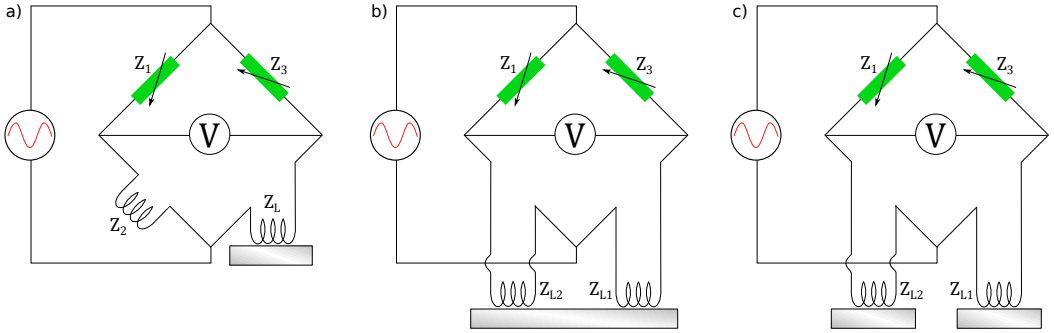


Figure 2.7: Schematic diagrams of impedance bridge types for eddy-current inspection measurements showing a) Absolute, b) Differential and c) External reference measurement configurations.

to balance the probe when it is over undamaged material, improving the dynamic sensing range of the system and increasing sensitivity to defects [45]. The use of a bridge introduces an analogue difference measurement which can be highly sensitive to defects whilst being unaffected by variations in the surrounding environment.

Eddy-current measurements are frequently performed with the use of a balancing reference coil as the $Z_2$ component in figure 2.6. This is typically of a matching inductance to the inspection coil and can be implemented in a number of ways. Figure 2.7 shows the most common eddy-current measurement circuits of this sort (see section 2.2.3 for information on their advantages).

### 2.2.5 Eddy-Current Excitation

Electromagnetic coil probes generate and detect eddy-currents by the principles of Amperes' and Faradays' Laws (see chapter 3). As a result they require a changing excitation field to generate and detect magnetic fields. The simplest excitation is a continuous monotonic sinusoidal waveform, however there are many other more advanced methods of making ECT measurements.

**Multi-Frequency Measurements**

Standard ECT inspections use a single frequency technique where the coil is driven at a fixed sinusoidal frequency. High frequency ECT operations are limited by the skin depth to detecting small surface defects. However, it is often desirable to achieve greater sub-surface detection with ECT inspections. One solution would be to lower the excitation frequency thereby increasing the depth of penetration, but this method comes with a reduction in the sensitivity to the smaller surface defects as current can pass underneath. In addition, Faradays law states that induced voltages are proportional to the rate of change of the magnetic field which will decrease with decreasing frequency.

More information can be acquired if multiple frequencies are used to generate eddy-currents flowing at different depths [75]. Different discontinuity properties (lift-off, temperature variation etc.) lead to different phase angles in signals which can be identified by experienced users when observed independently (see figure 2.9). Problems arise when multiple discontinuity properties are present in a single defect signal leading to a more complicated signal with increased noise. It is often the case that multiple unwanted factors are present in the signals of real defects. Multi-frequency techniques perform successive tests at two or more frequencies that, when combined, will cancel out the undesirable signals, hence improving the signal-to-noise-ratio (SNR) [42, 45, 76].

Bartels and Fisher [77] investigated using the linear summation of both real and imaginary components of impedance of a four frequency inspection in order to gain greater SNR. This approach combines both the magnitude and phase information of 2D impedance images and the authors claimed to improve the SNR by up to 1100% compared to traditional two-frequency techniques. There are many techniques for performing multi-frequency ECT inspections, including separate sinusoidal excitation of two or more frequencies, frequency sweeping and pulse excitation [44].

**Pulsed Eddy-Current (PEC)**

Pulsed ECT, sometimes referred to as transient ECT involves the excitation of a broad band of eddy-current frequencies by applying a voltage pulse to the excitation coil and measuring the time-domain response of the material to signals can be used to excite a broad spectrum of frequencies, providing many levels of material penetration and thus more information than simpler single frequency techniques. The data across multiple frequencies can be correlated, as per other multi-frequency techniques, to remove unwanted signals, making the characterization of defects easier than with other methods. The spectrum of frequencies scales inversely with the pulse length, so shorter pulses generate a wider range of frequencies [44, 45]. PEC

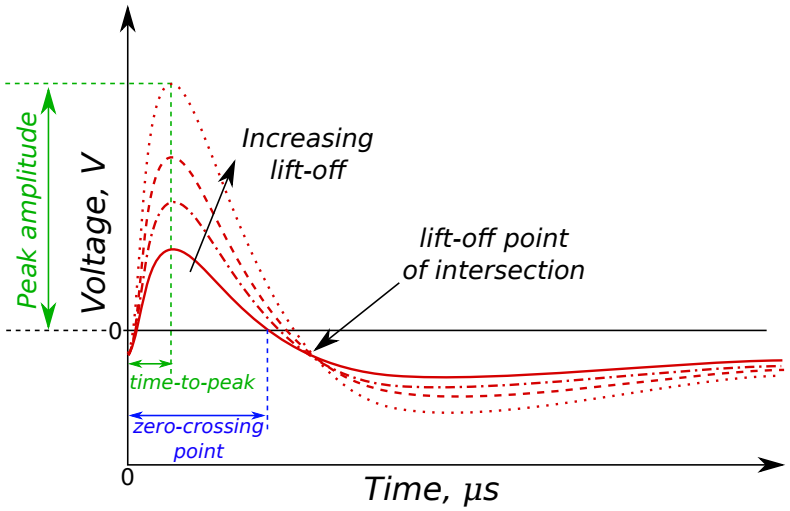


Figure 2.8: Example pulsed eddy-current signal responses in the time domain showing responses at various lift-offs from the material. Showing lift-off point of intersection, peak amplitude, time-to-peak and zero-crossing point, after [85, 86].

techniques predominately analyse the critical features of signal response in the time-domain (figre 2.8), such as the peak amplitude, time-to-peak, zero crossing-point and the lift-off point of intersection. Giguare et al. [85] performed investigations into pulsed ECT as a means of lift-off compensation known as Lift-Off Invariance (LOI). LOI is based on the observation that there occurs a point in the time domain

of received signals that is independent of lift-off, known as the cross-point. By measuring the signals within a time gate about the cross-point (figure 2.8), mapping of a material surface can be performed largely unaffected by variations in lift-off [87, 88]. However analysis of the time-domain signal is relatively sensitive to noise [82].

#### Chirp Excitation

Chirp excitation involves using a sinusoidal input function whose frequency linearly increases with time. The result is an input signal that sweeps through a range of frequencies in the time domain. The mathematical form of a chirp input is defined as,

$$s(t) = A(t)e^{i\omega(t)t}, \tag{2.2}$$

where $A(t)$ is the function envelope, and $\omega(t)$ is the time varying angular frequency [82]. Chirp measurement analysis of a signal response is typically made in the frequency domain. Chirp methods have widespread applications in radar systems [98, 99] but have had less attention in eddy-current testing research compared to pulsed and multi-frequency excitation.

## 2.3 Other Magnetic Field Sensors

In recent years, other methods for detecting and measuring the magnetic field of eddy-currents have seen increased attention due to their high sensitivity over large frequency ranges, and at lower frequencies than electromagnetic coils. These include giant magnetoresistors (GMR), superconducting quantum interference devices (SQUIDS) and Hall probes. Novkovski [101] outlines the main magnetic field sensors and discusses their suitability for use in nano-sensors in the pursuit of greater resolution.

### 2.3.1 Magneto-Resistors

Magneto-resistance (MR) is a quantum mechanical property of materials that exhibit changes in electrical resistance when subjected to an externally applied magnetic field. All conductors exhibit some MR properties but there are other materials that exhibit greater, anisotropic magneto-resistive (AMR) properties that can be used as magnetic field sensors for NDE applications [102, 103]. AMR properties are caused by changes in the scattering cross-section of the material brought about by an external magnetic field distorting the atomic electron orbitals [104].

Researchers have also been able to develop solid state devices with significantly larger MR properties known as giant magneto-resistors (GMRs). Smith et al. [105] and Dogaru and Smith [106] have demonstrated the use of GMRs as passive detectors for surface and near surface defect detection. GMRs have the advantage of being more sensitive at low frequencies than ECT coils because they measure the magnitude of the magnetic field instead of the change. GMR sensors can be made with small dimensions and due to their low power consumption can be configured into high density arrays on circuits of chips [105].

### 2.3.2 Superconducting Quantum Interference Device (SQUIDS)

High resolution magnetic field measurements can be achieved through using superconducting quantum interference devices (SQUIDs), which are capable of detecting very weak magnetic fields. SQUIDS are constructed from semi-circular loops of superconducting material connected via Josephson junctions [107]. However, they must be operated at cryogenic temperatures in order to decrease noise and maintain the probes superconducting state [101]. Authors such as Kreutzbruck et al. [108] have shown SQUIDs to be effective in distinguishing between defects and features of the material structure even in complex components such as a layered aluminium fuselage. Because of their very high sensitivity SQUIDs have also been used to aid in the solving of the inverse problem of defect-field interactions in 2D problems [109].

### 2.3.3 Hall probes

Hall probes or Hall-effect sensors are another method used for measuring the magnetic field of the eddy-currents. Classic Hall-effect probes measure the magnetic field by monitoring the changes in voltage across a current carrying conductor or semiconductor [110]. These vary as the magnetic field changes and the force upon the current fluctuates. As with GMRs, Hall probes are easily miniaturised but suffer from high levels of pink noise ($1/f$) [101] making their use at low frequencies less suitable. In spite of this, Hall-probes have been investigated as defect detectors. He et al. [94] investigated using a differential Hall probe to inspect defects in rivets with a pulsed eddy-current method but found that they offered no additional sensitivity improvements over conventional ECT differential probes.

Quantum Well Hall Effect (QWHE) sensors are another technique used that exploits the Hall effect observed in two-dimensional electron systems i.e. a gas of electrons with high mobility in two dimensions, but tightly confined in the third. This effect is observed in some semiconductor transistor-type junctions, where there exists a triangular quantum well in the conduction band which falls below the Fermi energy level allowing electron mobility parallel to the junction interface but not perpendicular to it, thus setting up an effective 2D electron gas which is then influenced by the presence of magnetic fields [111]. QWHE sensors typically exhibit greater sensitivity to their classical Hall-effect sensor counterparts [112].

## 2.4 Eddy-Current Signal Analysis

For single frequency excitation methods, defect signal responses are typically represented in what is known as a Lissajous (Foster, Argand or complex impedance plane) plot as shown in figure 2.9. The amplitude of the signal can be measured in a number of ways about the balance point. The balance point is the impedance of the probe on undamaged material. This is often used as the origin of the Lissajous

plot. The most common defect signal measurements, shown in figure 2.9 are:

1. Peak Magnitude - The distance from the balance point to the maximum point on the defect signal curve.

2. Peak-to-peak Magnitude - The distance between the minimum and the maximum points on the defect signal curve.

3. Peak Vertical Amplitude - The vertical height of the defect signal curve from the origin.

4. Peak-to-Peak Vertical Amplitude - The vertical height of the defect signal curve from the negative maximum to the positive maximum.

5. Phase angle - The angle between the defect signal curve and the horizontal axis.

One of the main problems with Magnitude (methods 1 & 2) measurements of ECT data is that it is phase insensitive. Taking the magnitude of a defect signal gives the maximum response along a particular phase, however, when a measurement of background noise is made using the same technique the peak magnitude of the noise may be in an entirely different orientation. It is therefore much more common to use phase sensitive techniques like the Vertical Amplitude measurements (methods 3 & 4). Often the impedance plane frame of reference is rotated around the signal such that any lift-off signals move along the horizontal axis. By then measuring the vertical height of the signals any potential lift-off noise is suppressed thereby improving the signal-to-noise of the inspection. The phase changes in ECT signals can also be used to provide a measure for changes in the material properties such as for corrosion or conductivity changes.

Typical ECT inspections use vertical height measurements to record defects and background signals after rotating the reference axis to force the lift-off signal

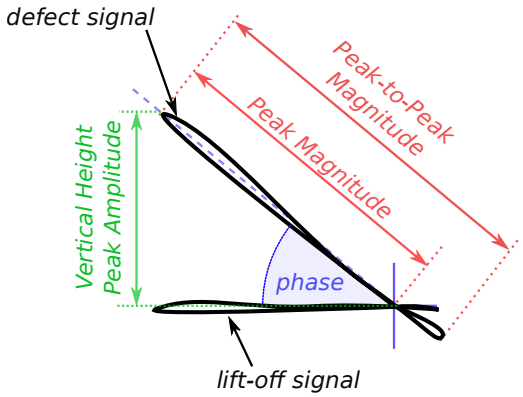


Figure 2.9: Lissajous (complex plane) plot of ECT defect signal showing the various measurements possible.

to zero. This is a simple approach which reduces the chances of background noise rising above a vertical threshold.

## 2.5 Inspection & Application Considerations

This sections summarises the main inspection considerations for the EC application considered in this thesis. The material application studied in this thesis is the ECT detection of sub-millimetre, surface breaking defects in Titanium 6Al-4V (Ti6-4). Ti6-4 is one of the most widely used superalloys in the aerospace industry, due to its high strength to weight ratio and corrosion resistance, but also happens to be one of the most demanding materials to inspect using non-destructive methods [113].

### 2.5.1 Frequency Selection

To begin with, Ti6-4 has one of the lowest electrical conductivities of any industrially-used metal. Typical values for the electrical and magnetic properties of Ti6-4 are $\sigma_{Ti(6-4)} = 0.60 \times 10^6\ Sm^{-1}$ and $\mu_{Ti(6-4)} = 1.00005$ respectively [11]. This means that the generation of eddy-currents within the material is inefficient and that the

standard depth of penetration, $\delta$, is deep. Using equation 3.31, which is,

$$\delta = \sqrt{\frac{2}{\omega\mu\sigma}}. \tag{2.3}$$

the value of $\delta$ is 0.38 mm at 3 MHz.

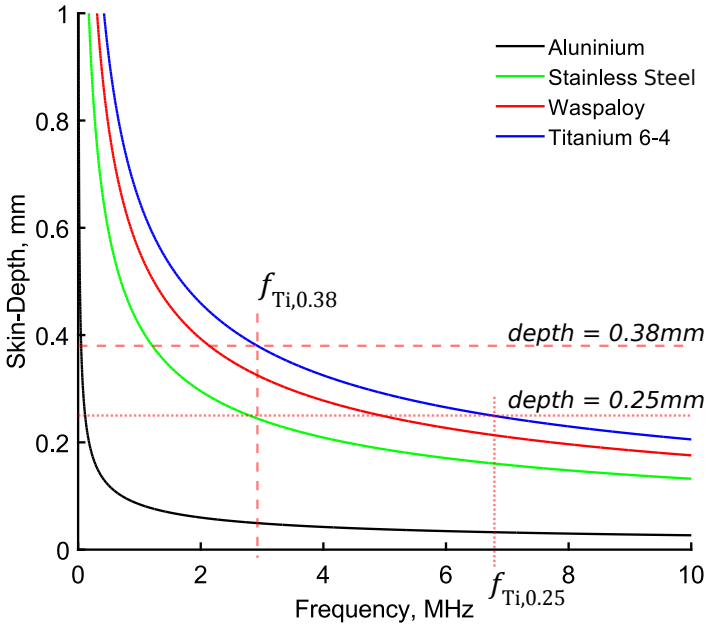


Figure 2.10: Calculated plane-wave skin-depth as a function of frequency for typical values of four industrial materials: Aluminium, Stainless Steel, Waspaloy and Titanium 6Al-4V.

A large $\delta$ is sometimes convenient when through-thickness measurements of plates are desired, however, traditional wisdom dictates that inspections for small surface defects should be performed at higher frequencies. This will reduce $\delta$ in order to confine the eddy-currents to a shallower surface layer (figure 2.10) [45]. Industrial ECT inspections for sub-mm defects, on Ti6-4, are therefore typically performed at frequencies between 1-3 MHz, corresponding to skin-depths of 0.65-0.38 mm respectively.

Operating at higher frequencies has its advantages. The sensitivity of the measurement probe increases due to Faraday and Ampere's laws (see section 3.2),

as seen by the linear relationship between the inductive reactance and frequency ($X = \omega L$). Increasing the frequency also improves the phase separation between lift-off and defect signals by moving the measurement along the conductivity curve shown by the red curve in figure 2.11.

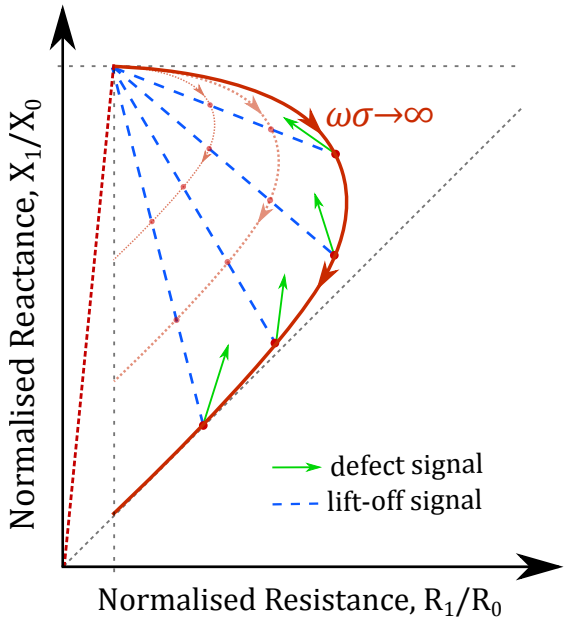


Figure 2.11: Example diagram of normalized impedance plane showing conductivity-frequency curve, lift-off and defect signal directions for a non-ferromagnetic material. After [44].

However, as shown by figure 2.10, greater frequency increases are required to reach shallower defect depth targets and the desired operating frequency would quickly reach into the tens of megahertz, well beyond the operating limits of most ECT systems.

Increasing the frequency also influences the choice of probe coil. High inductance, $L$, coils are desirable as they induce greater current density in the test material. However, large $L$ coils connected via a coaxial cable, of capacitance $C$, will have low electrical resonant frequencies (see section 3.7) as,

$$2\pi f_0 \approx \sqrt{\frac{1}{L_0 C_0}}. \tag{2.4}$$

Operating beyond resonance will give a measure of the capacitance of the cable in the system and is therefore impractical for measuring changes in the eddy-currents in the surface. The operating frequency for a given probe coil is therefore limited by the resonant frequency of the probe. In order to use higher operating frequencies the coil inductance or capacitance of the system must be decreased. Reducing the capacitance, i.e. shortening the cable, is not always practical, and reducing the inductance lowers the sensitivity which may not be made up by the frequency increase.

### 2.5.2 Material Noise in Ti6-4

Material noise is that produced by the inherent inhomogeneity of the test material, i.e. grain noise, electrical anisotropy or residual stress. This type of noise is spatially coherent, in that it is a feature of the material and so will be the same in every scan. It therefore cannot be eliminated from the measurement. Ti6-4 exhibits high material noise in ECT inspections due to its grain structure and the electrical anisotropy of its $\alpha$-phase crystal lattice [9, 114].

There are two main phases of Ti6-4, $\alpha$ and $\beta$, that have different crystal structures, hexagonal close-packed (HCP), and body centred cubic (BCC) respectively. The HCP form of Ti6-4 is typically the more dominant phase in industrial Ti6-4 and has the crystal structure shown in figure 2.12.a. HCP Ti6-4 is electrically isotropic in all orientations in the basal plane, $\rho = \rho_b$, but exhibits electrical anisotropy going from the basal plane along the c-axis, $\rho_c \neq \rho_b$ [9, 114] (figure 2.12.b). For pure titanium the resistivity is approximately 6% lower in the basal plane compared to along the c-axis [115].

This anisotropy is due to the interplaner electron mobility being impeded by atoms along the c-axes of the crystal. The directivity of the electrical resistivity of

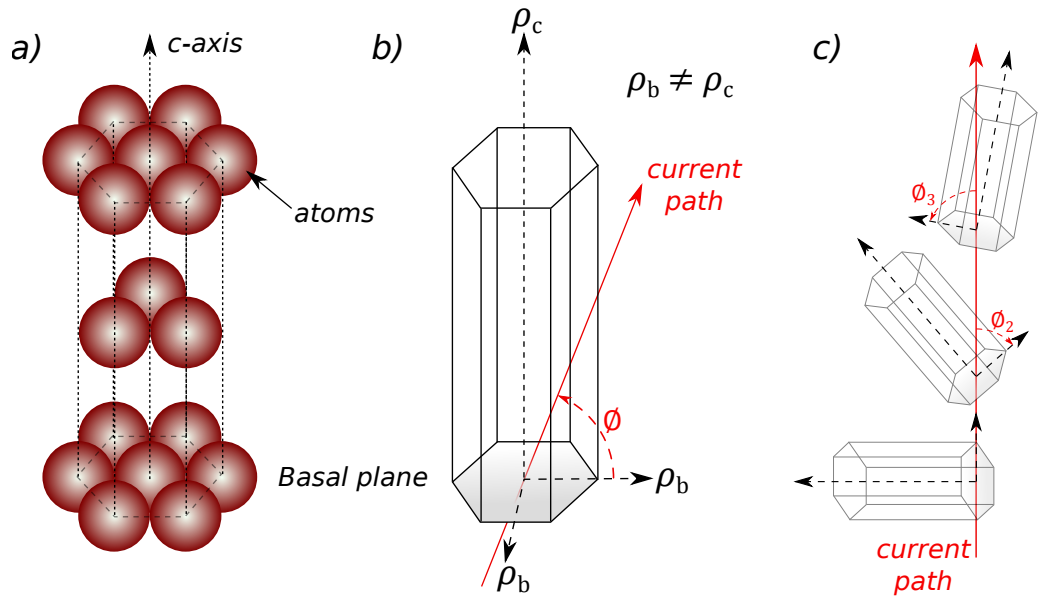


Figure 2.12: Diagram of hexagonal close-packed crystallographic structure showing: a) The crystal lattice structure, basal plane, and the c-axis. b) The resistivity anisotropy between the basal plane and the c-axis, and the current path angle with the basal plane. And c) the current path through randomly orientated crystal structures.

a HCP crystal can be represented by the function [116],

$$\rho(\phi) = \rho_c \sin^2 \phi + \rho_b \cos^2 \phi, \tag{2.5}$$

where $\phi$ is the angle between the direction of current flow and the basal plane. The resistivity measured along a current path passing through a number of grains of different crystal orientations (figure 2.12.c) will therefore be an average of different grain orientations along the current path.

Different grades and levels of thermal treatment of Ti6-4 can significantly change the material's grain structure and hence its physical properties. Annealing is used to optimise the structural properties, i.e. tensile strength or temperature tolerance, for a given application in the aerospace industry. However, heat treatment changes the grain structure of the material [117]. Grains form colonies of similarly

orientated grains and the size of those colonies vary through heat treatment. The grain boundaries represent an interface between crystals of different orientations and so eddy-currents are affected by the change in electrical conductivity at colony boundaries. The grain boundaries are discontinuities in the homogeneity of the crystal lattice and are, as such, the smallest material discontinuities possible.

For small grain colony sizes, the electrical anisotropy and grain boundary affects average out over a single ECT measurement such that the material will appear isotropic. However, as the grain colonies grow, these factors will have a greater influence on the ECT measurement such that macro-scale variations are observed in scans due to changes in the average resistivity of the eddy-current path, as documented by Blodgett and Nagy [116, 118]. Figure 2.13 shows ECT scan images of background noise associated with grain colonies in polycrystalline titanium alloys of different heat treatments. Other authors, such as Cherry et al. [119], have even used ECT measurements to detect grain boundaries in large grain Ti6-4 samples.

Another form of material noise occurs due to residual stress in the material surface. Residual stress can sometimes be desirable in aerospace applications as a way of preventing the propagation of surface breaking micro-cracks. There are a number of methods for inducing compressive residual stress in a material surface. One traditionally used in the aerospace industry is shot-peening where the surface is impacted with shot (commonly round ceramic or metallic particles) with enough force to produce plastic deformation in the surface layer [113]. The effect of an elastic stress on the surface is to make the conductivity slightly anisotropic [120].

As a result of these material factors, industrial Ti6-4 exhibits high levels of background noise compared to other materials (as shown in figure 2.14) which limits the detectable defect size of conventional ECT inspections on industrial Ti6-4. For this reason new approaches for enhancing the sensitivity of ECT inspections are investigated herein.

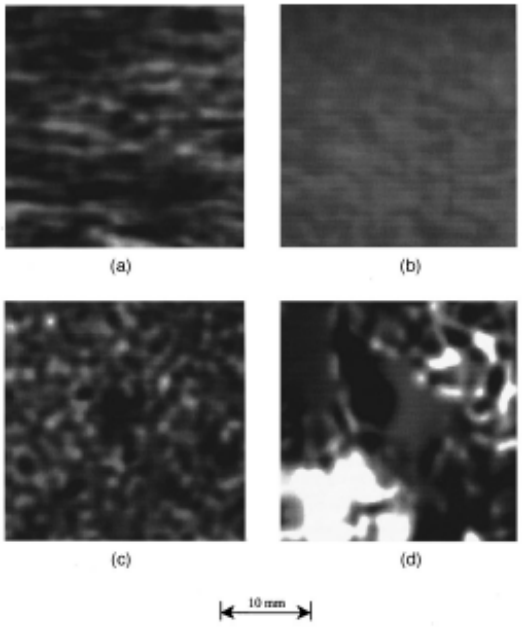


Figure 2.13: Examples of grain noise in 2MHz eddy-current scans of polycrystalline Titantium alloys. "Scanned eddy current images of different Ti-6Al-4V microstructures: a) the as received billet microstructure showing texture related features in the horizontal direction; b) solution treated and annealed very fine microstructure; c) equiaxed beta annealed microstructure; and d) heat-treated coarse grain structure with large colonies dimension 1×1 inch." From [116].

### 2.5.3 Inspection Noise

Inspection noise is that produced by physical instabilities or variations in the conditions of the inspection. Examples include variations in; probe lift-off, probe tilt, or temperature (see figure 2.2). This type of noise is also coherent, in that it is a physical feature of the system being measured. However, such variations can often be reduced by improving the control over the inspection and are typically of low spatial frequency such that spatial filtering can be applied to the resulting scan image to remove their effects.

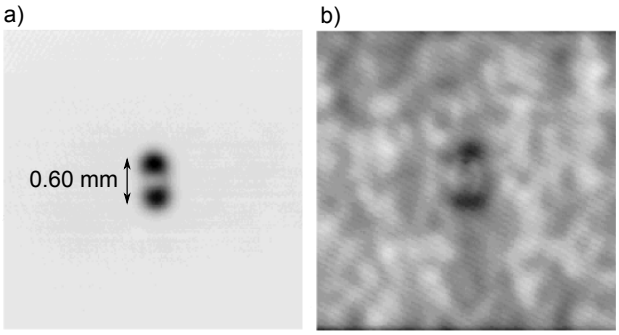


Figure 2.14: Examples of comparable ECT inspections of sub-millimetre fatigue defects in 2024 Aluminium (a) and Ti6-4 (b) at 2 MHz. From [121].

## 2.6 Summary

Due to the adverse properties of Ti6-4 for the detection of sub-millimetre surface defects, it is pertinent to develop methods of improving the sensitivity of ECT inspections for these applications. The core focus of the research presented in this thesis is in the pursuit of a more sensitive ECT inspection technique. Due to Ti6-4's low conductivity, high frequencies (>1 MHz) were investigated to constrain the eddy-currents to within 1.0 mm of the surface. Electromagnetic coils were selected as the most suitable sensor to work with due to their low cost, sensitivity at high frequencies and their wide use within industry.

# Chapter 3

# Eddy-Current Theory

## 3.1 Introduction

In this chapter the background theory behind eddy-current measurements are presented. EC probes are coils of wire (inductors) that generate time-varying magnetic fields when excited by an alternating current. Characteristic changes in the electrical properties of a coil occur when there is a change in the electrical properties of its surroundings [45]. A coil's response to these changes can be analysed to determine the cause of the signal, be it lift-off from the surface of a conductive sample, the presence of a material discontinuity, or any other change in the properties of the sample. The theory presented in this chapter is used later in the development of high sensitivity eddy-current techniques.

## 3.2 Electromagnetic Induction

Eddy-current measurements are based upon the principles of electromagnetic induction, whereby a time-varying magnetic flux will induce charge to flow within an electrically conducting material it is incident upon. The physical laws governing

these interactions are defined by Maxwell's equations, and are given as [110],

$$\nabla \cdot \mathbf{D} = \rho_f, \tag{3.1}$$

$$\nabla \cdot \mathbf{B} = 0, \tag{3.2}$$

$$\nabla \times \mathbf{E} = -\frac{\partial \mathbf{B}}{\partial t}, \tag{3.3}$$

$$\nabla \times \mathbf{H} = \mathbf{J_f} + \frac{\partial \mathbf{D}}{\partial t}. \tag{3.4}$$

In the above general expressions of Maxwell's equations, $\rho_f$ is the free charge density and $\mathbf{J_f}$ is the free current density. The second term in equation 3.4 is Maxwell's correction to Ampére's law and is referred to as the displacement current. Free current density and free charge density are related via the continuity equation,

$$\nabla \cdot \mathbf{J} = -\frac{\partial \rho}{\partial t}. \tag{3.5}$$

The free current density represents the density of charge flow and is approximated by Ohm's Law,

$$\mathbf{J_f} = \sigma \mathbf{E}. \tag{3.6}$$

An alternating current carrying wire will generate a dynamic (time-varying) magnetic field, $\mathbf{H} = \mathbf{B}/\mu$, in response to the rate of change of the electric field, $\mathbf{E} = \mathbf{D}/\varepsilon$, driving the current. The magnetic field expands and collapses in the direction perpendicular to the electric field as stated by Ampéres Law (equation 3.4). The curl (i.e. $\nabla \times \mathbf{H}$) is a vector potential operator denoting the infinitesimal rotation of a three-dimensional vector field. The curl of a rotating vector field is itself a vector field along the axis of rotation i.e. perpendicular.

These equations will be used to explain the principles of electromagnetic induction that govern eddy-current inspection techniques.

### 3.2.1 Self-Inductance

For a coil in free-space, i.e. not in the proximity of an external electrically conducting material, $\sigma = 0$, Ampére's law (equation 3.4) becomes,

$$\nabla \times \mathbf{H} = \mathbf{J_f} + \varepsilon \frac{\partial \mathbf{E}}{\partial t}. \tag{3.7}$$

Faradays law of electromagnetic induction (equation 3.3) states that a time-varying magnetic field, **H**, incident upon an electrically conducting material will induce an electric field within that media. The induced electric field generates currents which will always flow so as to generate a magnetic field (Ampéres law) which will oppose the change in magnetic flux which created it. Ampéres and Faradays Laws can be applied to an AC driven coil in free-space. When excited with an time-varying current, $I$, a dynamic magnetic field, **H**, forms around the coil (via Ampéres law, equation 3.7). Although the coil is in free space, the changing magnetic flux, $\phi_{\mathbf{B}}$, interacts with the coil turns, inducing a voltage across the inductor which opposes the rate of change of the primary current, $I$. This phenomenon is known as self-inductance and means that work must be done against a back electromotive force (emf), $V_{emf}$. Until the current is turned off, the work done against the back-emf can be thought of as energy stored in the magnetic field. In free space, the stored energy is a fixed, recoverable amount, which is returned when the current is turned off [110]. For a coil of $N$ turns in free-space the $V_{emf}$ is given by,

$$V_{emf} = -N \frac{\partial \phi_{\mathbf{B}}}{\partial t} = -L \frac{\partial \mathbf{I}}{\partial t}, \tag{3.8}$$

where $L$ is the coefficient of self-inductance. In simple terms, the coefficient of self-inductance, $L$, is a measure of a coil's ability to store energy in a magnetic field. ECT coils are often designed to have a high self-inductance in order to achieve higher sensitivity. The coefficient of self-inductance of a solenoid coil, constructed up of $N$

turns around a core of magnetic permeability $\mu$ and with a cross-sectional area $A$, and height $h$ can be approximately calculated using the equation [45],

$$L = \mu N^2 \frac{A}{h}. \tag{3.9}$$

Self-induced back-emf increases the total opposition to the flow of current, known as the electrical impedance, $Z = V/I$ (see section 3.6.1) [44].

### 3.2.2 Eddy-Current Induction

When an AC energized coil is in the proximity of an electrically conducting material ($\sigma > 0$), its changing magnetic flux penetrates the surface of the material (blue arrows in figure 3.1), thereby inducing the flow of electric charge in closed loops, known as eddy-currents, via Faradays law of induction (equation 3.3). Eddy-currents tend to flow perpendicular to the magnetic field that creates them, and in a direction so as to generate their own magnetic field (green arrows figure 3.1) which will oppose the changing magnetic field that created them. A current oscillating between $\pm I_0$ Amps, at a frequency $\omega = 2\pi f$ can be represented by the equation,

$$\mathbf{I(t)} = \mathbf{I_0} e^{i\omega t}. \tag{3.10}$$

An ideal coil with self-inductance in air, $L$, excited with current, $\mathbf{I_c}$, of the form in equation 3.10 will have an electrical potential, $\mathbf{E_c}$, that leads the current by $90^o$.

$$\mathbf{E_c} = -L\frac{\partial \mathbf{I_c}}{\partial t}, \tag{3.11}$$

$$= -i\omega L I_0 e^{i\omega t}, \tag{3.12}$$

$$= \omega L \mathbf{I_c} e^{-i\frac{\pi}{2}}. \tag{3.13}$$

A coil will generate a time-varying magnetic field ($\mathbf{H_c}$) perpendicular to the flow of current in the coil of wire conductivity, $\sigma_c$, as defined by Ampéres Law. The

magnetic field is dominated by the excitation current density, $\mathbf{J_c}$, in the coil,

$$\bigtriangledown \times \mathbf{H_c} = \mathbf{J_c} + \varepsilon \frac{\partial \mathbf{E_c}}{\partial t}, \tag{3.14}$$

$$\approx \sigma_c \mathbf{E_c}, \tag{3.15}$$

$$\approx -i\sigma_c \omega L \mathbf{I_c}. \tag{3.16}$$

As a result the magnetic field is approximately $-\pi$ out-of-phase from the excitation current. When in the proximity of an electrically conducting material the magnetic field will penetrate the surface of the material and, through Faradays law of electromagnetic induction, generate an induced electric field, $\mathbf{E_e}$, and thus cause the flow of electrical charge (eddy-currents).

$$\bigtriangledown \times \mathbf{E_e} = -\mu \frac{\partial \mathbf{H_c}}{\partial t}, \tag{3.17}$$

$$= -\mu\sigma_c \omega^2 L \mathbf{I_c}, \tag{3.18}$$

$$= -i\mu\sigma_c \omega \mathbf{E_c}. \tag{3.19}$$

Equation 3.19 shows that the induced electric field at the surface of a conducting material is out-of-phase with the generating electric field in the coil, $E_c$, by a value $\phi_0 = -\pi$.

The secondary magnetic field established by the flow of eddy-currents interacts with the coil, inducing additional current flow in the excitation coil. This changes the voltage required to push the same current through the coil, thus varying the coil impedance, $Z$. The interaction of the primary and secondary magnetic fields with the coil and the eddy-currents leads to a mutual-inductance, $M$, which is highly dependent on the separation between coil, material surface condition, and the self-inductance of the coil, $L$, (see section 3.7.3).

Eddy-currents flowing at a depth $z$ within the material will see the primary H-field partially shielded by the secondary H-fields of the eddy-currents above it.

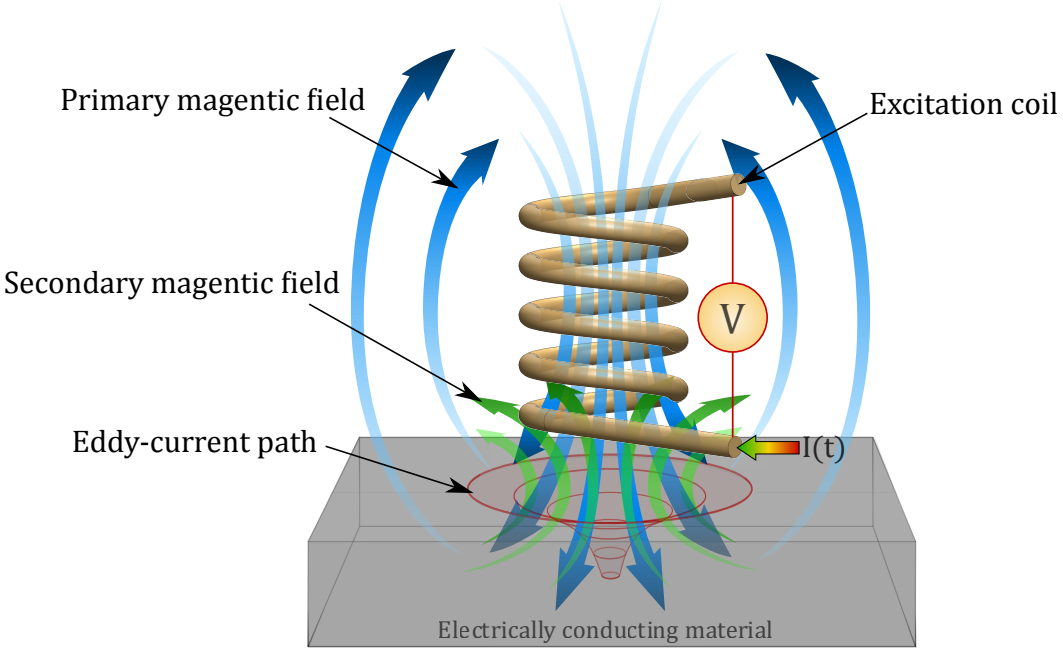


Figure 3.1: Induction of Eddy currents within a metal block by an ECT coil, after [44].

In this way the primary H-field seen within the conductor falls off rapidly with depth, and with it so does the current density it generates. Alternatively, this effect can be considered to be a result of attenuation of the electromagnetic (EM) fields as they propagate to greater depths as energy is dissipated by the generation of eddy-currents within the material. As a result the eddy-currents are confined to the surface of the material by this phenomenon known as the skin effect.

## 3.3 The Skin Effect

EC inspections are limited to the inspection of surfaces or thin sheets of material as determined by the standard depth of penetration, or skin-depth, $\delta$. This is due to the electromagnetic skin effect, whereby the amplitude of a non-DC current density decreases exponentially with depth. A derivation of the skin-depth is made below via the examination of the behaviour of propagating electromagnetic fields in electrically conducting materials.

### 3.3.1 Standard Depth of Penetration

For EM waves in a good conductor ($\sigma \gg \omega\epsilon$) the free charge density, $\rho_f$, dissipates to the surface of the material in a characteristic time ($\varepsilon/\sigma$) that is much faster than the period of excitation ($1/\omega$) [123]. This means that the displacement current, $\mathbf{D}$, is negligible compared to conduction current, $\mathbf{J_f}$, such that Maxwell's equations for EM waves in a conductor become,

$$\nabla \cdot \mathbf{D} = 0, \tag{3.20}$$

$$\nabla \cdot \mathbf{B} = 0, \tag{3.21}$$

$$\nabla \times \mathbf{E} = -\frac{\partial \mathbf{B}}{\partial t}, \tag{3.22}$$

$$\nabla \times \mathbf{H} = \mathbf{J_f}. \tag{3.23}$$

By applying the vector Laplacian relationship[1] to equations 3.22 & 3.23 and substituting in equations 3.6, 3.20 & 3.21, modified wave equations are obtained [124] for the electric and magnetic fields.

$$\nabla^2 \mathbf{E} - \mu\sigma \frac{\partial \mathbf{E}}{\partial t} = 0, \tag{3.24}$$

$$\nabla^2 \mathbf{H} - \mu\sigma \frac{\partial \mathbf{H}}{\partial t} = 0. \tag{3.25}$$

For the case of plane waves propagating in the $z$-direction the Laplacian operator in equations 3.24 & 3.25 becomes $\nabla^2 = \frac{\partial^2}{\partial z^2}$. Hence, complex plane wave solutions for waves propagating in the z-direction are,

$$\tilde{\mathbf{E}}(z,t) = \tilde{\mathbf{E}}_0 \exp i(\tilde{\gamma} z - \omega t), \tag{3.26}$$

$$\tilde{\mathbf{H}}(z,t) = \tilde{\mathbf{H}}_0 \exp i(\tilde{\gamma} z - \omega t + \frac{\pi}{2}), \tag{3.27}$$

[1] $\nabla^2 A = \nabla(\nabla \cdot A) - \nabla \times (\nabla \times A)$

where $\tilde{\gamma}$ is the complex propagation constant of the form $\alpha + i\beta$ which, by using solution 3.26 in wave equation 3.24 can be derived as,

$$\tilde{\gamma}^2 = i\omega\mu\sigma, \tag{3.28}$$

$$\tilde{\gamma} = \sqrt{i\omega\mu\sigma}, \tag{3.29}$$

$$\tilde{\gamma} = (1+i)\sqrt{\frac{\omega\mu\sigma}{2}}, \tag{3.30}$$

having used the identity $\sqrt{i} = (1+i)/\sqrt{2}$. The real ($\alpha$) and imaginary ($\beta$) components of $\tilde{\gamma}$ are referred to as the attenuation and phase constants respectively and are equal in magnitude for the case of a plane wave in a good conductor. The inverse of $\alpha$ or $\beta$ defines the material quantity, the standard depth of penetration,

$$\delta = \sqrt{\frac{2}{\omega\mu\sigma}}. \tag{3.31}$$

This value is the depth within the material at which the magnitude of the propagating field has decayed to $1/e$ ($\approx 37\%$) of it's original amplitude; however both the phase and amplitude vary with depth [39]. It is easy to see from equation 3.31 that the higher the excitation frequency, the shallower the penetration depth. Equally, higher conductivity or permeability materials also lead to shallower depths of penetration. It is for this reason that careful consideration must be made when it comes to selecting the excitation frequency of ECT inspections.

The resulting wave equations for the plane wave electric and magnetic fields in a conductor are therefore,

$$\tilde{\mathbf{E}}(z,t) = \tilde{\mathbf{E}}_0 \exp\left(-\frac{z}{\delta}\right) \exp\left(i(\omega t + \phi_0 - \frac{z}{\delta})\right), \tag{3.32}$$

$$\tilde{\mathbf{H}}(z,t) = \tilde{\mathbf{H}}_0 \exp\left(-\frac{z}{\delta}\right) \exp\left(i(\omega t + \phi_0 - \frac{z}{\delta})\right). \tag{3.33}$$

The first exponential term in equations 3.26 & 3.27 represent the decay in amplitude and the second exponential term includes an equivalent phase shifting term as a function of depth, $z$.

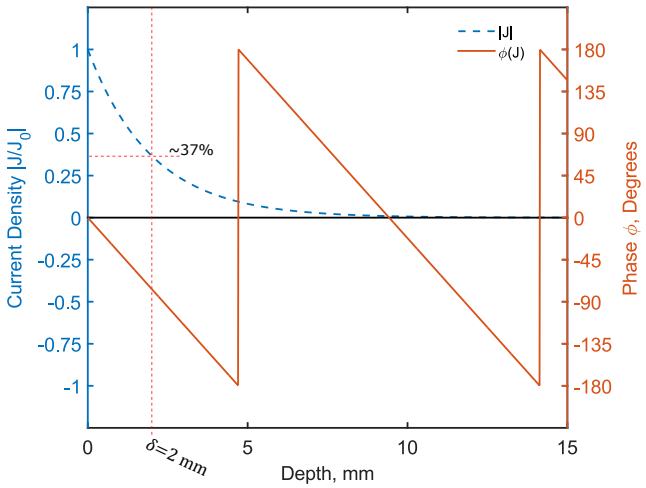


Figure 3.2: Current density depth profile: Decay of magnitude and change in phase of current density as a function of depth for plane wave excitation. The skin-depth is 2 mm and is shown in the plot (red dotted vertical line).

Using Ohm's law, the current density at a depth $z$ within a conductor supporting a plane EM wave can be expressed as,

$$\mathbf{J}(\mathbf{z},\mathbf{t}) = \sigma\mathbf{E} = \mathbf{J_0}\exp\left(-\frac{z}{\delta}\right)\exp\left(i(\omega t + \phi_0 - \frac{z}{\delta})\right), \tag{3.34}$$

$$= \mathbf{J_0}\exp\left(-\frac{z}{\delta}(1+i)\right)\exp i(\omega t + \phi_0), \tag{3.35}$$

where $\phi_0$ is the phase of the normalised current density, $\mathbf{J}(\mathbf{z},\mathbf{t})$, at the surface of the material, $z = 0$. Figure 3.2 illustrates the magnitude and phase of $\mathbf{J}$ as a function of depth into a material of characteristic skin-depth $\delta = 2mm$.

For the case of plane wave current generation, the eddy-currents can be considered to form a uniform current sheet at the surface. By considering a section of this current sheet of length $l$ and width $W$ (figure 3.3) the eddy-current density of equation 3.35 can be integrated over all depths to give the total current, $I$, within

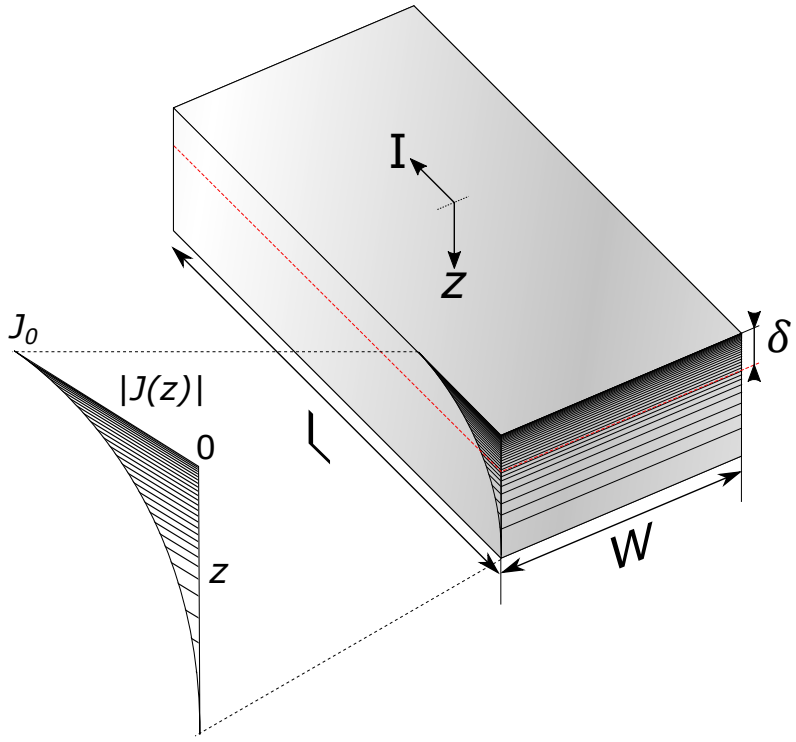


Figure 3.3: Diagram representing the skin effect in a slab section of a conducting half-space of electrically conducting material. After [39].

.

the material as shown in Wheeler [39].

$$\mathbf{I} = W \int_0^\infty \mathbf{J}(\mathbf{z}, \mathbf{t})\, dz, \tag{3.36}$$

$$= \mathbf{J}(\mathbf{z}, \mathbf{t}) W \frac{\delta}{2}(1 + i) \tag{3.37}$$

Equation 3.37 shows that the total current within the material is equivalent to a current with a phase shift of $-\pi/4$ from the surface phase, $\phi_0$. The impedance, $Z = V/I$, of a current sheet of length $l$ and width $W$, subject to an image current $I$, can be shown to be,

$$Z = (1 + i)\frac{l}{W}\frac{1}{\delta}\frac{E_e}{J_0 e^{i(\omega t + \phi_0)}}, \tag{3.38}$$

where $J = \sigma \mathbf{E_e}$ such that,

$$Z = (1 + i)\frac{l}{W}\frac{1}{\sigma\delta}, \tag{3.39}$$

and where $\rho$ is the material resistivity ($\rho = 1/\sigma$). For a plane wave excitation field, the resistive and reactive components of the complex impedance, $Z$, are both dependant on the skin-depth and are equal in magnitude, as shown by Wheeler [39]. For a section of the current sheet of unit length and width ($l = W = 1$) the intrinsic impedance, $\eta$, of the media is expressed as,

$$\eta = (1 + i)\frac{1}{\sigma\delta}. \tag{3.40}$$

The intrinsic, or surface, resistance and reactance (for unit $l$ and $W$) are therefore defined as,

$$R_1 = X_1 = \frac{1}{\sigma\delta}, \tag{3.41}$$

$$= \sqrt{\frac{\omega\mu}{2\sigma}}. \tag{3.42}$$

This demonstrates how both resistive and reactive components of the intrinsic impedance of a material are influenced by the skin-effect. The intrinsic impedance of a good conductor at high frequency is 45° ($\pi/4$) i.e. in most cases the magnetic field lags the electric field by 45° in a non-ferromagentic material [124].

The frequency will therefore influence an AC carrying wire at high frequencies. If the skin-depth for a given frequency, wire conductivity and permeability is smaller then the wire diameter than the current will be confined to a surface layer of the wire whose cross-sectional area is smaller than that of the whole wire (figure 3.4). Hence with increasing frequency the resistance of the wire will also increase. This is an important consideration when developing high frequency probes and models. The resistance of a wire of length, $l$, and diameter, $d$, is therefore,

$$R = X = \frac{l}{\pi d}\sqrt{\frac{\omega\mu}{2\sigma}}. \tag{3.43}$$

The skin-effect influences the test material as well as the conducting wire carrying

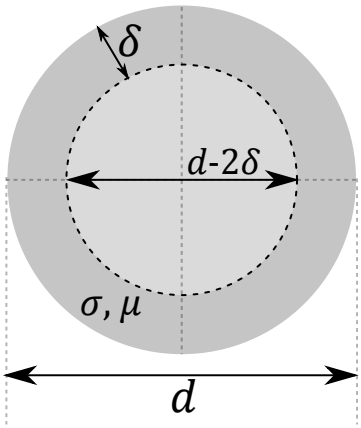


Figure 3.4: Wire cross-section diagram showing surface confinement of electrical current within a wire of diameter $d$ with electrical conductivity, $\sigma$ and magnetic permeability, $\mu$. After [39].

AC, by confining the current to a shallower skin-depth as the frequency increases. For the test material, the frequency of excitation can be selected dependent on the size and location of the defects being inspected for. For shallow surface defects, the frequency is typically increased until the skin-depth is comparable to the depth of the target defect. However, for most eddy-current applications, the excitation field is not a uniform plane wave, and so the behaviour of the fields and the eddy-currents will deviate from this idealised case.

### 3.3.2 Geometric Skin-Depth

The above results are true for plane wave excitation i.e. current in a wire or induced current from an infinitely large coil. In reality ECT coils are never infinitely large, but the larger the coil, the more like a uniform plane-wave field the magnetic field looks to the majority of the material beneath it. Practically speaking, ECT coils are rarely very large, especially for high sensitivity applications, as this thesis considers. As a result of this deviation from a uniform field, geometric effects must also be considered when determining the depth of penetration of a probe.

It is often convenient when considering the EM-fields around a coil to define

them in terms of the magnetic vector potential, $\mathbf{A}$, which can be defined, for a non-static electric field, by the following relationships,

$$\mathbf{B} = \nabla \times \mathbf{A}, \text{ and} \tag{3.44}$$

$$\mathbf{E} = -\frac{\partial \mathbf{A}}{\partial t}. \tag{3.45}$$

For an axially symmetric system of a single coil turn above a conducting half space (figure 3.6), the magnetic vector potential around the coil will vary with both radial distance, $r$, and distance, $z$, normal to the coil turn. This can be expressed by including a spatial frequency term, $\tilde{\kappa}$, in the complex propagation constant, $\tilde{\gamma}$, (equation 3.28) such that [90, 126],

$$\tilde{\gamma}^2 = \tilde{\kappa}^2 + i\mu\sigma\omega. \tag{3.46}$$

The spatial frequency of a coil represents how quickly the magnetic flux lines turns back to complete a closed loop in space. This is a function of coil size as well as the current applied to the coil. Intuitively, it follows that small coils have high spatial frequency as the flux lines quickly turn back to close the flux loops and so therefore do not propagate great distances in space. Larger coils have lower spatial frequency as the flux lines have a larger trajectory around the coil in order to close the loop and so will extend to greater distances in space.

The geometrically modified skin-depth, $\delta$, is then defined as [127],

$$\delta = \frac{1}{\Re\left[\tilde{\gamma}\right]} = \frac{1}{\Re\left[\sqrt{\tilde{\kappa}^2 + i\mu\sigma\omega}\right]}. \tag{3.47}$$

The equation governing the penetration of the $\mathbf{A}$-fields for spatial and temporal frequencies, $\kappa$ and $\omega$, respectively, is defined by Smith et al. [127] as,

$$\tilde{\mathbf{A}}(\kappa, \omega, r, z) = \tilde{\mathbf{A}}(\kappa, \omega, r)\left[1 + \Gamma(\kappa, \omega)\right] e^{-\tilde{\gamma} z}. \tag{3.48}$$

$\Gamma$ is the reflection coefficient at the interface between free-space and the conductive medium and is defined by Bowler and Johnson [90] as,

$$\Gamma = \frac{\tilde{\kappa} - \tilde{\gamma}}{\tilde{\kappa} + \tilde{\gamma}}. \tag{3.49}$$

By the analysis of equations 3.47 & 3.49 we can confirm that, in free space ($\sigma = 0$) such that $\Gamma = 0$ and so there is no reflection and so the magnetic field distribution in free space is only dependent on the spatial frequency. For the case of a plane wave, $\tilde{\kappa} = 0$, in electrically conducting material ($\sigma \neq 0$), the skin-depth becomes the standard depth of of penetration (equation 3.31) making $\Gamma = -1$. This corresponds to total reflection of the EM-field at the interface along propagation direction ($z$). The material interface, or reflection boundary, is inclusive of the eddy-current boundary layer and EM-fields generated within this layer do not count as transmission. Instead they form the mechanism by which the EM-field is reflected.

## 3.4 The Proximity Effect

The proximity effect is an eddy-current mechanism by which inductors exhibit AC frequency dependent resistive losses. Similar to the skin-effect, the proximity effect is the name given to distortion in the current distribution phenomenon within conductive wires as a result of inductive interactions between neighbouring current carrying wires. The time-varying magnetic fields, $B_1$, generated by AC excited wires, penetrates and induces eddy-current paths within neighbouring wires, via Faraday's law (sees ection 3.2). These eddy-currents flow in a direction so as to generate their own magnetic field, $B_2$, that opposes the one that created them (Ampére's law). The overall result of this effect is to cause a current crowding effect in the wire cross-section (figure 3.5).

The non-homogeneous current density becomes more prominent at high frequencies increasing the effective resistance of the wire above that of the DC resis-

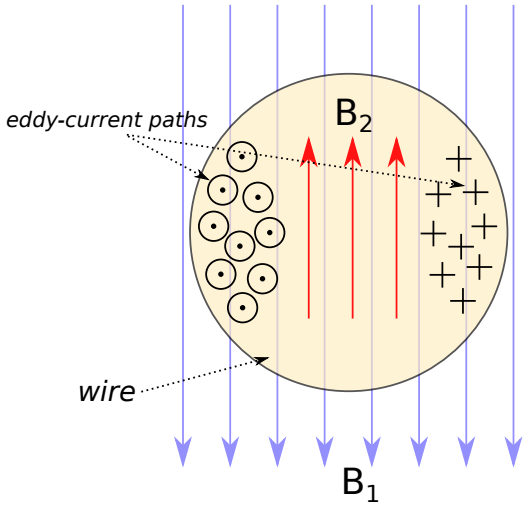


Figure 3.5: Diagram of eddy-current path induction in wire cross-section demonstrating the current crowding effect. Diagram shows time-varying primary magnetic field, $B_1$, and opposing secondary magnetic field, $B_2$, generated by eddy-current paths going into the page on the right hand side of the wire, and out of the page on the left hand side. After [128].

tance, $R_{DC}$. For multiple layers of neighbouring wire conductors, the proximity effect quickly becomes the dominant mechanism for resistive losses at high frequencies over the skin-effect [128]. High resistive losses influence the power of the component by damping the Q-factor (see section 3.7), which becomes a significant consideration when utilising electrical resonance behaviour.

There have been a number of attempts to produce analytical solutions for predicting the resistive losses in closely spaced windings. One of the oldest models still implemented is the Dowell method, from [129], whereby layers of coil windings are represented as foils of length equal to the core height. The increased cross-sectional area of the representative foil is compensated for by a layer porosity factor, effectively reducing the conductivity of the equivalent foils. Most models only accurately predict the AC resistance over certain frequency ranges and are typically only applicable to specific coil designs and geometries [130]. Finite element modelling (FEM) of the problem can also be used to calculated the resistive losses for a given geometry but are typically computationally expensive so more analytical models are

frequently sought [131, 132].

## 3.5 Modelling Eddy-Current Behaviour

A model for the calculating the current density generated by an infinitely thin coil (delta-coil) above a conducting two-layer half-space (as depicted in figure 3.6) can be calculated using the analytical solutions set out by Dodd and Deeds [126] for the magnetic vector potential, **A**.

For the axially-symmetric system in figure 3.6 the magnetic vector potential,

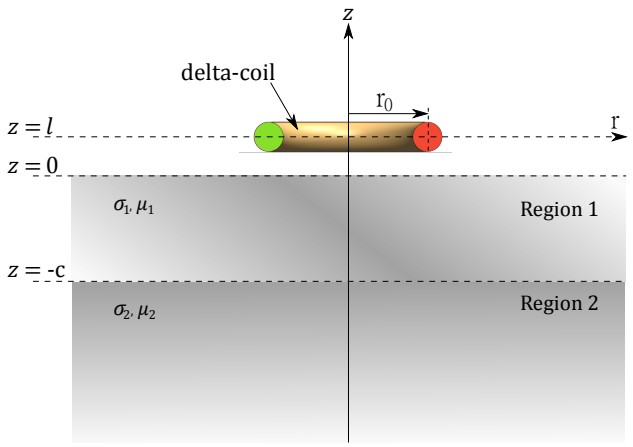


Figure 3.6: Cross-sectional diagram of a delta-function coil above a conducting half-space showing the parameters used in the Dodd and Deeds analytical solution. After [126].

$\mathbf{A}_1(r,z)$, at a radial position $r$ and a depth $z$, can be calculated for each of the two layer regions of the half-space using the formulae,

$$\begin{aligned}\mathbf{A}_1(r,z) &= \mu_1 I r_0 \int_0^\infty \mathrm{J}_1(\alpha r_0)\mathrm{J}_1(\alpha r)e^{-\alpha l}\alpha \\ &\quad \times \left[\frac{(\alpha_1+\alpha_2)e^{2\alpha_1 c}e^{\alpha_1 z} + (\alpha_1-\alpha_2)e^{-\alpha_1 z}}{(\alpha-\alpha_2)(\alpha_1-\alpha_2) + (\alpha+\alpha_1)(\alpha_1+\alpha_2)e^{2\alpha_1 c}}\right] d\alpha, \quad (3.50)\\ \mathbf{A}_2(r,z) &= \mu_2 I r_0 \int_0^\infty \mathrm{J}_1(\alpha r_0)\mathrm{J}_1(\alpha r)e^{-\alpha l}\alpha \\ &\quad \times \left[\frac{2\alpha_1 e^{c(\alpha_2+\alpha_1)}e^{\alpha_2 z}}{(\alpha-\alpha_2)(\alpha_1-\alpha_2) + (\alpha+\alpha_1)(\alpha_1+\alpha_2)e^{2\alpha_1 c}}\right] d\alpha. \quad (3.51)\end{aligned}$$

where $J_1$ is a first order Bessel function, $r_0$ is the coil radius, $l$ is the coil stand-off from the surface, $c$ is the thickness of Region 1, $\alpha$ is a continuous variable, referred to by Dodd and Deeds [126] as the separation constant, which embodies the spatial frequency parameter $\kappa$ defined in section 3.3.2. Thus $\alpha_i$ is equivalent to the propagation constant, $\tilde{\gamma}$, for region $i$, and so is defined as,

$$\alpha_i = \sqrt{\alpha^2 + i\omega\mu_i\sigma_i}. \tag{3.52}$$

Regions 1 & 2 have characteristic conductivities, $\sigma_i$, and permeabilities, $\mu_i$, where $i$ denotes the layer number. The current density within a conducting material can therefore be calculated using equations 3.50 & 3.51 and the relationship,

$$\mathbf{J} = -i\omega\sigma\mathbf{A}. \tag{3.53}$$

Dodd and Deeds [126] go on to define magnetic vector potential expressions for finite width coil windings and even the coil winding impedance in air and above a conducting half-space as,

$$\begin{aligned}\mathbf{Z} \;=\; & \frac{i\omega\pi\mu n^2}{(l_2-l_1)^2(r_2-r_1)^2}\int_0^\infty \frac{1}{\alpha^5}\mathrm{I}^2\Bigg(2(l_2-l_1) \\ & + \alpha^{-1}\left\{2e^{-\alpha(l_2-l_1)} - 2 + \left[e^{-2\alpha l_2} + e^{-2\alpha l_1} - 2e^{-\alpha(l_2+l1)}\right]\right. \\ & \left.\times\left[\frac{(\alpha+\alpha_1)(\alpha_1-\alpha_2)+(\alpha-\alpha_1)(\alpha_1+\alpha_2)e^{2\alpha_1 c}}{(\alpha-\alpha_1)(\alpha_1-\alpha_2)+(\alpha+\alpha_1)(\alpha_1+\alpha_2)e^{2\alpha_1 c}}\right]\right\}\Bigg),\end{aligned} \tag{3.54}$$

were $r_1$ and $r_2$ are the inner and outer radius of the finite thickness coil, and $l_1$, $l_2$ are the top and bottom of the finite thickness coil winding in the z-plane. Many authors [70, 109, 134, 135, 136, 137] develop models in order to predict the results of ECT measurements for given geometries, probe configurations and defect dimensions. Although developing in complexity, these models are often limited to simulating simple geometries and typically predict the behaviour of probe behaving as ideal

inductors i.e. well away from electrical resonance.

## 3.6 Eddy-Current Measurement

Eddy-current measurements are performed by measuring changes in the magnetic field arising due to the eddy-currents in the test material. This can be done using a range of magnetic field sensors including electromagnets, Hall-effect sensors and giant-magneto resistors (GMRs) to name just a few. The work carried out in this thesis uses electromagnet coil sensors to sense the magnetic field changes in the surface of the material. This was done by monitoring the electrical properties of a coil whose impedance, $Z$, will change depending on the environment it is encountering.

### 3.6.1 Electrical Impedance

Impedance is a component's total opposition to current flow and is defined as the ratio between the voltage across the inductor ($V$) and the driving current ($I$). Alternatively, $Z$ can be represented as a complex number with real components of resistance ($R$) and imaginary components of reactance ($X$), as given by the equation,

$$Z = \frac{V}{I} = R + iX \tag{3.55}$$

The reactance represents a components dynamic opposition to a change in current flow and is a frequency dependent effect that can have both inductive, $X_L$, capacitive, $X_C$, and sometimes resistive, $X_R$, components. Inductive reactance increases linearly with excitation frequency as,

$$X_L = \omega L, \tag{3.56}$$

and capacitive reactance decrease with frequency as,

$$X_C = \frac{1}{\omega C}, \tag{3.57}$$

where $L$ is the inductance and $C$ is the capacitance of the system. The real (resistive) and imaginary (reactive) components of impedance ($\Re\{Z\}$ and $\Im\{Z\}$ respectively) can be plotted in the complex impedance plane, or Argand diagram (figure 3.7), such that the magnitude, $|Z|$, and phase, $\phi$, of the impedance (equations 3.58 and 3.59) can be visually depicted.

$$|Z| = \sqrt{R^2 + X^2}, \tag{3.58}$$

$$\phi = \arctan \frac{X}{R}. \tag{3.59}$$

The phase of the complex impedance represents the phase difference between the

Table 3.1: Circuit model: Impedance and phase of ideal circuit components.

| Component | Impedance, $Z$ ($\Omega$) | Phase $\phi$ ($^\circ$) |
|---|---|---|
| Resistor ($R$) | $Z_R = R$ | $0^\circ$ |
| Capacitor ($C$) | $Z_C = iX_C = -i/\omega C$ | $-90^\circ$ |
| Inductor ($L$) | $Z_L = iX_L = i\omega L$ | $+90^\circ$ |

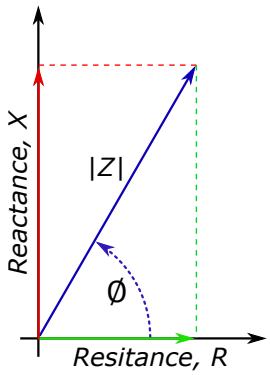


Figure 3.7: Example Argand diagram showing the resistive and reactive components on the complex impedance.

voltage, $V$, and the current, $I$, supplying the coil.

An ideal resistor will have only real resistive components of impedance and zero inductive or capacitive parts ($X = 0$) such that the phase between voltage and current is zero (figure 3.7). Likewise, ideal capacitors and inductors would only have capacitive and inductive reactance components respectively corresponding to the voltage having a phase, relative to the current, of $-90°$ or $+90°$ respectively [123]. The impedance of ideal components are given in Table 3.1 along with the resulting phases, $\phi$, of each.

Both inductors and capacitors store energy. An inductor store energy in the magnetic field it generates around itself, whereas a capacitor stores energy in the electric field between its charged plates. When the power to the components is cut off they will each discharge their stored energy back into electrical current at a characteristic rate.

## 3.7 Equivalence Circuit Model

As a first approximation, an ECT probe can be very simply modelled as the combination of lumped electronic components; an inductor (coil), a parallel capacitor (parasitic capacitance) and series resistance (circuit resistance) known as an LCR circuit, as shown in figure 3.8. This model is a simplistic combination of components where capacitive contributions from the coil turns and cable are all lumped together, cable parasitic conductance, inductance and resistance are neglected, and the influence of the skin and proximity effects on the resistance of the excitation wire is also neglected. The total impedance of this simple ECT coil model is a combination of all of the terms in table 3.1.

The complex impedance (the total obstruction to the flow of current) for

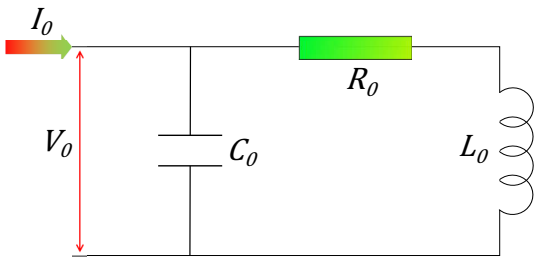


Figure 3.8: Simplified equivalent circuit for an eddy-current probe in free space with a coaxial cable connection.

this model can be derived using Kirchhoff's Laws and expressed as,

$$Z_0 = \frac{R_0 + i\omega L_0}{1 + i\omega R_0 C_0 - \omega^2 L_0 C_0}. \tag{3.60}$$

Equation 3.60 can be re-arranged into real and imaginary components of impedance such that,

$$Z_0 = \left[\frac{R_0}{(1-\omega^2 L_0 C_0)^2 + (\omega R_0 C_0)^2}\right] + i\left[\frac{\omega L_0(1-\omega^2 L_0 C_0) - \omega R_0^2 C_0}{(1-\omega^2 L_0 C_0)^2 + (\omega R_0 C_0)^2}\right]. \tag{3.61}$$

There will occur a frequency, $f_0$, where the inductive and capacitive reactances' are equal such that the imaginary component of impedance is zero. At this frequency the phase is zero and the magnitude of impedance is a maximum. This is known as the electrical resonant frequency and, for a system where the skin-effect on the total resistance is negligible, is calculated as[2],

$$\omega_0 = 2\pi f_0 = \sqrt{\frac{1}{L_0 C_0} + \left(\frac{R_0}{L_0}\right)^2}. \tag{3.62}$$

For the high inductance probes the inductive reactance is much greater than the resistance ($R_0 \ll \omega L_0$), such that the electrical resonant frequency is more commonly

[2]Electrical resonance is defined here as the frequency when the phase of impedance is zero. In reality there is also a magnitude resonance that occurs when the denominator in equation 3.61 is a minimum, occurring at a slightly different frequency defined as, $\omega_0 = 2\pi f_0 = \sqrt{\frac{1}{L_0 C_0} + \frac{1}{2}\left(\frac{R_0}{L_0}\right)^2}$

approximated to,

$$2\pi f_0 \approx \sqrt{\frac{1}{L_0 C_0}}. \tag{3.63}$$

The system is predominantly inductive ($\phi = 90°$) while the denominator of equation 3.61 is positive ($1 \gg \omega^2 L_0 C_0$). At higher frequencies the denominator turns negative ($1 \ll \omega^2 L_0 C_0$) and the probe behaves like a capacitive system ($\phi = -90°$) i.e. capacitive processes dominate the flow of current. The magnitude and phase of impedance of a real probe over a wide MHz frequency spectrum is shown in figure 3.9 highlighting the transition from inductive to capacitive regimes.

The complex components of impedance for a real ECT coil in air are shown

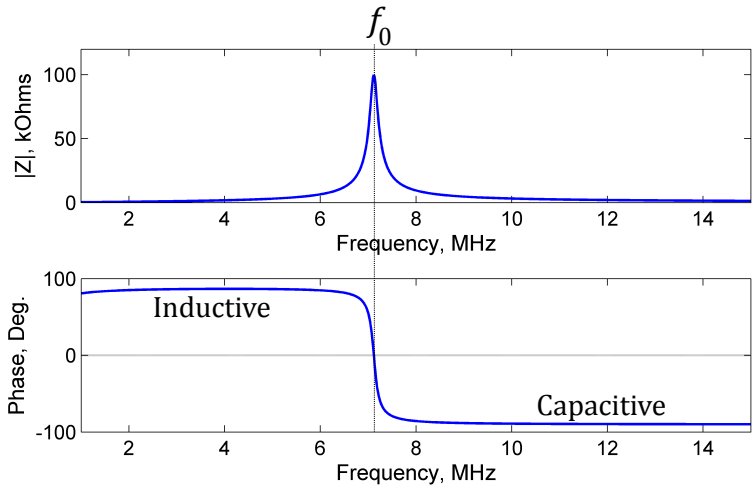


Figure 3.9: Electrical Resonance: Peak in an eddy current testing (ECT) coil showing the magnitude and phase of impedance as it passes through the resonant frequency, $f_0$.

as a function of frequency in figure 3.10.

Electrical resonance in a parallel LCR circuit means that the current is maximally stored and transferred between inductor and capacitor components. So, for a system supplied with a constant alternating current, the voltage required to force the same current through the system rises to a maximum. Via the equation for impedance $Z = V/I$ this is equivalent to an impedance magnitude maximum, as

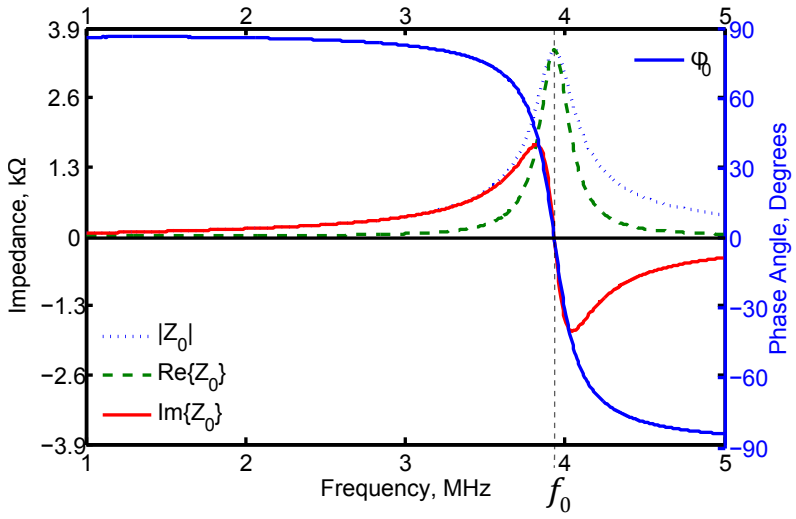


Figure 3.10: Electrical Resonance: Experimentally measured components of complex impedance for the ECT probe in Air showing the real, imaginary, magnitude and phase of impedance from 1-5MHz. The system goes through electrical resonance a $f_0 = 3.93 \pm 0.01 MHz$.

observed in figure 3.9 & 3.10.

As with any resonating system, small variations in the delicate balance of the components of the system ($L_0$ and $C_0$) will lead to large changes in the amplitude of the electrical properties. Eddy-current inspections rely on measuring the electrical changes in the inductive component of the probe and therefore must operate within the range of frequencies below electrical resonance. Measurements at frequencies beyond electrical resonance would predominantly be a measure of the capacitance of the system. The typical upper operating frequency of a probe is therefore limited by the resonant frequency which is dependent on the balance between the inductance and capacitance of the system.

### 3.7.1 Q-Factor

The resistive component in the circuit has a damping effect on resonance and therefore gives the resonance peak it's width and amplitude. A measure of how under-

damped the resonance is, is given by the quality factor, defined as,

$$Q = \frac{f_0}{f_2 - f_1}, \tag{3.64}$$

$$= \frac{\omega_0 L}{R} \tag{3.65}$$

where $f_1$ & $f_2$ are the frequencies at the half power point of the resonance peak either side of resonance, $L$ is the inductance of the system and $R$ is the series resistance of the system. $f_1$ & $f_2$ are characterised as the -3db drop which is equivalent to the the frequency at which the amplitude is equal to $1/\sqrt{2}$ of the maximum amplitude. Large Q-factors occur for $\omega_0 L \gg R$ tending towards a monotonic delta-function. The Q-factor decreases with increasing resistance.

### 3.7.2 Sources of Capacitance

There are numerous mechanisms that produce capacitive effects in an ECT probe circuit, however some are more dominant than others. The main mechanisms for capacitance in a simple ECT probe are coil parasitic capacitance and the capacitance of the coaxial cable.

#### Parasitic Self-Capacitance

A current carrying wire in close proximity to another will experience a parasitic capacitance between the two. A coil's self-capacitance, or stray parasitic capacitance, occurs between adjacent coil turns (turn-to-turn) and between turns and the surface of a conducting core (turn-to-core) if there is one.

Massarini and Kazimierczuk [140] and Grandi et al. [141] set out a series of equations for calculating the self-capacitance of a coil of diameter $D_t$ and $n$ number of turns. The turn-to-turn capacitance, $C_{tt}$, of two neighbouring turns of

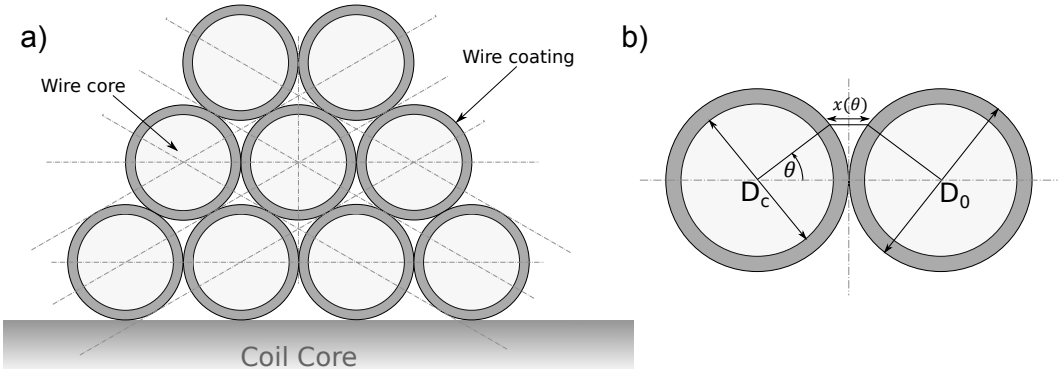


Figure 3.11: Cross-sectional diagram of a) layered coil windings around a core, and b) assumed path $x(\theta)$ of an electrical field line at an angle $\theta$ between two coil turns, after [140].

core diameter $D_c$ and outer diameter (including cladding) $D_0$, is given by,

$$C_{tt} = \epsilon_0 l_t \left\{ \frac{\epsilon_r \theta^*}{\ln \frac{D_0}{D_c}} + \cot\left(\frac{\theta^*}{2}\right) - \cot\left(\frac{\pi}{12}\right) \right\}, \tag{3.66}$$

where $\epsilon_r$, is the relative permittivity of the dielectric wire coating, $l_t = \pi D_t$ is the winding length around the core, and $\theta^*$ corresponds to a characteristic angle of the configuration where the air gap capacitance, along the electric field line path $x(\theta)$, is equal to the coating capacitance [140]. This is defined as,

$$\theta^* = \arccos\left(1 - \frac{\ln \frac{D_0}{D_c}}{\epsilon_r}\right). \tag{3.67}$$

Multiple winding layers and capacitance between windings and the core material introduce additional capacitive effects which further complicate the self capacitance of the coil. The resulting self capacitance of multiple layered coils with both air and ferrite cores are approximated in Massarini and Kazimierczuk [140] as a factor of $C_{tt}$. However, the self-capacitance of the coil is rarely the dominant contributor to the overall capacitance of an ECT probe. Instead it is the coaxial cable capacitance that is more significant, and will be discussed in the following section.

**Coaxial Cable Capacitance**

Although the self capacitance of a coil is an important consideration, an ECT probe is operated using a co-axial cable which has a much greater contribution to the capacitive component of the ECT equivalence circuit diagram in section 3.7. Coaxial cables are typically characterised by their capacitance per unit length, $C_n$. The capacitance of a given length of co-axial cable can then be calculated and used as a lumped component in the equivalence circuit (figure 3.8). However, coaxial cable actually contributes resistive, inductive and capacitive components to the system. As such it can be modelled as a transmission line using network theory.

Network theory is a well-established concept within electrical engineering for designing analogue and digital filters. The concepts of network theory can be used to model the effects of a coaxial cable transmission line on an ECT system [123, 142, 143]. The basic geometry of a coaxial cable is shown in figure 3.12.

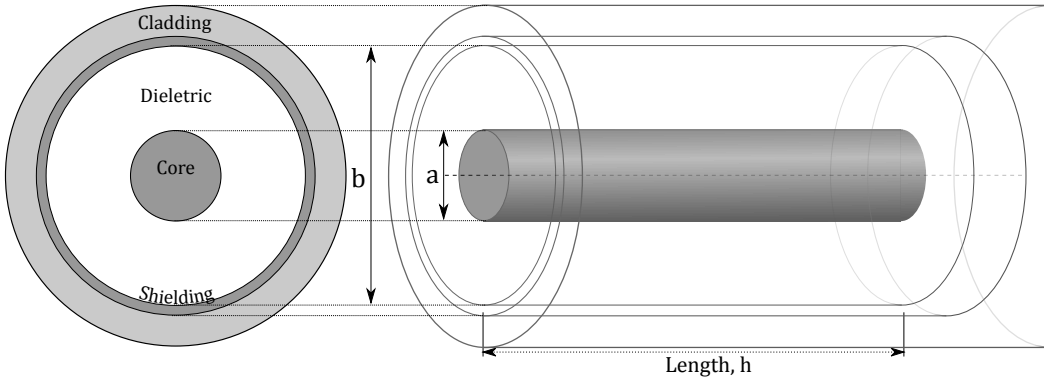


Figure 3.12: Geometry of a coaxial cable, showing core diameter and the shields inner diameter, adapted from Wheeler [39].

A simplified transmission line model for a coaxial cable is made up of a series of unit circuits containing series resistance and inductance, representing the coaxial cable core, and shunt capacitance, representing the voltage difference between the inner and outer conductors (figure 3.12).

This model assumes that losses due to shunt conductance between inner

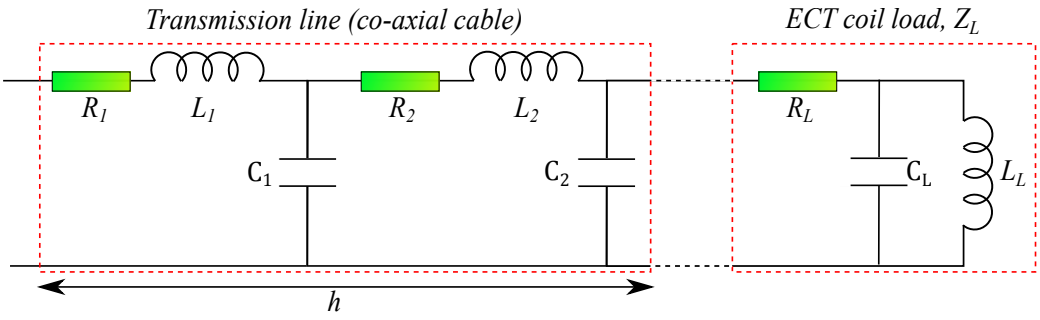


Figure 3.13: Equivalence circuit model for inductively loaded coaxial cable transmission line.

and outer conductors are negligible. The components within each unit circuit of the co-axial cable are the components per unit length of the cable and equal to all other unit length components i.e. $R_1 = R_2 = R_n = R_c/h$, $L_1 = L_2 = L_n = L_c/h$ and $C_1 = C_2 = C_n = C_c/h$. Components with subscript c represent the total value of the cable. The resistance, inductance and capacitance per unit length of a simple coaxial cable (figure 3.13) can be calculated by the equations [39, 144],

$$\frac{R}{h} = \frac{\rho}{\pi\delta_s}(\frac{1}{a} + \frac{1}{b}), \qquad \Omega m^{-1} \qquad (3.68)$$

$$\frac{L}{h} = \frac{\mu}{2\pi}\log\frac{b}{a}, \qquad Hm^{-1} \qquad (3.69)$$

$$\frac{C}{h} = \frac{2\pi\epsilon}{\log\frac{b}{a}}, \qquad Fm^{-1} \qquad (3.70)$$

where $\rho$ is the resistivity of the conductor, and $\mu$ and $\epsilon$ are the magnetic permeability and electric permittivity (dielectric constant) of the insulating material between the core and the shield respectively. The resistance of the conductor is dependent on the frequency of excitation due to the skin effect (see section 3.3). Many coaxial cable conductors are made of interwoven strands of wire making them more flexible and less susceptible to the skin and proximity effects (section 3.3), however the following model only assumes a single core.

Using the equations for reactance ($X$) from section 3.6.1 and the concept of parallel admittance summation [123], the series impedance of $L$ and $R$, and shunt

impedance of $C$ can be expressed as,

$$Z_n = R_n + i\omega L_n, \tag{3.71}$$

$$Y_n = \frac{1}{Z_C} = i\omega C_n. \tag{3.72}$$

Therefore the total impedance of the cable and load system can be calculated by equation 3.73 [142].

$$Z_\tau = Z_1 + \cfrac{1}{Y_1 + \cfrac{1}{Z_2 + \cfrac{1}{Y_2 + \cfrac{1}{\cdots + \cfrac{1}{Z_n + \cfrac{1}{Y_n + Z_L}}}}}}. \tag{3.73}$$

Equation 3.73 can be simplified for a cable of unit length, $n$, with unit impedance $Z_1 = Z_2 = Z_n = Z_c$ and unit admittance $Y_1 = Y_2 = Y_n = Y_c$, as,

$$Z_\tau(n) = Z_c + \cfrac{1}{Y_c + \cfrac{1}{Z_\tau(n-1)}}, \tag{3.74}$$

where $Z_\tau(n-1)$ is the impedance of the transmission line of unit length, $n-1$. The result of the transmission line on an inductor load impedance, $Z_L$, is to excite multiple harmonic resonant frequencies as the load inductance resonates with different lumped quantities of the transmission line. Equation 3.74 can therefore be used to predict the frequencies that these harmonic resonances will occur for a given cable length.

The equivalence circuit models so far discussed have only considered a coil

in air. However, when brought into the proximity of an electrically conducting material, eddy-currents are generated within the surface and electromagnetic coupling occurs between the coil and the adjacent material. The equivalent circuit in figure 3.8 can be extended to a transformer model to represent the coupling interaction, and has been utilized by many authors [39, 97, 147, 148]. Here we develop an equivalent circuit transformer model and consider the influence of the skin effect on the system.

### 3.7.3 The Transformer Model

It has been shown that (see section 3.2), when an inductor is brought into the proximity of an electrically conducting material, it will electromagnetically couple to the eddy-currents it generates in the material surface. The electromagnetic coupling between the coil and eddy-currents changes the electrical properties of the sensor probe circuit for an ideal inductor. The coupling interaction can be modelled as a transformer circuit shown in figure 3.14, where the effect of the eddy-currents is modelled as a passive series inductor and resistance (LR) circuit [147]. This

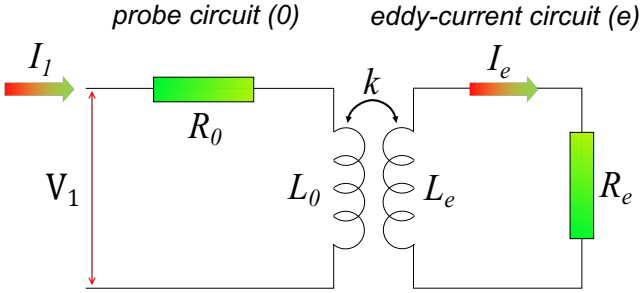


Figure 3.14: The transformer model: Simple transformer circuit model for an eddy-current probe (0) coupled to the surface of an electrically conducting material (e).

simple equivalent circuit is based on the assumption that the coupling coefficient, $k$, is invariant of excitation frequency. In reality, frequency alters the eddy-current distribution within the surface of the material as determined by the skin-effect (see section 3.3) [39]. Hence, frequency will influence the inductive component of the

eddy-current circuit (figure 3.14), such that coupling between the probe and eddy-current inductor components will be frequency dependent.

Assuming no prior knowledge of the eddy-current circuit (i.e. the phase of the current flow), and ignoring the parallel capacitive effects of the coaxial cable for the moment, Kirchhoffs laws are used to determine the effective impedance of the inductive branch, shown in figure 3.14, $Z_1$, of the probe circuit.

$$V_1 = I_1(R_0 + i\omega L_0) + I_e(i\omega M), \tag{3.75}$$

$$0 = I_e(R_e + i\omega L_e) + I_1(i\omega M). \tag{3.76}$$

The mutual inductance, $M$, between the circuits is defined as [149],

$$M = k\sqrt{L_0 L_e}, \tag{3.77}$$

where $k$ is the coefficient of coupling between the two inductors. Rearranging equation 3.76 to give $I_e$ gives,

$$I_e = -I_1 \frac{i\omega M}{R_e + i\omega L_e}, \tag{3.78}$$

$$I_e = -I_1 \frac{\omega M}{{R_e}^2 + \omega^2 {L_e}^2}(\omega L_e + iR_e). \tag{3.79}$$

It is common for authors implementing the transformer model to equate the eddy-currents to a loop of wire and then make the assumption that the resistive component of the eddy-current circuit is frequency invariant [147, 148]. This would certainly be true for two coupled coils such that the expression $R_e \ll \omega L_e$ can be applied for high frequencies, hence making $I_e$ entirely real. This would require that the eddy currents flow exactly out of phase (i.e. the mirror image) with the generating current, $I_1$.

However, as was demonstrated in section 3.3, for plane wave excitation, the resistive and reactive components of the eddy-current impedance are equal in

magnitude ($R_e = \omega L_e = X_e$) so that, for the plane wave case, $I_e$ becomes,

$$I_e = -I_1 \omega L_0 \frac{k^2}{2}(1+i). \tag{3.80}$$

$$\equiv I_1 \omega L_0 \frac{k^2}{\sqrt{2}} e^{-\frac{3\pi}{4}}. \tag{3.81}$$

Equation 3.81 is equivalent to equation 3.37 in that, for plane wave excitation, the eddy-current circuit has real and imaginary components that are equal in magnitude and are both dependent on excitation frequency. This leads to the secondary circuit lagging the primary excitation circuit by $-\frac{3\pi}{4}$.

This result was derived but its significance was not explicitly stated in Wheeler [39]. It is also contrary to a commonly implemented assumption that the eddy-current secondary circuit supports a perfect mirror current (perfectly out of phase to the generation current). The phase lag of eddy-currents will therefore result in a phase shift in the magnetic field generated by the eddy-currents, which will influence the phase of the measured impedance of the coil.

Carrying on the derivation, equation 3.79 can be substituted into equation 3.75 to give,

$$Z_1 = \frac{V_1}{I_1} = (R_0 + i\omega L_0) + \frac{\omega^2 k^2 L_0 L_e}{{R_e}^2 + \omega^2 {L_e}^2}(R_e - i\omega L_e). \tag{3.82}$$

The eddy-current circuit components are unknown, however certain arguments can be applied to infer the behaviour of the system. It is sometimes assumed [150] that the resistive component of the eddy-current circuit is negligible compared to the inductive component and does not change with frequency ($R_e \ll \omega L_e$). Although applicable to traditional transformer circuits where the primary and secondary circuits are both coil windings, the result is that only the reactive component of impedance changes due to the presence of a conducting material. This is plainly incorrect.

The other end of the assumption spectrum is to assume the probe in an

infinite inductor such that the plane wave approximation from section 3.3.1 can again be applied. The result is that both the resistive and reactive components of the eddy-current circuit are equal in magnitude, i.e. $R_e = \omega L_e = X_e$, such that equation 3.82 can be shown to be,

$$Z_1 = R_0 + i\omega L_0 + \omega L_0 \frac{k^2}{2}(1-i), \tag{3.83}$$

$$= Z_0 + \omega L_0 \frac{k^2}{2}(1-i). \tag{3.84}$$

As a result, both real and imaginary parts of the $Z_1$ are equally dependent on frequency due to the the skin-effect for the plane-wave case. In reality an ECT coil will never generate a plane-wave and so the resistive and reactive components will not be equal in magnitude. From equation 3.82, the complex third term, which defines the materials influence on the impedance, can be rewritten in terms of a complex coupling coefficient, $\tilde{k}$.

$$Z_1 = R_0 + i\omega L_0 \left(1 - \tilde{k}^2\right), \tag{3.85}$$

$$= Z_0 - i\omega L_0 \tilde{k}^2. \tag{3.86}$$

where,

$$\tilde{k}^2 = \alpha k^2(\omega L_e - iR_e), \tag{3.87}$$

and,

$$\alpha = \frac{\omega L_e}{{R_e}^2 + \omega^2 {L_e}^2}. \tag{3.88}$$

This is equivalent to saying that the current in the secondary circuit, $I_e$ in figure 3.14, is in phase with the excitation current, $I_1$, and the complex response of the material is entirely contained within a complex coupling coefficient, $\tilde{k}$. For a real inductor, $\tilde{k}$ will be complex number somewhere between the idealised transformer model assumption of an entirely real mirror current ($R_e \ll \omega L_e$), and the plane-

wave approximation ($R_e = \omega L_e$), thereby resulting in a phase change in frequencies below electrical resonance.

Using the same approach as in section 3.7, a simplified expression for the impedance of the system can be found when the transformer system is in parallel with a capacitive component (i.e. coaxial cable lumped capacitance), $C_0$.

$$Z_1 = \left[\frac{R_0'}{(1-\omega^2 L_0' C_0)^2 + (\omega R_0' C_0)^2}\right] + i\left[\frac{\omega L_0'(1-\omega^2 L_0' C_0) - \omega R_0'^2 C_0}{(1-\omega^2 L_0' C_0)^2 + (\omega R_0' C_0)^2}\right], \tag{3.89}$$

where $R_0'$ and $L_0'$ represent the effective resistive and inductive reactance,

$$R_0' = R_0 + \alpha k^2 \omega L_0 R_e, \tag{3.90}$$

$$L_0' = L_0\left(1 + \alpha k^2 \omega L_e\right). \tag{3.91}$$

and where both the resistive and reactive components are a function of frequency.

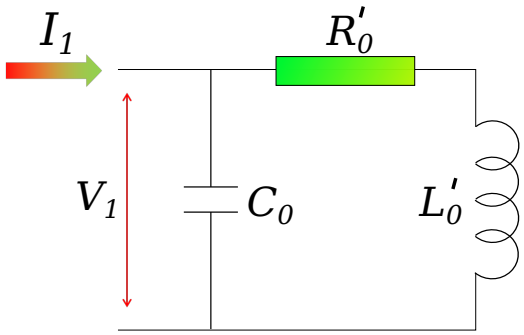


Figure 3.15: Simplified equivalence circuit model for material coupled coil and cable system.

The resulting expression for the electrical resonant frequency is a non-trivial solution to a polynomial frequency function. However, returning to the unique case of a uniform excitation field ($R_e = \omega L_e$), then the resonant frequency can be roughly

approximated to,

$$\omega_1 = 2\pi f_1 \approx \sqrt{\frac{1}{C_0 L_0 (1 - \frac{1}{2}k^2)}}. \tag{3.92}$$

The result of coupling to the surface of an electrically conducting material is to effectively change the resistive and reactive components of the probe equivalence circuit. For a non-ferromagnetic test material, this causes an upwards shift in the electrical resonance of the system.

The quality factor of a coupled probe system, $Z_1$, at electrical resonance $\omega_1$, can be defined as,

$$Q_1 = \frac{\omega_1 L_0'}{R_0'}, \tag{3.93}$$

## 3.8 Summary

There are many, more sophisticated, models to simulate the electrical properties of an EC system which take into account some of the complexities of the system including; the effect of ferrite cores on stray coil capacitance and the skin effect in coil windings, as well as the proximity effect both between the individual coil windings, the windings and the core, and between the coil and the test material. However, for the purposes of investigating the resonant frequency behaviour of an ECT coil, the lumped equivalence circuit model provides a useful analogue.

# Chapter 4

# Eddy-Current Array Benchmark Study

## 4.1 Introduction

Eddy-current array (ECA) probes are becoming increasingly popular in industrial NDE inspections due to the improvements they can offer in the speed of inspection [38, 70, 105]. They offer a much greater probe coverage and so are ideally suited for the inspection of large surface areas, require simpler probe manipulation, and can offer desirable reliability for the inspection of some complex geometries [151, 152]. However, when it comes to inspecting for small defects in difficult (see section 2.5), safety critical components, a high sensitivity standard must be met by the probes and inspection systems. Without knowing the sensitivity capability of a new inspection, it cannot be implemented on such applications. For this reason a comprehensive characterisation study was carried out on a newly developed high-sensitivity probe, manufactured by Eddyfi (Quebec, Canada) for Rolls-Royce plc.

An ECA probe was developed by Eddyfi to meet specific inspection criteria for safety critical Ti6-4 components. The probe must be sensitive to a surface breaking notches of length, depth and gape of 0.75×0.38×0.10 mm in Ti6-4. The

probe must cover a length of 30 mm, and the probe must be cost effective. A balance must therefore be struck between sensitivity, cost and coverage. Changing any one significantly influences the other two elements. The resulting ECA probe was comprehensively characterised to establish its inspection limitations.

## 4.2 Probe Design

An array probe was developed for a Rolls-Royce high-sensitivity inspection. The probe coil elements were high inductance, multi-layered pancake coils with ferrite cores. The coil element configuration of the section of array investigated is shown in figure 4.1.

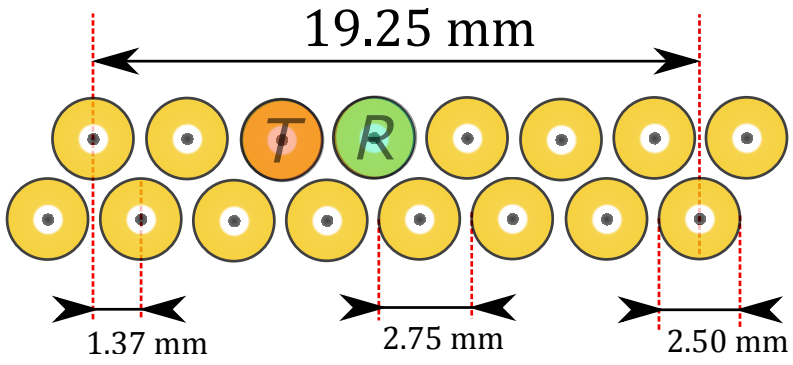


Figure 4.1: Transmit-Receive eddy-current array (ECA) coil configuration of a commercially available probe designed to detect a 0.75 mm surface notch in Titanium 6-4.

### 4.2.1 Array Operation

The probe is designed to perform a transmit-receive measurement between neighbouring coil elements at 1MHz (the maximum frequency limit of the operation system). Transmit-receive mode of excitation was chosen because of its superior phase separation between lift-off and defect signals in Ti6-4 compared to other modes of

excitation. Absolute mode is the most sensitive measurement however has very poor phase separation between defect and lift-off signals. Differential modes are lift-off invariant but insensitive to large defects. The differences in defect and lift-off signal between the three main modes of eddy-current operation are shown visually in Figure 4.2 where lift-off increases from right to left along the horizontal axis. The measurements were made using coils of the same dimensions and frequencies as those used in the final array probe.

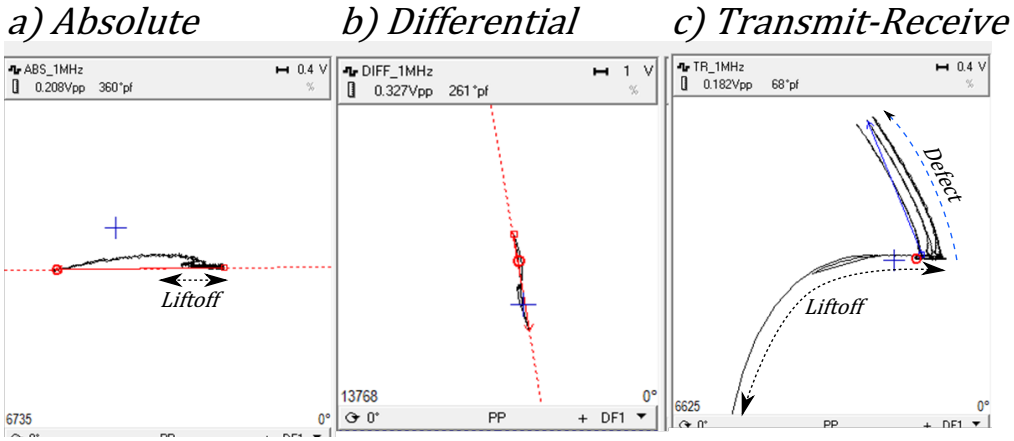


Figure 4.2: Screenshots of Lissajous plots for three different modes of measurement on Titanium 6-4 showing a defect signal in relation to a lift-off signal, a) Absolute, b) Differential, and c) Transmit-Receive.

The elements are fired in a transmit-receive configuration designed to be sensitive to defects orientated perpendicular to the scanning axis (figure 4.3). The transverse mode excites and receives on neighbouring coils within a row.

### 4.2.2 Normalisation

In order to normalise the array channels the probe had to be passed over a uniform slot so that all the channels could have their phase and gain values optimised to give the same signal response to the same indication. The desired response can be set depending on how the inspection is carried out. For the purposes of this inspection,

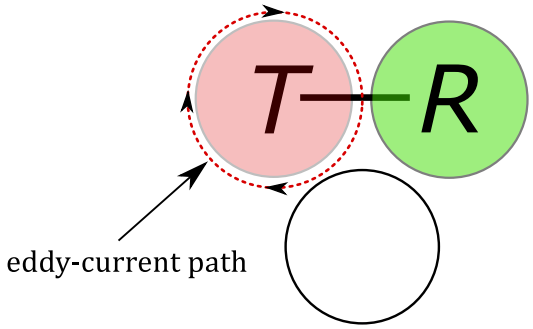


Figure 4.3: Transverse mode of transmit-receive measurements in a two staggered row array element configuration showing the defect orientation it is designed to be most sensitive to.

Table 4.1: ECA scan calibration parameters.

| | |
|---|---|
| Frequency | $1MHz$ |
| Filter(Spatial) | Median Bandpass ($5.1mm$) |
| Voltage | $6V$ |
| Measurement | Vertical Height |
| Angle | $30°$ |
| Measurement | Peak-to-peak first transition |

the normalisation conditions were set to those shown in table 4.1.

The gains and rotation of the channels can be monitored to determine the uniformity of a slot. This normalisation process is useful but variations in the probe pressure may occur when the probe is applied to the part.

## 4.3 Positional Sensitivity Study

A study was carried out to investigate how the position of the a target defect underneath the array affected the signal response from the array elements.

### 4.3.1 Experimental Method

A section of the array was raster scanned across an electron discharge machined (EDM) target notch ($0.75 \times 0.38 \times 0.10mm$ in surface size) to build up an under-

standing of the variations in sensitivity of the probe as the defect passes under different regions of the probe (figure 4.6). The test material was made from a scrap Ti6-4 component and machined to the same surface finish as in-service components. The raster scan was performed using a combination of 2 linear stages used in combination to form an XY-stage. The array was fixed in place and the test sample positioned on stage platform and moved in the X and Y planes to perform each leg of the raster scan. Due to the lack of linear encoder output, the ECA system acquired data from an internal time-base encoder, calibrated at an acquisition rate equal to the scanning speed of the linear stage in the X-axis (6 $mms^{-1}$).

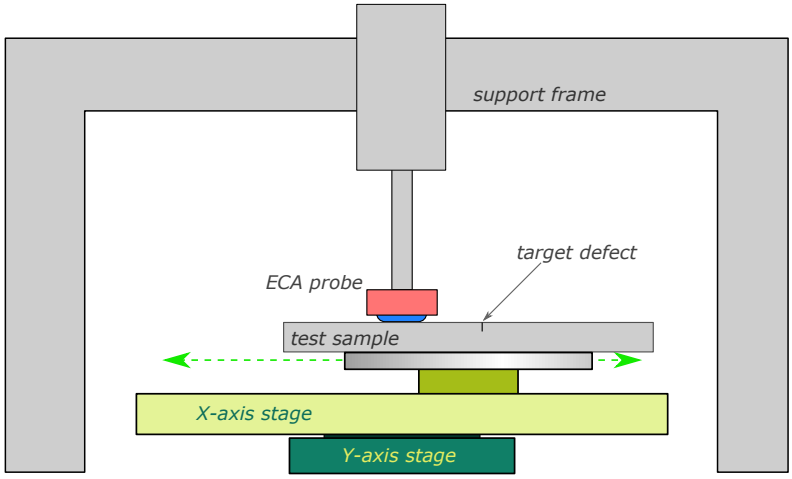


Figure 4.4: Cross-sectional diagram of ECA scanning stage showing the scanning range.

After normalisation, the following steps were carried out to complete the study:

1. Position the array on the test material, roughly in line with the test notch (see figure 4.6, and apply a small amount of pressure to ensure full contact of the array with the surface of the test sample.

2. Balance the array elements whilst the array is stationary and in contact with the material. This zeros the measurement on the Lissajous plot.

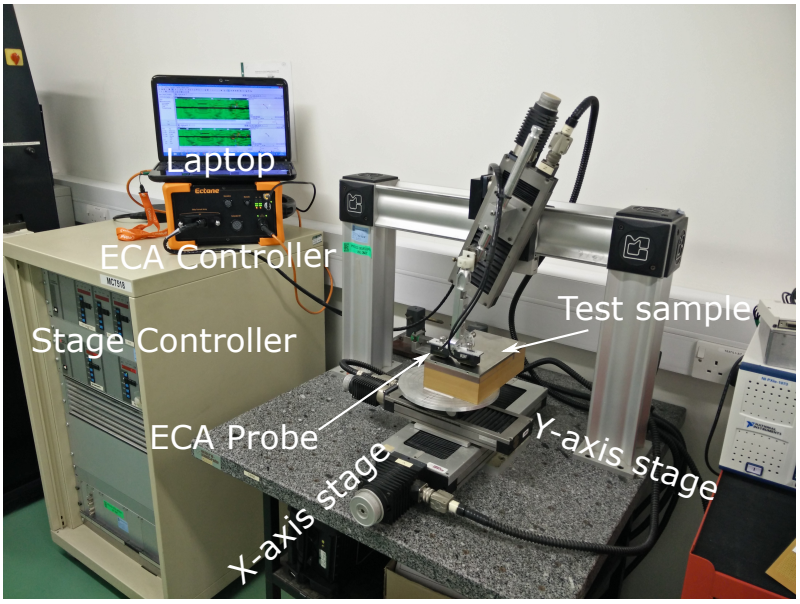


Figure 4.5: Image of ECA scanning system setup, using Eddyfi's Ectane ECA controller and linear stage scanning system.

3. Begin scanning acquisition in the Magnifi software and move the X-axis stage until the ECA probe has scanned over the target notch.

4. Stop acquisition and record the vertical height of the maximum defect signal and background material.

For each measurement the array was moved by increments of $0.12 \pm 0.01mm$ in the direction perpendicular to the scanning axis so as to provide multiple point measurements underneath each 1.37 mm channel of the array.

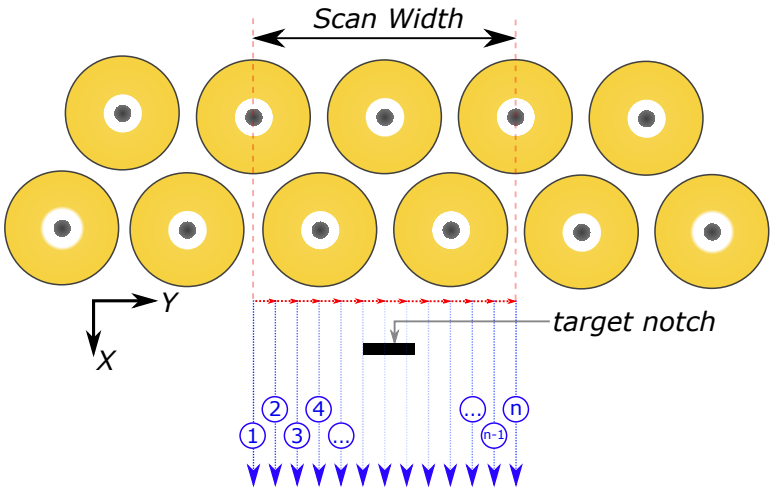


Figure 4.6: Schematic diagram of ECA raster scan method over a target EDM notch of 0.75 mm.

The maximum signal of the target defect was detected from the C-scan[1] and the maximum vertical height of the signal recorded (see figure 4.7). No vertical gains were applied to the signals. A measurement of the background noise was recorded for each pass over the target notch. Again the vertical height measurement method was used for the background noise.

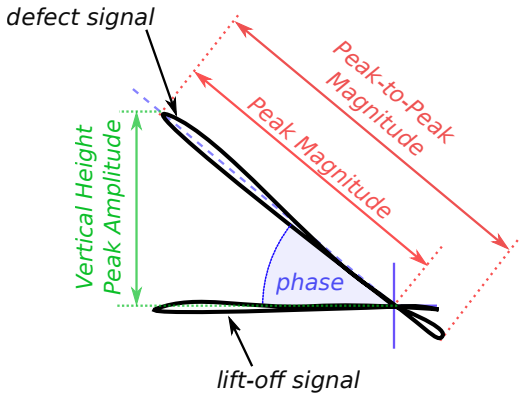


Figure 4.7: Example vertical height measurement used to record defect signals from ECA scans.

[1] A C-scan is a 2D image of the inspection surface constructed from components of the impedance data. In this instance C-scans were generated to depict the vertical height of the impedance data.

**Defining ECA Noise**

ECA measurements pose a more complex problem when considering noise. Standard manually operated ECT inspections use the maximum signal obtained from arbitrary undamaged sections of material as the measure of the noise level. This is less simple with an ECA inspection as each channel within the array will have varying levels of background noise based on the gains and phase rotations assigned them during normalisation. In addition, the close proximity of the coils to one another can lead to phantom electronic signals giving a false indication of the background noise.

Although these signals cannot be discounted in the consideration of background noise they must be acknowledged as artefacts of the inspection. As such, using the maximum recorded noise signal from the data is a false representation of the actual background noise level. Instead it is more fitting to use the root mean-squared (RMS) average of the background noise value from all of the measurements. This can then be used to assist in determining the decision threshold for the inspection.

The equation below expresses the RMS noise of a collection of $n$ measurements, where $N_i$ is the measured maximum noise from a scan of the $i^{th}$ sample.

$$N_{ECA} = \sqrt{\frac{1}{n}\sum_{i=1}^{n} N_i^2} \tag{4.1}$$

Signal-to-noise ratios (SNRs) given in the following sections of the report are defined using the above rms noise calculation unless stated otherwise.

### 4.3.2 Results

The vertical height of the defect signals was recorded as well as the defect signal phase angle. The results are shown in figure 4.8 for a region encompassing 5 channels.

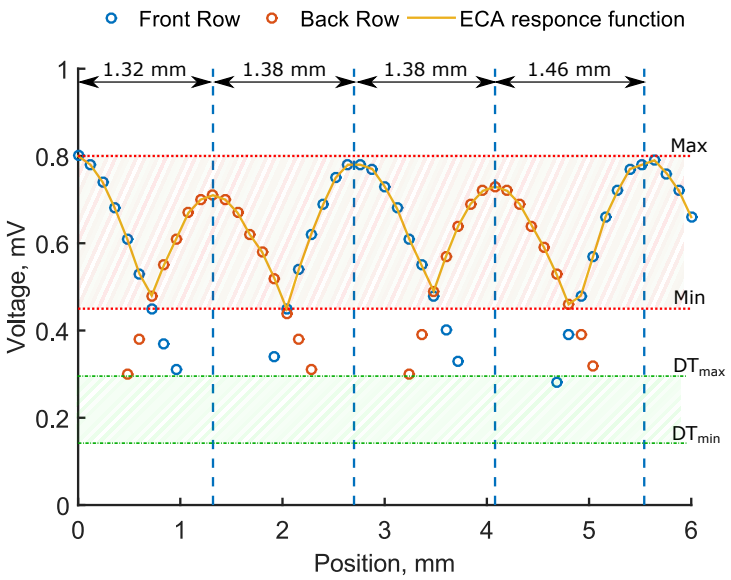


Figure 4.8: ECA signals response to 0.75 mm target notch at different positions under the array elements. Front and back row elements have been separated (blue and red circles respectively) and the range of possible defect signals indicated. The decision level (DT) range is also shown.

The results shown in figure 4.8 demonstrate the sensitivity bell curves associated with each TR measurement channel. The peaks of these curves correspond to the regions in between the active elements as described by Mook et al. [152]. The results are separated into front row and back row channels to demonstrate the effect of probe drag on the signal (see figure 4.9).

As the probe is moved across a surface, contact with the surface caused the front edge of the spring-loaded array pad to catch and the back edge to lift off the surface. This caused an increase in lift-off and tilt for the back row coils, reducing their sensitivity. This was proved by passing the probe over the same slot in the forward and backward directions and measuring the signals from the front and back rows. Reversing the direction caused the front and back rows to switch their peak sensitivities. This effect can be alleviated by reducing the pressure on the probe or by maintaining a slight lift-off from the sample at all times. However, lift-off rapidly

reduces the sensitivity of the measurement, as determined by the spatial frequency of the coil elements (see section 3.3.2).

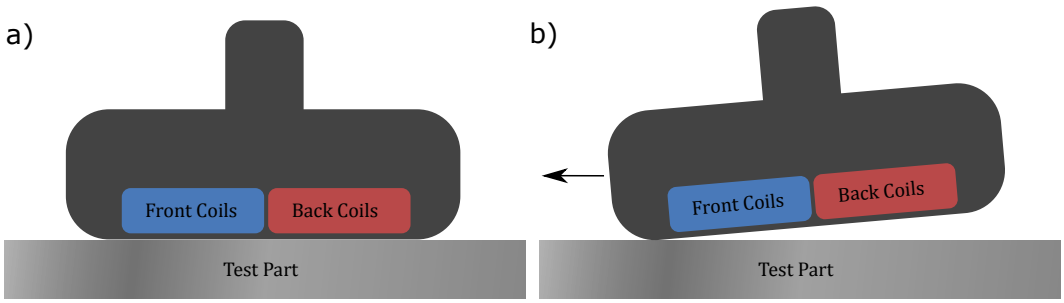


Figure 4.9: Example of probe drag effect causing increased lift-off and tilt on array elements thereby decreasing sensitivity on back row elements.

The array exhibits sensitivity "bells" underneath the most sensitive regions of the array, with maxima corresponding to the midway point between two neighbouring elements (i.e the centre of the transmit-receive channel). The bells have a spatial period of half the pitch between neighbouring coils (1.38 mm). However, the minimum sensitivity of the channels never falls below the maximum reject threshold.

### 4.3.3 Discussion

The phenomenon of the sensitivity curves experimentally measured is expected for the measurement of a feature smaller than the critical dimensions of the array elements. Although this variation occurs, the study shows that the array is capable of detecting the target notch with a good signal-to-noise across the whole array. However, the existence of this variation poses a problem to the manner in which an industrial inspection would be carried out.

Typical industrial ECT inspections perform a calibration measurement on a target notch to set the sensitivity level of the inspection. The gains are changed such that the notch signal usually extends to 80% of the screen height. The decision threshold (the threshold which, if a signal goes over, the component has failed the inspection) is then typically set at 30% screen height [153]. This method of cali-

bration becomes a problem when the signal of the calibration target notch could be a range of values depending on it's position beneath the array. This could result in over or under-estimating the decision threshold (DT) thus leading to missed defects or a high rate of false calls respectively. This is demonstrated by the decision threshold range depicted by the green shaded area in figure 4.8.

This sensitivity variation to the target defect represents a problem for ECA inspections. It is possible that defects will be detected at the sensitivity minimum of the array and the response may not be above the rejection threshold. This can be remedied by investing in arrays with smaller coil elements. However this will increase the cost of the probe in order to maintain the same coverage.

## 4.4 ECA Probability of Detection

Using the 1 MHz frequency transmit-receive (TR) eddy-current array (ECA) probe, detailed above, a probability of detection (PoD) study was carried out in order to statistically determine the reliable sensitivity of the inspection on Titanium 6-4 samples (See Appendix A).

### 4.4.1 Experimental Method

A probability of detection (PoD) study was carried out on the ECA probe to determine its intrinsic statistical sensitivity. This was achieved by scanning 39 fatigue cracks in Ti6-4, ranging from 0.10-5.75 mm in surface length, and measuring the signal response. The minimum detectable defect size at a given rejection threshold is determined using a computer programme based on the MIL-HDBK-1823, in accordance with RRP58000 [154, 155].

Current inspection sensitivity is established by setting signal response of the probe, to a reference standard target notch, to 80% screen height and then setting the rejection threshold to 30% screen height which is considered to be approximately

Table 4.2: Minimum statistically-reliable defect size detectable by the ECA probe as calculated via Probability of Detection analysis, comparing different $a_{thresh}$ levels.

| Description | Threshold (mV) | $a_{90/50}$ (mm) | $a_{90/95}$ (mm) |
|---|---|---|---|
| $3 \times N_{rms}$ | 0.10 | 0.65 | 0.74 |
| 20% Screen Height | 0.16 | 0.85 | 0.96 |
| $3 \times N_{max}$ (30% SH) | 0.25 | 1.07 | 1.21 |

3× the maximum noise level [153]. The reliable detectability of the system directly depends on this rejection threshold.

Using the same scanning system as was shown in figure 4.5, the PoD samples were scanned as a typical ECA inspection would be performed, in a single pass. As a result the PoD analysis would then also represent the uncertainty of where along the array a defect was detected, i.e. by the most or least sensitive regions of the array element (see figure 4.8).

### 4.4.2 Results

PoD analysis was performed on the recorded data set of signal responses. The signal response data is displayed as a function of the defect size in figure 4.10, showing the linear best fit plot applied using the MH1823 software in statistical analysis software "R" [154].

The probability of detection curve, for a decision threshold of $a_{thresh} = 0.2\ mV$ is displayed in figure 4.11. The decision threshold was set based on 3× the maximum background noise. The analysis predicts that the ECA probe will be able to reliably detect (9 times out of 10 with 95% confidence) a defect size of $a_{90/95} = 1.07\ mm$. A summary of the detectable defect size for different 2 significant figure $a_{thresh}$ values is shown in table 4.2.

For this analysis the screen height of the inspection was set based on the root-mean square of the sensitivity variation shown in figure 4.8 being 80% screen height. The calculated minimum statistically-detectable defect size is significantly

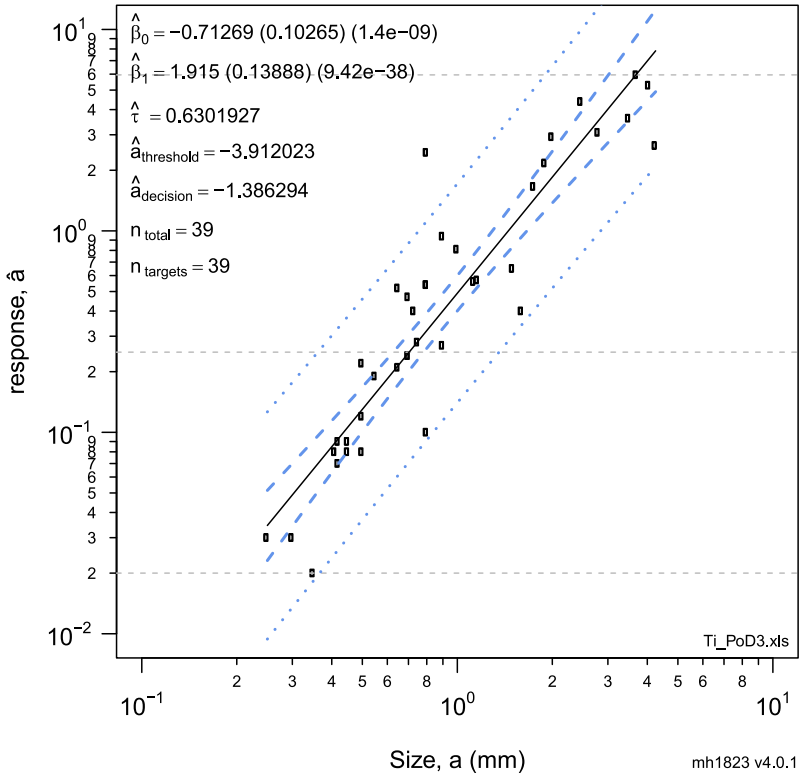


Figure 4.10: Size, $a$, vs signal response, $a_{hat}$ in log-log space showing linear best fit and confidence bounds as produced using MH1823 software in R [154].

larger that the target defect size (0.75 mm).

## 4.5 Conclusion

An examination was performed investigating the sensitivity limitations of a sub-millimetre sensitivity, industrially manufactured eddy-current array (ECA) probe. The ECA probe used was developed for the detection of 0.75 mm surface breaking defects in Ti6-4. The probe was designed to balance sensitivity, probe coverage and cost reflecting typical industrial requirements.

The first study tested the sensitivity variation experienced by the probe as a function of the target defect position beneath the array elements. The results demonstrate Gaussian sensitivity bell curves beneath array elements exhibiting sensitivity minima at the cross-over point between neighbouring array elements. The

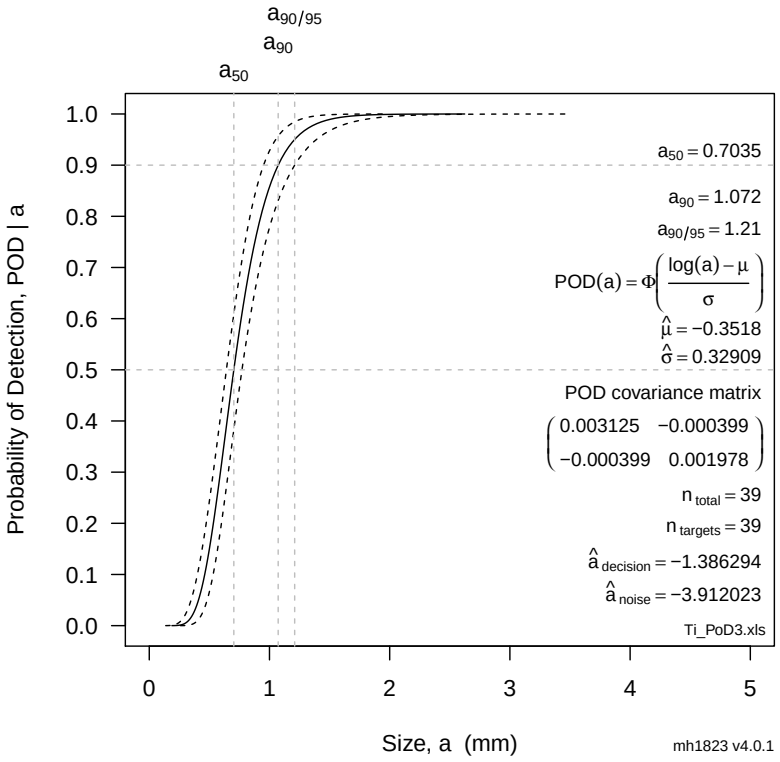


Figure 4.11: Probability of detection curve for $a_{thresh} = 0.2\ mV$ as calculated using MH1823 software in "R" [154].

variation will be dependant on the size of the target defect relative to the size of the array elements and the pitch between staggered rows of elements.

A range of potential signal responses from the target defect poses a problem for the industrial application of an ECA probe when considering how to define a reject threshold for inspections. A potential solution was proposed whereby the root-mean squared (rms) signal response of the ECA to the target defect is calculated and used to set the reject threshold for the remainder of the study to reflect expected industrial procedure.

A probability of detection (PoD) study was performed on the ECA probe to establish the smallest defect size reliably detectable by the probe. 39 fatigue cracks in Ti6-4 samples were inspected and PoD analysis performed on their signal responses. For a decision threshold set by the rms average of the ECA signal response

from an EDM notch of target dimensions (as detailed in the previous paragraph), the smallest defect statistically detectable by the ECA probe was calculated as being $a_{90/95} = 1.21\ mm$. This is significantly larger than the required defect sensitivity.

The analysis of the limitations of the ECA probe forms a benchmark for the development of more sensitive ECA probes. Typical methods for improving the sensitivity of ECA probes include using smaller array elements and more staggered rows. However, each of these introduces more complexity into the probe and thus increases the cost of design, manufacture and operation. More coils require a greater number of multiplexing channels which typically comes at a greater cost or reduces the array coverage. Research into improving the sensitivity of probes without the need for more complex probe designs is presented in the following chapters.

# Chapter 5

# Resonance Behaviour: Preliminary Investigations

## 5.1 Introduction

Electrical resonance has long been exploited for many applications across a wide range of technologies and applications, including radio engineering and wireless power transfer [156]. It has also had some attention for non-destructive ECT applications, in particular for proximity sensing and passive measurements [74, 147, 157, 158, 159]. However, typical ECT systems used in industry avoid electrical resonance for theoretical simplicity, measurement stability and historical reasons. When the local environment around an inductor changes, the largest changes in impedance are observed at the frequencies around electrical resonance. For this reason it is theorised that greater sensitivity and defect information can be obtained by understanding and exploiting the behaviour of electrical resonance. This chapter experimentally explores the behaviour of the electrical resonance of a typical ECT coil as a result of changes in its environment and constituent circuit components.

## 5.2 Theory

As the frequency of excitation is increased, the inductive reactance within a coil will increase proportionally ($X_L = \omega L$). The rate of change of the electric field within the coil increases with frequency generating a greater primary magnetic field via Ampéres law, which will have a knock-on effect on the eddy-current density and thus the changes, due to defect signals, will be greater. In addition the standard depth of penetration decreases with frequency, so that smaller shallower defects are a greater obstacle to higher frequency currents. Both these points mean that higher frequencies are preferable when inspecting for small surface defects [45]. However, this trend does not continue indefinitely and reaches a limit determined by the resonant frequency of the system or when surface roughness of the component becomes comparable to the skin depth.

As shown in section 3.7 eddy-current coils undergo electrical resonance at a certain frequency. This resonant frequency, $\omega_0$, will occur, based on the simplified coil model of section 3.7 when,

$$\omega_0 = 2\pi f_0 = \sqrt{\frac{1}{L_0 C_0} + \left(\frac{R_0}{L_0}\right)^2} \tag{5.1}$$

At $\omega_0$ the impedance, $Z$, of the coil tends towards a maximum and as a consequence the voltage across the coil increases to maintain the same current flow, via Ohm's law. As a result the power into the system at resonance increases proportionally with impedance,

$$P = IV = I^2 Z \tag{5.2}$$

Beyond resonance, the impedance is dominated by the capacitive effects in the coil or cable [123], and it will cease to measure changes in the inductive component effectively. As discussed in section 3.7.3, the presence of an electrically conducting material will have an effect on the resonant circuit such that the resonant frequency

can be roughly approximated to [147],

$$\omega_0 = 2\pi f_0 \approx \sqrt{\frac{1}{L_0 C_0 (1 - k^2)}} \tag{5.3}$$

The magnitude of the electrical impedance of a coil in two states; in air and on the surface of undamaged Ti6-4 are shown in Figure 5.1.

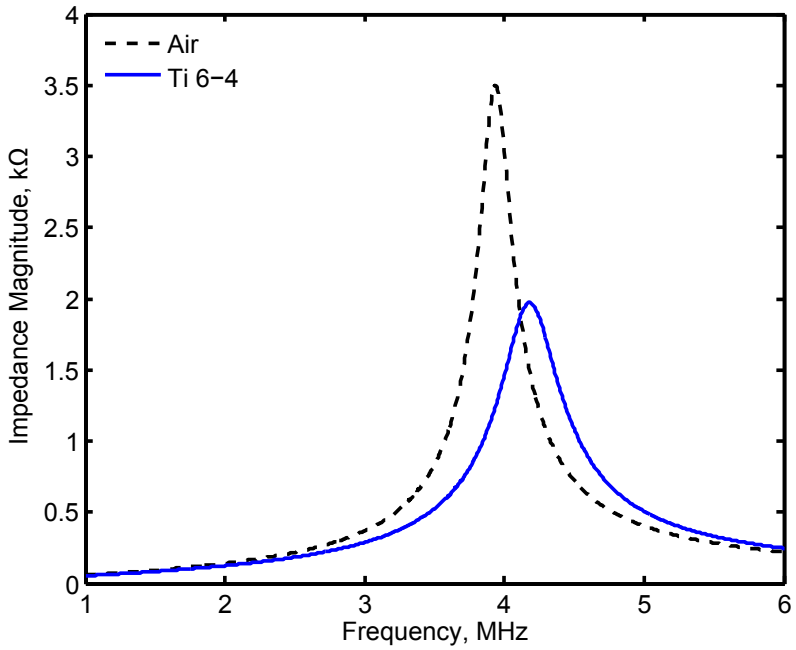


Figure 5.1: Experimentally measured impedance, $|Z|$, magnitude between 1-5MHz, of an ECT probe in air and at zero lift-off above undamaged Ti6-4 showing the impedance maximum at electrical resonance of each system. The systems go through electrical resonance a $f_0 = 3.93 \pm 0.01$ MHz, $f_{Ti6-4} = 4.17 \pm 0.01$ MHz.

A variation in the inductance, capacitance or the coefficient of electromagnetic coupling, $k$, between the coil and the material will result in a resonant frequency shift of the system. The coupling coefficient embodies many of the variable parameters of the coupled system, i.e. material conductivity, magnetic permeability, lift-off, material surface finish, tilt and temperature, all of which will influence coupling. As with any resonating system, even slight changes to any of these parameters can have a large effect on the amplitude of oscillation (i.e. the voltage).

Three preliminary studies were carried out to investigate how coaxial cable length, coil lift-off, and material discontinuities affect the electrical resonance of a typical ECT probe setup.

## 5.3 Co-axial Cable Length

The impedance frequency spectrum, $Z(f)$, of varying lengths of co-axial cable, was measured to determine the effects on electrical resonance and compared to the theoretically predicted resonant frequencies derived from transmission line theory. The formula from section 3.7.2 was used to calculate the impedance, $Z_\tau$, of a transmission line system of unit length, $n$.

$$Z_\tau(n) = Z_c + \cfrac{1}{Y_c + \cfrac{1}{Z_\tau(n-1)}}, \tag{5.4}$$

### 5.3.1 Experimental Parameters

An Agilent (Santa Clara, USA) A4294A Impedance Analyser was used to measure the impedance frequency spectrum $Z(f)$ of 51 RG58, 50Ω, coaxial cables of varying lengths over a frequency range from 40 Hz to 110 MHz. The impedance spectrum of each cable length was measured for two different termination methods: Terminated with an arbitrary inductance load coil of impedance $Z_L$, and a shorted terminated i.e. no load.

#### Coaxial Cable

The key physical parameters of the RG58 50Ω co-axial cable are given in table 5.1. The cable core and shield were each made up of strands of wire. This is used to reduce the influence of the skin-effect and to improve cable flexibility. However, to aid calculations, the geometry of the coaxial cable was assumed to be made up

of a single bodied core and a single bodied shield (see section 3.7.2) of dimensions shown in table 5.1. These properties were used to calculate values for the unit resistance, $R/h$, inductance, $L/h$, and capacitance, $C/h$, using equations 3.68-3.70. The resulting calculated unit component values (table 5.1) were used to simulate the frequency spectrum of the system impedance for increasing cable length.

Table 5.1: Physical properties of RG58, 50Ω coaxial cable, RS Part 6655870 - RG58 C/U PVC [1].

| **Property** | **Value** | **Units** |
|---|---|---|
| Unit Capacitance, $C/h$ | $100 \pm 5$ | $pF.m^{-1}$ |
| Conductor Resistivity, $\rho$ (tinned Copper)[1] | $15.4 \pm 0.1$ | $n\Omega.m^{-1}$ |
| Core Diameter, $a$ | $0.90 \pm 0.10$ | $mm$ |
| Shield Diameter, $b$ | $2.95 \pm 0.10$ | $mm$ |
| Dielectric constant, $\epsilon$ (Solid Polyethylene)[1] | $2.3\epsilon_0 = 20.36$ | $pF.m^{-1}$ |
| Dielectric Permeability, $\mu$ (Solid Polyethylene)[1] | $\approx \mu_0 = 1.257$ | $\mu H.m^{-1}$ |
| **Calculated Properties** | | |
| Predicted Unit Capacitance, $C/h$ | $105 \pm 1$ | $pF.m^{-1}$ |
| Predicted Unit Inductance, $L/h$ | $237 \pm 3$ | $nH.m^{-1}$ |
| Predicted Unit Resistance, $R/h$ | $\frac{1}{\delta_s} 7.1 \pm 0.3$ | $\mu\Omega.m^{-1}$ |

[1]Kaye and Laby [160]

$\delta_s$ = standard depth of penetration in the core.

### Load Coil

An air cored solenoid coil of inductance $L_L = 3.06 \pm 0.06\ \mu H$ was used as an impedance load, $Z_L$, for various lengths of coaxial cables. The key parameters of the coil are shown in table 5.2. The electrical properties were measured using the Agilent (Santa Clara, California, USA) A4294A Impedance Analyser.

The resistance of the coil was assumed to be negligible compared to the reactive components i.e. an ideal inductor.

Table 5.2: Physical properties of load coil, $Z_L$.

| **Physical Properties** | **Value** | **Units** |
|---|---|---|
| Number of Turns, $n$ | 53 | |
| Number of Layers, $N$ | 4 | |
| Wire Diameter, $t$ | 0.08 | $mm$ |
| Core Material | Air | |
| Core Diameter, $d_{in}$ | $1.5 \pm 0.1$ | $mm$ |
| Outer Diameter, $d_{out}$ | $2.0 \pm 0.1$ | $mm$ |
| Coil Height, $h$ | $2.0 \pm 0.2$ | $mm$ |
| **Measured Electrical Properties** | | |
| Inductance, $L_L$ | $3.06 \pm 0.06$ | $\mu H$ |
| Resonant Frequency, $f_0$ | $60.0 \pm 0.3$ | $MHz$ |
| Self-Capacitance, $C_s$ | $2.30 \pm 0.05$ | $pF$ |

### 5.3.2 Experimental Results

The impedance of the load coil was measured using the impedance analyser to determine the coils electrical properties shown in table 5.2. Figure 5.2 shows the impedance magnitude, $|Z|$, of the coil with no coaxial cable connection ($0m$) and with a $5.86 \pm 0.02$ $m$ coaxial cable connection.

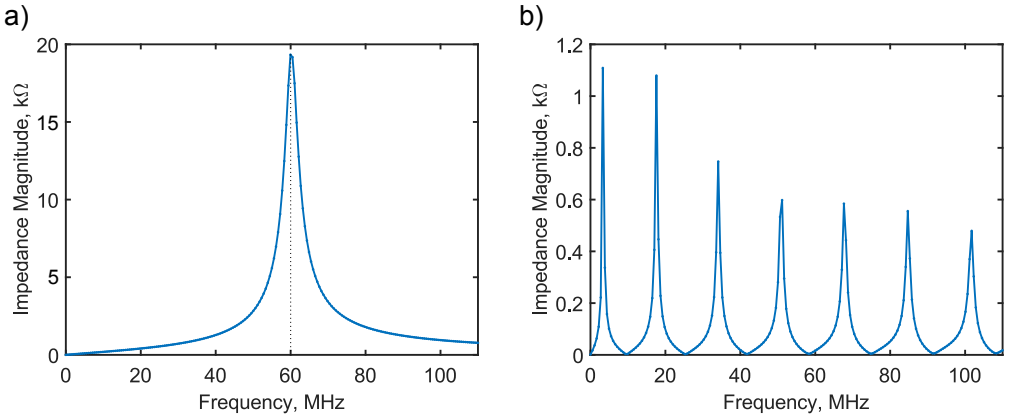


Figure 5.2: Impedance magnitude frequency spectrum of load coil in air with a) No cable ($0$ $m$), and b) a coaxial cable length of $5.86$ $m$.

The measured impedance frequency spectrum of the load coil, $Z_L(f)$, (figure 5.2.a) was used in the subsequent transmission line simulation.

Transmission line theory was used to simulate the effects of coaxial cable length on the resonant frequency of the probe and compared to experimental measurements of cables with a load coil (of properties shown in table 5.2) and with a shorted end (coaxial core and shield connected at the end of the cable). The simulated frequency spectrum maps for the loaded and shorted cables cases are shown in figure 5.3.a & b respectively.

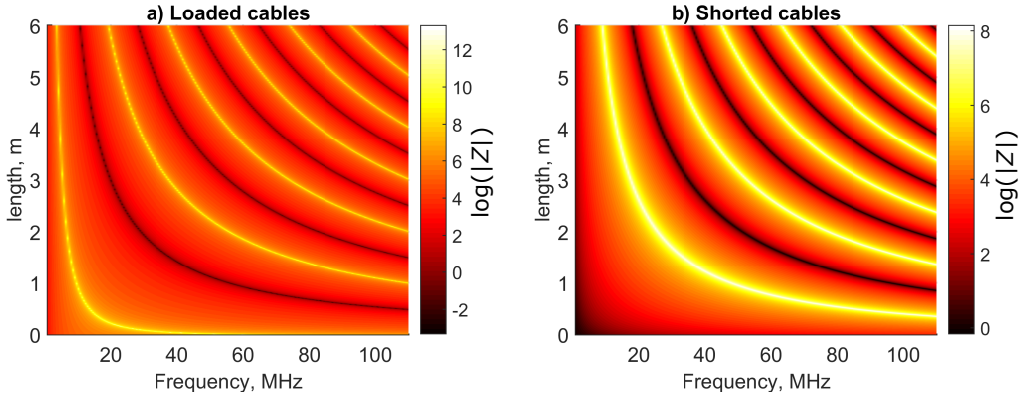


Figure 5.3: Simulated map of coaxial cable length vs impedance magnitude frequency spectrum, $\log(|Z(f)|)$, of a) coil loaded and b) shorted, coaxial cables of different lengths.

The transmission line approximation in equation 5.4 simulates the multiple resonant frequencies of long coaxial cable as experimentally observed in figure 5.2. The fundamental (first) resonant frequency, $f_0$, of the simulated results (from figure 5.3) and the experimental results are plotted for comparison in figure 5.4 for both the loaded and shorted cases.

The transmission line theory calculation of the fundamental resonant frequency is very accurately represented by the lumped circuit model approximation such that,

$$f_0 \approx \frac{1}{2\pi}\sqrt{\frac{1}{L_L(C_s + hC_n)}}, \tag{5.5}$$

where $C_s$ is the self capacitance of the coil, $h$ is the length of the coaxial cable, and $C_n$ is the unit capacitance of the coaxial cable.

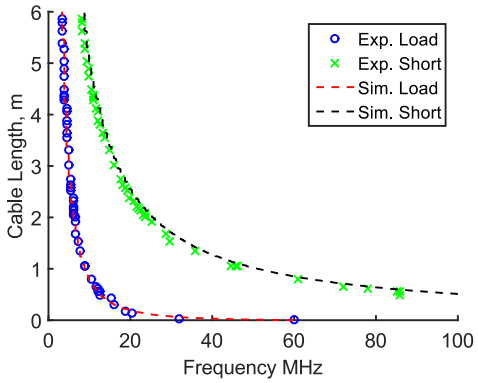


Figure 5.4: Fundamental resonant frequency of the system as a function of cable length for coil loaded and shorted systems showing experimental and transmission line simulated results.

### 5.3.3 Discussion & Analysis

The resonant frequency prediction of the transmission line simulation is in good agreement with the experimental measurements. The experimental resonant frequency measurements have a standard deviation from the predicted values of $\sigma_{load} = \pm 1.5$ MHz and $\sigma_{short} = \pm 1.8$ MHz. These errors incorporate inconsistencies in the length measurement but do not reflect the variation in capacitive instability of systems with shorter, compared to longer, cables. These instabilities are demonstrated by the residual plot in figure 5.5 where the deviation of the measured from the predicted results is greater for shorter cable lengths.

Shorter cables ($h < 1$ m) have a greater effect on the resonant frequency of the system as they contribute a greater proportion of the total capacitance of the system. As the cables get longer additional length provides a rapidly diminishing proportion of the total capacitance of the system. As a result, slight discrepancies in the length of shorter cables will lead to more significant variations from predicted values. This is equally true for slight changes in the quality or surrounding environment of the cables. A change to the outside environment of the cable produces a change in the parasitic capacitance of the coaxial shield thereby affecting the overall capacitance. This is proportionally more significant for shorter cables than longer

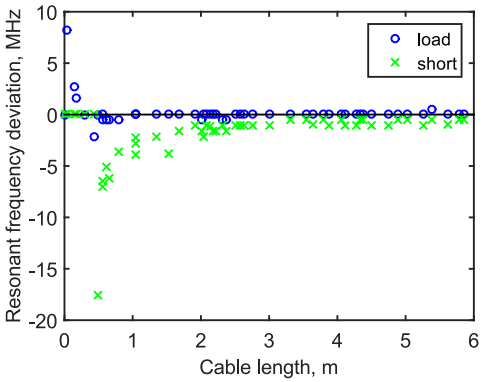


Figure 5.5: Residuals: Deviation of experimental measurements from simulated resonant frequency predictions for coil loaded (blue circles) and shorted coaxial cables (green cross).

cables. All these factors can lead to instabilities in the resonant frequency of the system for short cable lengths.

The magnitude of the simulated impedance was significantly less accurate, but the transmission line simulation is shown to be an accurate method for predicting the resonant frequency of the system.

Although the coaxial cable capacitance is a significant component of the ECT system and its electrical resonance behaviour, the main component of interest in ECT inspections is the inductive coil and it's interaction with the test material.

## 5.4 Inductive Resonance Shifting

Two additional studies were carried out exploring the behaviour of the electrical resonance of an ECT probe due to changes in the inductive coil environment. The first investigated the effect of probe lift-off from the surface of a non-ferromagnetic aerospace superalloy (Ti6-4). The second study investigated the effect of material discontinuities in Ti6-4 on the electrical resonance of the probe.

### 5.4.1 Experimental Parameters

A single coil GE (Coventry, UK) ECT pen probe (Part No. 379-012-060) was used to investigate how some of the typical contributors to ECT signals affect the electrical resonance of an ECT LCR system. The physical and electrical properties of the probe are shown in table 5.3 and a cross-sectional X-ray CT image is shown in figure 5.6. The probe was operated using a $1.54 \pm 0.02$ $m$ long RG174, 50Ω coaxial cable of unit capacitance $C_n = 101$ $pFm^{-1}$. The properties of the RG174 coaxial cable are shown in table 5.4.

Table 5.3: Physical and electrical properties of eddy-current probe used to measure inductive resonance shifting phenomenon, $Z_L$.

| **Physical Properties** | **Value** | **Units** |
|---|---|---|
| Number of turns, $n$ | 38 | |
| Number of layers, $N$ | 5 | |
| Wire diameter, $t$ | $0.10 \pm 0.01$ | $mm$ |
| Core material | Ferrite* | |
| Core diameter, $d_{in}$ | $1.02 \pm 0.01$ | $mm$ |
| Coil outer diameter, $d_{out}$ | $2.19 \pm 0.01$ | $mm$ |
| Coil height, $h$ | $0.84 \pm 0.01$ | $mm$ |
| Inherent lift-off, $l_0$ | $0.59 \pm 0.01$ | $mm$ |
| Coil thickness, $\tau$ | $0.52 \pm 0.01$ | $mm$ |
| **Electrical Properties** | | |
| Coil inductance, $L_L$ | $10.34 \pm 0.09$ | $\mu H$ |
| Cable capacitance, $C_c$ | $158.4 \pm 0.5$ | $pF$ |
| Resonant frequency (air), $f_0$ | $3.93 \pm 0.01$ | $MHz$ |

*Specific ferrite grade unknown

The Agilent A4294A impedance analyser was used to measure the magnitude, $|Z|$, and phase, $\phi$, of impedance as a function of frequency for the probe in air, $Z_0(f)$. The same measurement was made for the probe in contact and normal to the surface of Ti6-4 (lift-off = 0.0 $mm$, tilt angle = $0 \pm 1°$ with reference to figure 2.2). Each measurement was made between 1-5 MHz The complex impedance components of the probe in these two environments are shown in figure 5.7.

In air, the electrical resonance of the probe occurs at frequency $f_0 = 3.933 \pm$

Table 5.4: Physical properties of RG174, 50Ω coaxil cable, RS Part 665-5855 - RG174 A/U PVC [2].

| **Property** | **Value** | **Units** |
|---|---|---|
| Unit Capacitance ($C/h$) | $101 \pm 5$ | $pF.m^{-1}$ |
| Conductor Conductivity, $\sigma$ (Copper clad steel) | 23.2 | $MS.m^{-1}$ |
| Core Diameter, $a$ | $0.49 \pm 0.01$ $mm$ | |
| Shield Diameter, $b$ | $1.52 \pm 0.08$ $mm$ | |
| Dielectric constant, $\epsilon$ (Solid Polyethylene) | $2.3\epsilon_0 = 20.36$ | $pF.m^{-1}$ |
| Dielectric Permeability, $\mu$ (Solid Polyethylene) | $\approx \mu_0 = 1.257$ | $\mu H.m^{-1}$ |

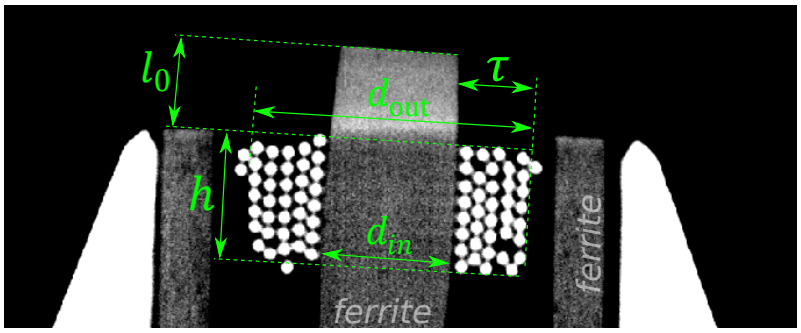


Figure 5.6: X-ray computed tomography (CT) cross-sectional image of the ECT probe coil around a ferrite core and surrounded by a ferrite shield. Core diameter $d_{in} = 1.02 \pm 0.01$ $mm$, coil outer diameter $d_{out} = 2.19 \pm 0.01$ $mm$, coil height $h = 0.84 \pm 0.01$ $mm$, intrinsic lift-off $l_0 = 0.59 \pm 0.01$ $mm$ and coil thickness $\tau = 0.52 \pm 0.01$ $mm$.

0.005 $MHz$. The properties of electrical resonance for these two probe environments are compared in Table 5.5. The resonant frequencies were calculated via the crossing point of the impedance phase for each case.

For the case of the probe being in the proximity of a non-ferromagnetic material, such as Ti6-4, the impedance maximum at resonance decreases with proximity to the material surface and the resonance frequency shifts to higher frequencies (figure 5.7). This is analogous to a reduction in the inductance and an increase in the resistance of the system. Using the experimental system described above, two further studies were carried out on the behaviour of the probes electrical resonance in the presence of Ti6-4. The first investigated the effect of lift-off from the material

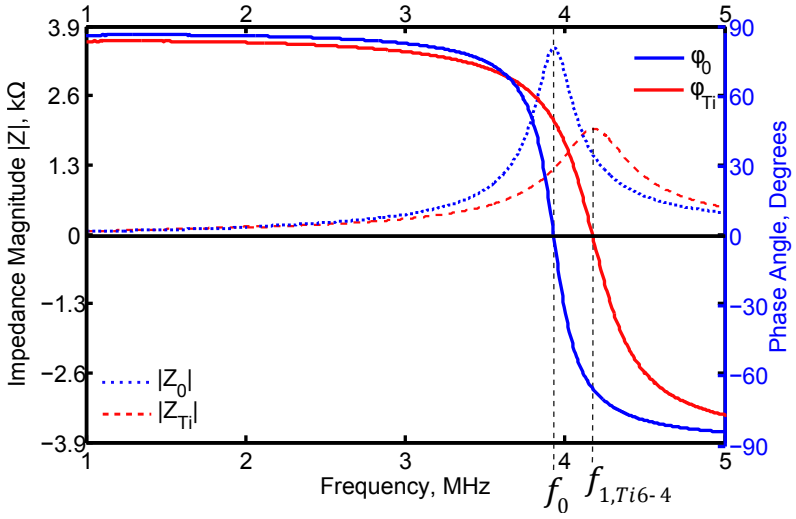


Figure 5.7: Experimentally measured magnitude and phase of complex impedance for the ECT probe in Air (blue) and with zero lift-off above Ti6-4 (red) showing the electrical resonance in air ($f_0 = 3.933 \pm 0.005$ MHz) and on Ti6-4 ($f_1 = 4.17 \pm 0.005$ MHz).

Table 5.5: Key properties of electrical resonance for the system in air, and positioned at zero lift-off on the surface of undamaged Ti6-4.

| **Material** | $f_0$ ($\pm 0.005$ $MHz$) | $\lvert Z_0(f_0)\rvert$ ($\pm 0.01$ $k\Omega$) | Q-factor ($\pm 0.1$ $dim.$) |
|---|---|---|---|
| Air | 3.933 | 3.50 | 17.5 |
| Ti 6-4 | 4.173 | 1.97 | 10.3 |

surface and, the second explored the effect of discontinuities in the material surface on the electrical of the probe system.

### 5.4.2 Lift-off Behaviour

The impedance frequency spectrum, $Z(f)$, of the ECT probe, defined in table 6.5, was measured as a function of lift-off from the surface of undamaged Ti6-4.

#### Experimental Setup

The ECT probe was secured into a sliding stage so that the probe was orientated parallel to the sliding rail. The test sample was secured into a stage which was

locked in place on the sliding rail facing the probe head. This limited the relative probe tilt angle to $0 \pm 1°$.

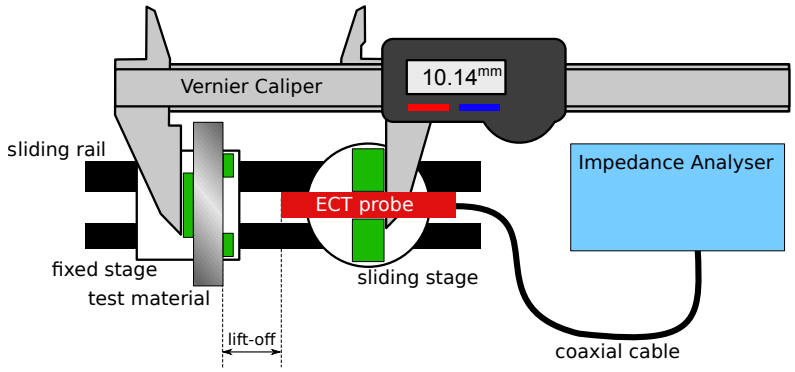


Figure 5.8: Schematic diagram of lift-off investigation experimental setup.

A digital Verneir Caliper was used to measure the lift-off separation between the probe head and the material surface. The two arms of the caliper were fixed to the two stages and the digital reader was zeroed when the probe head and material surface were brought into firm contact. The first measurement was made with the probe in firm contact with the material surface, with no protective tape over the tip of the probe in order to measure the maximum resonance shift possible for the probe (true zero lift-off). A protective Teflon tape layer (of thickness ≈0.1 mm) was then applied to the tip of the probe and another impedance spectrum measurement made for the taped probe in firm contact with the material. This measurement replicates typical industrial ECT arrangements and will be referred to as "industrial zero lift-off", $f_{Ti,0i}$, until further notice the probe was then moved away from the surface of the material, starting at increments of ≈0.1 mm, and recording the actual lift-off for each measurement from the Verneir Caliper. Figure 5.8 shows the experimental setup for the study.

**Results & Discussion**

Figures 5.9 shows the change in maximum impedance magnitude, $|Z_0|_{max}$, the resonant frequency, $f_0$, and the quality factor, $Q_0$, of the system with increasing lift-off. The resonant frequency and peak impedance magnitude of the probe on Ti6-4 at true zero lift-off are referred to as $f_{Ti,0}$ and $|Z_{Ti,0}|$ respectively. The same values for industrial zero lift-off are referred to as $f_{Ti,i0}$ and $|Z_{Ti,i0}|$ respectively, until stated otherwise.

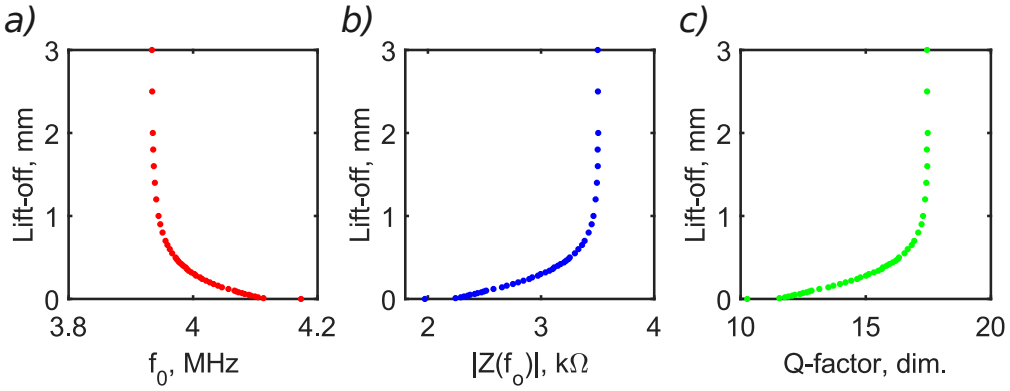


Figure 5.9: Experimentally measured resonant frequency (a), impedance magnitude (b) and Q-factor (c) of the ECT probe as a function of lift-off from the surface of undamaged Ti6-4.

As is shown in figure 5.9, for a lift-off greater than approximately 1.5 $mm$ the magnitude and the resonant frequency are equivalent to that in air, and the probe will cease being influenced by the material beneath it. It is clear from figure 5.9 that the change in peak impedance and quality factor due to lift-off are directly proportional to one another, and have a linear relationship of the form, $|Z_0| = q_1 Q_0 + q_2$, where $q_1 = 4.70 \pm 0.01\ k\Omega$ and $q_2 = 1.02 \pm 0.04\ k\Omega$. The fit is in excellent agreement with the data, with a root mean squared error of $\sigma_{rms} = 0.02\ k\Omega$.

Figure 5.10 shows the relationship between experimentally measured impedance peak and resonant frequency identifying the direction of lift-off and the features of the system; in air, at true zero lift-off, and industrial zero lift-off. At a small lift-off from the surface (0-0.25 mm) the change in resonant frequency and impedance

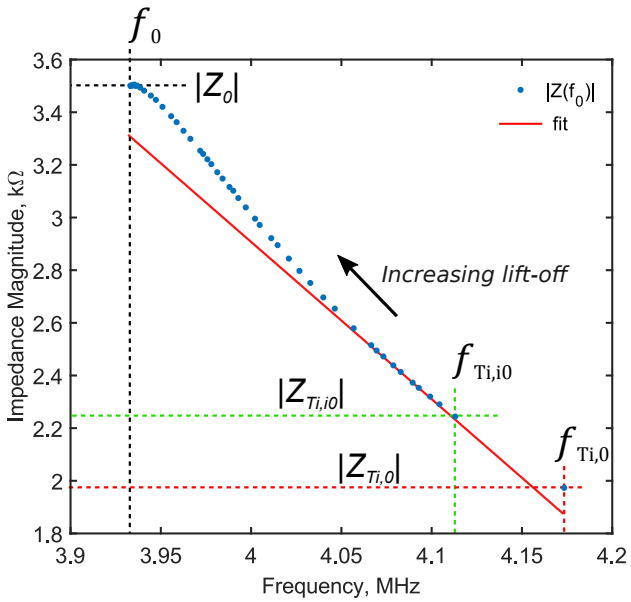


Figure 5.10: Experimental impedance peak magnitude vs resonant frequency as a function of lift-off from the surface of undamaged Ti6-4. Plot shows linear fit to small lift-off region and indicates the probe resonance peak in air ($f_0$ & $|Z_0|$), at true zero lift-off ($f_{Ti,0}$ & $|Z_{Ti,0}|$), and at industrial zero lift-off ($f_{Ti,i0}$ & $|Z_{Ti,i0}|$).

peak are approximately linear, as shown by the best fit in figure 5.10. The parameters of the linear fit, of the form $|Z_0| = a_1 f_0 + a_2$, are $a_1 = -5.9 \pm 0.2\ k\Omega s$ and $a_2 = 26.7 \pm 0.7\ k\Omega$. The fit is in excellent agreement for small lift-off distances, with a root mean squared error of $\sigma_{rms} = 0.004\ k\Omega$.

It can be seen in both figure 5.9 & 5.10 that there is a significant shift in the resonance between the industrial zero (≈0.1 mm) and true zero lift-off positions. This may be due to the probe achieving magnetic and electrical contact with the material surface. As such there will be a greater level of magnetic coupling with the sample causing a significant jump in the resistive and reactive components as well as removing any stray parasitic capacitive between the ferrite core and the material surface. Further work and finite element modelling is likely to be required to properly characterise this behaviour, however this was outside the scope of this thesis.

In order to properly represent industrial ECT measurements, a layer of

Teflton tape is used on the tip of the measurement probe for all subsequent investigations unless stated otherwise. As such, industrial zero lift-off will now be more simply referred to as zero lift-off. The next section explores the resonance behaviour in the presence of artificial material discontinuities.

### 5.4.3 Material Discontinuities

The effects of discontinuities in the test material on the ECT probe impedance was investigated by positioning the probe above long, wire-cut slots and measuring the impedance of the system as a function of frequency.

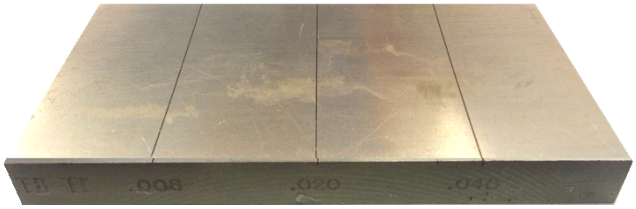


Figure 5.11: Calibration block. Image of a Ti64 test specimen and the three notches of increasing depth.

#### Experimental Setup

Three large calibration slot discontinuities in a Ti6-4 specimen (pictured in figure 5.11) were inspected to investigate the effects of resonance-shifts on discontinuity signals. The slots spanned the width of the test sample, had equal gapes of 0.5 mm, and depths of 0.20, 0.50 and 1.00 mm (0.008, 0.020 and 0.040 inches respectively). These machined discontinuities are not representative of real material cracks but are a useful starting point for investigating the behaviour of resonance in the presence of discontinuities. The same ECT probe, as shown in figure 5.6, was used with the probe tip covered in a layer of protective Teflon tape to mimic typical industrial inspection conditions.

**Results & Discussion**

The impedance magnitude frequency spectra are shown in figure 5.12 for; the probe on undamaged material, and at zero lift-off, positioned directly above the centre of the three slot gapes. Inaccuracies in positioning the probe directly above the centre of the discontinuities were estimated to be $\pm 0.5\ mm$.

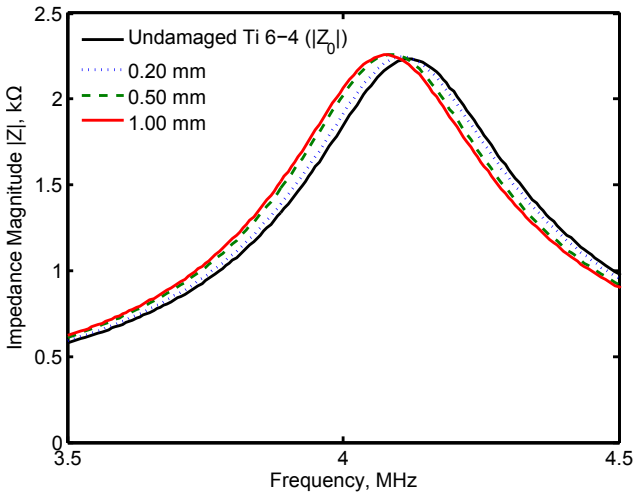


Figure 5.12: Impedance magnitude frequency spectrum of ECT probe on undamaged Titanium 6-4 and above 3 long slots of varying depth in the same material: Undamaged (solid black), 0.20 mm deep (dotted blue), 0.50 mm deep (dashed green), and 1.00 mm deep (solid red).

The discontinuities (material loss or eddy-current path obstruction) in the Ti6-4 cause a change in the equivalent components of the effective circuit model for the ECT probe system (see section 3.7.3). This results in a shift in the resonant frequency and a change in peak amplitude of the system. The key features of resonance for each of the impedance spectra are summarised in table 5.6 and the path of the resonance peak due to discontinuities displayed in figure 5.13 relative to the path due to lift-off from section 5.4.2.

Figure 5.13 demonstrates that material discontinuities produce different resonance behaviour to lift-off, thereby making it possible to differentiate between lift-off and discontinuities changes. The discontinuities measured in this study cause trace-

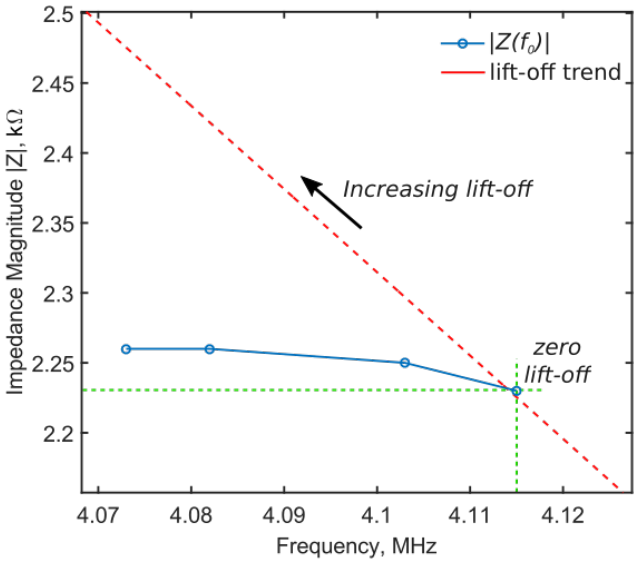


Figure 5.13: Experimental impedance peak magnitude vs resonant frequency as a function of discontinuity depth in Ti6-4. Plot shows the linear path of the impedance peak due to small lift-off distances (red dotted) and indicates the probe resonance peak at industrial zero lift-off.

able downward shifts in the resonant frequency of impedance whilst exhibiting only small changes in the peak impedance magnitude and maintaining approximately the same Q-factor (see table 5.6). This implies that the inductive component of the equivalence circuit model increases, i.e. a reduction in the coefficient of coupling (see section 3.7.3), whilst the resistive component is relatively unaffected.

Frequencies approaching the electrical resonance exhibit the greatest impedance

Table 5.6: Key properties of electrical resonance for the system in air, and positioned at zero lift-off on the surface of undamaged Ti6-4.

| **Discontinuity** | $f_0$ $(\pm 0.005\ MHz)$ | $Peak\ \|Z\|$ $(\pm 0.01\ k\Omega)$ | **Q-factor** $(\pm 0.1, dim.)$ |
|---|---|---|---|
| 0.0 mm | 4.115 | 2.23 | 11.5 |
| 0.2 mm | 4.103 | 2.25 | 11.5 |
| 0.5 mm | 4.082 | 2.26 | 11.5 |
| 1.0 mm | 4.073 | 2.26 | 11.5 |

changes, relative to the undamaged Ti6-4 impedance. This is more clearly observed once the "background" impedance of the undamaged Ti6-4 is subtracted from the impedance measurements of the probe above the slots (figure 5.14).

Figure 5.14 shows the background subtracted frequency spectra for the magnitude and phase of the complex impedance. It is clear from the results that the signal intensity from a discontinuity is greater at frequencies close to electrical resonance compared to standard operational frequencies (1-3 MHz).

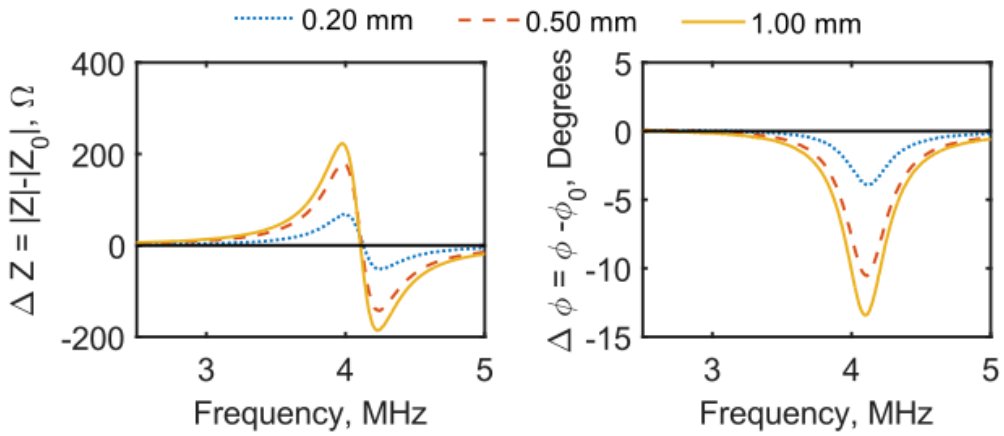


Figure 5.14: Difference in the impedance frequency spectrum of the ECT probe above 3 long slots of varying depth in the same material: 0.20 mm deep (dotted blue), 0.50 mm deep (dashed red), and 1.00 mm deep (solid yellow). Showing the change in impedance magnitude (left) and impedance phase (right).

The resonance shifting phenomenon results in a signal enhancement within a band of frequencies immediately below the resonant frequency, for impedance magnitude ($|Z|$), and around electrical resonance, for impedance phase ($\phi$).

### 5.4.4 Errors

The major source of error in each of these preliminary studies was the positioning of the probe. This is particularly significant for positioning the probe above the discontinuities. If the probe is not correctly positioned at the point where the maximum disruption to the mutual induction occurs then the resonance shift will

be misrepresented.

### 5.4.5 Resonant Noise

The key factor in determining whether operating at frequencies close to electrical resonance is viable for ECT inspection is resonant noise. In this thesis, resonant noise refers, not to electrical background interference but, to variable background shifting of the resonant frequency caused by unwanted external physical influences i.e. probe lift-off and tilt etc. Many physical parameters will influence the resonant frequency of the system, some of which have been investigated in this section. However, there are many other factors that can cause the resonant frequency to shift slightly thereby causing noise at near-electrical-resonance (NER) frequencies. A list of the main factors that could influence the electrical resonance of the system during an inspection are given in table 5.7.

If these parameters are allowed to fluctuate too much, such that the background resonant frequency shift is equivalent to shifts caused by discontinuities, then the signal enhancement will be accompanied by an equivalent enhancement of the background noise. This will negate any potential signal-to-noise improvement that could be gained from exploiting the effects of defect resonance shifting.

## 5.5 Conclusions

Variations in the electromagnetic environment of an ECT probe, alters the frequency and magnitude of its electrical resonance. This shifting leads to the large changes in the electrical properties of the system at near-electrical-resonance (NER) frequencies when the system encounters any disturbance i.e. changes in lift-off from a sample, or material discontinuities.

It has been shown that the resonant frequency of an ECT probe is highly influenced, in a predictable way, by changes in the coaxial cable capacitance. It

was observed that lengths greater than $1.0m$ of standard coaxial cable produce resonance frequencies in very good correlation with theoretical values calculated using transmission line theory. Shorter coaxial cable lengths produce greater instabilities in resonance which can be detrimental for maintaining a reliable resonant frequency.

Probe lift-off from the surface of a typical aerospace material, Titanium 6-4, was investigated for a standard ECT probe. For an industrial ferrite cored and shielded ECT probe (diameter $\approx$2 mm), the results show that the electrical resonance is no longer significantly affected by the presence of the test material at a lift-off greater that approximately $1.5mm$. It was also shown that the resonant frequency and peak impedance magnitude, for the geometry and material investigated, exhibit a linear relationship for small lift-off distances.

Material discontinuities also cause resonance shifting behaviour and it was shown that the relationship between resonant frequency and peak impedance magnitude due to discontinuities deviates significantly from that of lift-off. It was therefore hypothesised that this phenomenon could be manipulated to improve the sensitivity of ECT inspections. An investigation was carried out to determine the effect of the resonance behaviour of ECT probes on their sensitivity to discontinuities in superalloy materials. The results are presented in the following chapters.

Table 5.7: Key factors affecting the electrical resonance of an ECT inspection probe.

| **Factor** | **Liftoff** |
|---|---|
| **Causes** | Inaccurate scan setup, instabilities in the scanning system, surface roughness and surface geometry. |
| **Suppression technique** | Spring loaded probe mount or fixed liftoff scanning. |
| **Residual effect** | High frequency surface roughness will still generate some liftoff effects. |

| **Factor** | **Tilt** |
|---|---|
| **Causes** | Probe drag, inaccurate scan setup, instabilities in the scanning system, surface roughness and surface geometry. |
| **Suppression technique** | Rigid, secure probe mount fixture or scanning at a fixed liftoff. Contour adjusting manipulation for complex geometries. |
| **Residual effect** | Surface roughness will still generate some tilt effects. |

| **Factor** | **Coaxial Cable Environment** |
|---|---|
| **Causes** | Short coaxial cables. Unsecured coaxial cables leading to variations in its surrounding environment during inspection. |
| **Suppression technique** | Use longer cables. Secure cables to minimise variations in its environment. |
| **Residual effect** | Some changes in coaxial environment are unavoidable, however, if care is taken the effect on resonance will be minimal especially in longer cable lengths. |

| **Factor** | **Temperature Fluctuations** |
|---|---|
| **Causes** | Variations in ambient temperature or the temperature of the component will change the electrical conductivity of a sample and can lead to an effective change in the electromagnetic response of the material. |
| **Suppression technique** | Well controlled temperature environment, or a high-pass filter. Temperature variations are typically low frequency effects that can be filtered out in post-processing. |
| **Residual effect** | Although a slow drift in resonant frequency can be filtered out it will however also shift the NER frequency region such that a system operating at a single frequency within this range would experience some loss in sensitivity. |

# Chapter 6

# Near Electrical Resonance Signal Enhancement (NERSE)

## 6.1 Introduction

Based on the preliminary investigations presented in chapter 5, a band of frequencies around electrical resonance were highlighted as exhibiting exaggerated discontinuity signal responses. The following chapter presents the early stage research, development and characterisation of a novel ECT technique for enhancing the sensitivity of ECT measurements by exploiting the resonance shifting behaviour of ECT probes in the presence of material discontinuities. Initial investigations examined the frequency spectrum response change of a typical ECT probe in the presence of discontinuities, and analysed the features of such measurements in order to characterise discontinuity geometries (section 6.3).

Research was then performed to optimise and statistically determine the sensitivity of single frequency excitation ECT measurements to real fatigue cracks in Titanium 6Al-4V (Ti6-4) (section 6.4). Analysis was performed on the sensitivity and background noise levels comparing results from inspections using standard operating frequencies, and the novel method presented. An additional study was also

performed to detect grain colony boundaries of $\alpha$-phase (see section 2.5.2) dominant Titanium alloys using this novel method (section 6.5). The details and results of thesis studies are presented in the following chapter.

## 6.2 Experimental Methods

An experimental system was developed to explore the behaviour of near electrical resonance (NER) phenomena on the sensitivity of ECT measurement of surface-breaking defects in Ti6-4. The two main methods of excitation used in this Thesis are chirp excitation (frequency sweeping) and harmonic excitation (single frequency). The following chapter details the experimental equipment and methods of excitation used for this Thesis.

### 6.2.1 Experimental Apparatus

ECT probes were driven using the experimental setup shown in Figure 6.1. With reference to figure 6.1; a Tektronix (Beaverton, Oregon, USA) 3021B arbitrary function generator was used to create a voltage input function, $V_{in}$, signal which was converted into an equivalent drive current by a Howland current source. This current, $I_{in}$, is supplied via coaxial cable to the probe coil which is scanned across the surface of the test material.

Constant light pressure is supplied to the probe head via the probe mount which contains a weighted brass probe holder core with an approximate mass of 0.30kg, which can slide unimpeded within the concentric mount as the scan is performed. This allows the probe head to adapt to slight changes in the surface of the test material. The voltage in, $V_{in}$, and the voltage across the probe, $V_{out}$, is monitored and recorded using an analogue-to-digital (A/D) data acquisition card (with a digitisation rate of $20ns$) and Labview program. The program also controls the XY stage and performs stationary measurements at each point in the scan. The

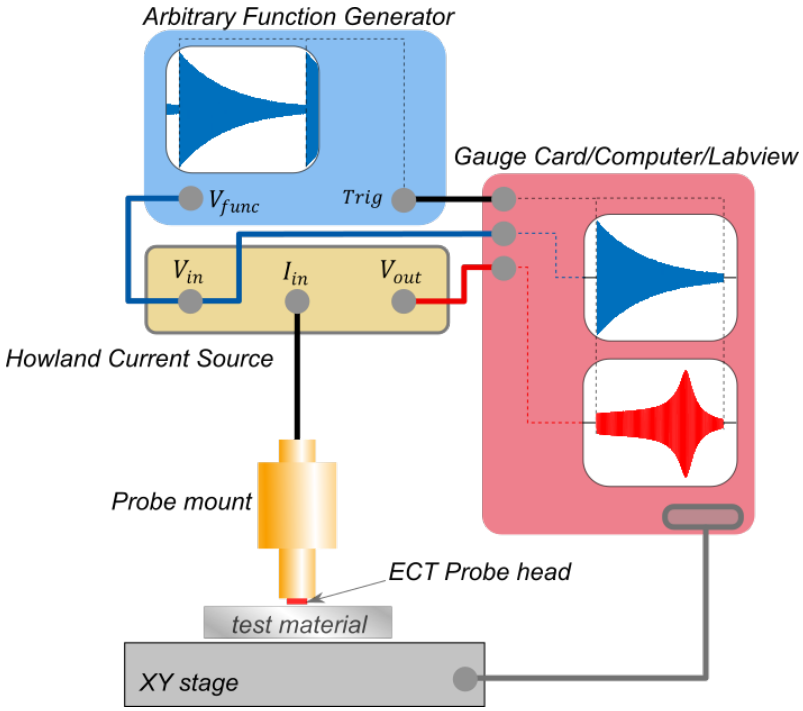


Figure 6.1: Schematic diagram of the experimental set up for a 2D ECT scan. A Function generator outputs a voltage function which a Howland current source converts into an equivalent current function which is sent to the probe. The electrical properties of the probe are monitored via a Labview program as the probe is scanned across the surface of the test specimen.

XY stage has a minimum step increment of $100 \pm 10$ $\mu m$ and the scan resolution set depending on the application.

### Howland Current Source/Pump

The Howland current source (or current pump) [161], built in house, converts the voltage function, $V_{in}$, from the arbitrary function generator into an equivalent current function, $I_{in}$, which is supplied to the load probe, $Z_L$. The source includes a positive and negative feedback system which maintains the current within the probe and so the voltage across the probe ($V_{out}$) changes to adapt to variations in the electrical properties of the probe. The basic circuit design for a Howland current source is shown in figure 6.2.

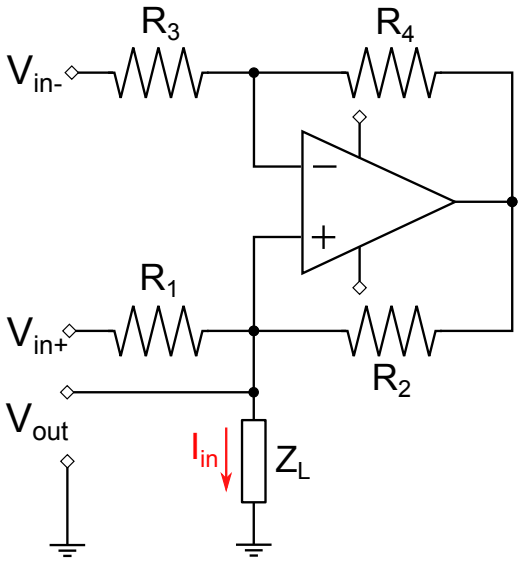


Figure 6.2: Schematic circuit diagram of a basic Howland current source design.

Figure 6.2 depicts the basic Howland current source where,

$$\frac{R_1}{R_2} = \frac{R_3}{R_4}, \tag{6.1}$$

must be satisfied in order for the source to work correctly. The actual current source used was a much more sophisticated design to compensate for some of the instabilities inherent in the non-ideal components, such as resistor mismatching. The current source used in the investigations presented in this thesis has a flat output response over a frequency range of 1-5 MHz with an operational input amplitude range between $\pm 0.5\ V$ corresponding to a $\pm 50\ mA$ output current. For a given frequency excitation the output amplitude stability was measured to be $< \pm 0.6\%$.

### 6.2.2 Excitation Methods

Two different excitation methods were used to investigate the effects of electrical resonance on eddy-current inspection sensitivity, chirp (frequency swept) and harmonic (single frequency) excitation. The details of these excitation modes are presented

in the following sections.

### Chirp Excitation

A chirp excitation approach was used to investigate the frequency range around the electrical resonance of the probe in section 6.3. A chirp refers to a frequency sweep excitation where a range of frequencies are excited sequentially in a continuous controlled function (see section 2.2.5). This was achieved by developing a frequency increasing sinusoidal function in Tektronix Arbitrary Function Xpress software. The equation for a chirp excitation function is,

$$V_{in} = V_0 e^{i\omega(t)t}, \tag{6.2}$$

where $\omega(t)$ is an angular frequency function increasing linearly with time $t$ between the chosen start and end frequencies. This function produces a sinusoidal wave of constant current amplitude steadily increasing in frequency. However, maintaining a constant amplitude of excitation over a large range of frequencies will lead to a steady increase in the output voltage due to the linear relationship between frequency and inductive reactance ($X_L = \omega L$, see section 3.6.1). The output voltage is expressed as,

$$V_{out} = I_{in} Z, \tag{6.3}$$

$$\propto V_{in} Z. \tag{6.4}$$

Very quickly saturation of the dynamic measurement range occurs such that either the measurement range is set too low so that the signal is clipped at higher frequencies, or the range is set higher leading to poor signal resolution at lower frequencies. This is especially important when approaching electrical resonance, as the impedance of the probe deviates from the linear increase with frequency and exhibits a much more dramatic increase, as demonstrated in figure 6.3.

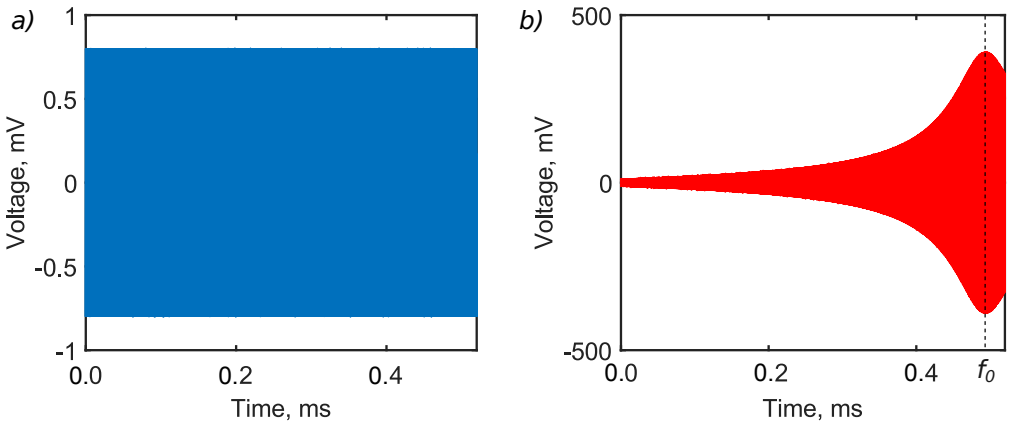


Figure 6.3: Example $V_{in}$ (a) and $V_{out}$ (b) signals for a constant amplitude chirp excitation function, sweeping from 1-5MHz, and exciting a probe resonating at 4.8MHz (peak in b). Sinusoidal oscillations not observable due to the high frequency of excitation.

The solution to this is to use an exponentially decaying excitation function of the form,

$$V_{in} = V_0 e^{i\omega(t)t - \frac{1}{\tau}t}, \tag{6.5}$$

where $\tau$ is a time constant responsible for the decay rate of the amplitude of the exponential function. The value of $\tau$ is determined so as to best fit the impedance magnitude, $|Z|$, over the frequency range of the sweep. This function counteracts the increase in impedance and prevents $V_{out}$ from saturating the dynamic range of the of the detector at higher frequencies. It also offers lower frequencies roughly the same screen height as higher frequencies.

The function generation software outputs a $130 \times 10^3$ point waveform, which the 25 $MS/s$ Tektronix arbitrary function generator converts into a 0.52 $ms$ waveform with a repetition rate of 1923 Hz. Example $V_{in}$ and $V_{out}$ functions are shown in figure 6.4 for a probe with a resonant frequency, $f_0 = 4.8$ MHz, excited from 1-5 MHz, with a decay value, $\tau = 0.5 \times 10^{-3} s$.

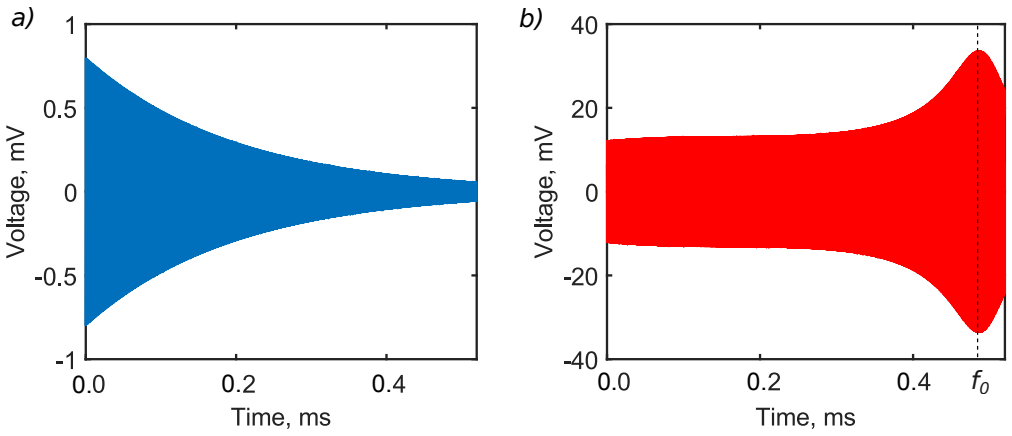


Figure 6.4: Example $V_{in}$ (a) and $V_{out}$ (b) signals for an exponentially decaying amplitude ($\tau = 0.5e-3s$) chirp excitation function(1-5 MHz), exciting a probe resonating at 4.8MHz. Sinusoidal oscillations not observable due to the high frequency of excitation.

### Chirp Analysis

A 2D-scan of the surface of the test material is achieved by positioning the probe at discrete incremental positions within the area of interest and recording $V_{in}$ and $V_{out}$ for one frequency sweep cycle at each point. The computer samples $V_{in}$ and $V_{out}$ at a rate of 50 $MS/s$. In order to sample the whole frequency sweep, lasting 0.52 $ms$, the sample depth of the measurement was set to 26000 Samples. The temporal signal can then be used to calculate the ratio of $V_{out}/V_{in}$ in frequency space, which is proportional to the impedance, via Ohms' law ($V_{in} = I_{in}Z$).

The data for a given point in the scan can be displayed in the frequency spectrum and the spectral response of that measurement analysed. This offers a lot more information about the measurement point and is analogous to spectroscopy and the measurements made using the impedance analyser in chapter 5. Alternatively the data can be frequency collapsed i.e. summed over all frequencies, or over a selected frequency range, to give an effective area under the frequency spectrum curve. This can then be displayed as a c-scan image of the surface of the material.

**Harmonic Excitation**

The harmonic, or single frequency, excitation of the probe is much more straight forward. For this method the excitation function is the same as equation 6.2, except that the $\omega$ term is a single, non time varying, angular frequency. The function generator produces a continuous sinusoidal wave of constant amplitude which is supplied as $V_{in}$. The output function, $V_{out}$, from the coil is a similarly continuous function of consistent amplitude (for any given point measurement). These waveforms can be measured for a predefined number of cycles to average out any incoherent noise and analysed in Fourier space to extract their complex signals.

## 6.3 Chirp NERSE Excitation

An investigation into the effects of operating an ECT probe at near electrical resonance (NER) frequencies was carried out and the results used to draw conclusions as to how the behaviour of resonance, in the presence of simulated material discontinuities, affects the measurement sensitivity.

### 6.3.1 Experimental Parameters

Three long wire cut material discontinuities of varying depth in Ti6-4 (see section 5.4.3) were inspected using the chirp excitation approach outlined in the chapter 6.2. The ECT probe was positioned at zero lift-off (with a Teflon tape protective layer) and with a tilt angle of $0 \pm 1°$. Additional parameters for the 2D scan of the material surface are given in table 6.1.

The $V_{in}$ and $V_{out}$ measurement voltage scale was set so that the maximum amplitude of the measured function extended to 80% of screen height (SH) when at zero lift-off from the test sample. This prevented the signal from being clipped during inspection whilst providing sufficient dynamic range for the measurement.

Table 6.1: Experimental parameters for the near electrical resonance (NER) frequency sweep measurement of 3 long discontinuities of varying depth in Titanium 6-4.

| $V_{func}$ **Parameters** | **Value** |
|---|---|
| Frequency range | 1-5 MHz |
| Repetition rate | 1923 Hz |
| $V_0$ input voltage | 170 $mV$ |
| **C-Scan Parameters** | **Value** |
| X-positions | 200 |
| Y-positions | 20 |
| X increment, $\Delta X$ | 0.25 $mm$ |
| Y increment, $\Delta Y$ | 0.25 $mm$ |

### 6.3.2 Experimental Method

Three notches in the Ti6-4 sample were tested using a single coil probe operated in the absolute mode and swept through frequencies from 1-5 MHz. A 0.52 $ms$ repeating frequency sweep signal was generated using a 25 $MS/s$ arbitrary function generator, to output a driver waveform that satisfies the Nyquist criterion.

The waveform was designed to decrease exponentially with frequency so that the $V_{out}$ signal would not saturate the measurement scale as the frequency approached resonance (Figure 6.4). $V_{in}$ and $V_{out}$ were scaled such that their maxima, when coupled to undamaged Ti 6-4, were equal to 80% of full screen height.

The measured signals, $V_{in}$ and $V_{out}$, were converted into the frequency domain via Fourier Transform and binned (bin width = 1923 Hz) over the full frequency range. The ratio of $V_{out}$ over $V_{in}$ is proportional to the impedance of the system ($Z = V_{out}/I_{in}$ ). In this way a measurement proportional to the complex impedance of the ECT probe, $Z$, over that point is obtained for each position within the XY scan to build an image of the surface.

The C-scan image was zeroed to an area of undamaged material. Figure 6.5 shows a high contrast C-scan image of the test piece surface constructed by the linear summation of data from frequency bins within the frequency range of $1.0 - 4.0$ MHz

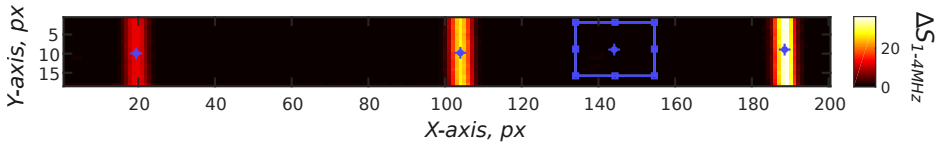


Figure 6.5: Titanium 6-4 calibration block surface Magnitude C-scan image of the background subtracted frequency summation signal between 1-4 MHz ($\Delta S_{1-4MHz}$). Image shows the 3 calibration slots of depth 0.2, 0.5 and 1.0 mm and the measurement points for each discontinuity (blue cross-hairs) and background noise (black solid square).

(avoiding phase inversion after resonance).

### 6.3.3 Results & Analysis

The raw chirp signal data, $S = (V_{out}/V_{in})$, over undamaged material (mean of undamaged area), $S_0$, and for the locations of maximum signal from the 3 discontinuities are shown in all of its measurable components in figure 6.6.

The left window of figure 6.6 shows the impedance magnitude of the probe as it passes through electrical resonance at approximately 4MHz. Shifts in the resonant frequency are observable for measurements made above each of the material discontinuities, in both the magnitude and phase. The degree of shifting increases with increasing discontinuity depth. It should be noted that the resonant frequency of the probe on the undamaged material ($f_0 = 3.99 \pm 0.01$ MHz) is lower than that measured using the Impedance analyser ($f_0 = 4.12 \pm 0.01$ MHz) in section 5.4.3 (see table 6.2). This is most likely due to additional series inductance or parallel capacitance within the electronics of the Howland current source prior to the voltage measurement shifting the electrical resonance down.

The raw data signals, $S$, shown in component form in figure 6.6, are put through a 2 step process of:

1. **Smoothing** in the frequency domain, to eliminate the effects of intrinsic noise between sequential frequency bins in the signals, and

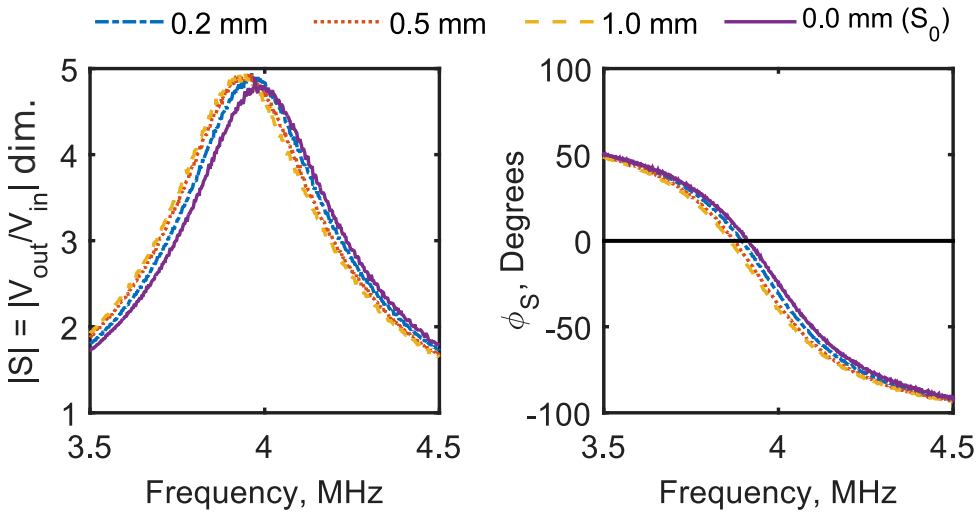


Figure 6.6: Raw frequency spectrum data for varying depth slots on Titanium 6-4 measured using a frequency sweep approach. Data is displayed between 3.5-4.5 MHz in order to clearly show the separation between different defect spectra. The data is displayed as Magnitude $|S|$ (left) and Phase $\phi_S$ (right) clearly showing electrical resonance at approximately 4.0 MHz.

2. **Background subtraction** of a smoothed background frequency spectrum, $S_0$, to produce a measure of the change in discontinuity signal.

The resultant changes in signal from each discontinuity were replotted as a function of frequency to show where the greatest changes in measured signal occur in the spectrum (Figure 6.7). This process is analogous to balancing a probe on a section of undamaged material.

The results in figure 6.7 show the deviation in magnitude and phase from the undamaged signal spectrum for measurements above each discontinuity. For the magnitude there is a positive pre-resonance signal peak and a negative post-resonance signal peak in frequency space. The cross-over frequency in the magnitude represents the point where the signal profiles of defect measurements cross the undamaged material signal spectrum. Conversely the phase difference between discontinuity measurements and the undamaged material exhibits a single negative peak at approximately the electrical resonance of the probe on undamaged material.

Table 6.2: Key properties of experimental raw frequency spectrum data from the frequency sweep measurement of the Ti6-4 calibration slots.

| Discontinuity | $f_0$ ($\pm$0.02 MHz) | *Peak* $\lvert S\rvert$ ($\pm$0.05 *dim.*) |
|---|---|---|
| 0.0 mm | 3.99 | 4.78 |
| 0.2 mm | 3.97 | 4.89 |
| 0.5 mm | 3.94 | 4.91 |
| 1.0 mm | 3.93 | 4.89 |

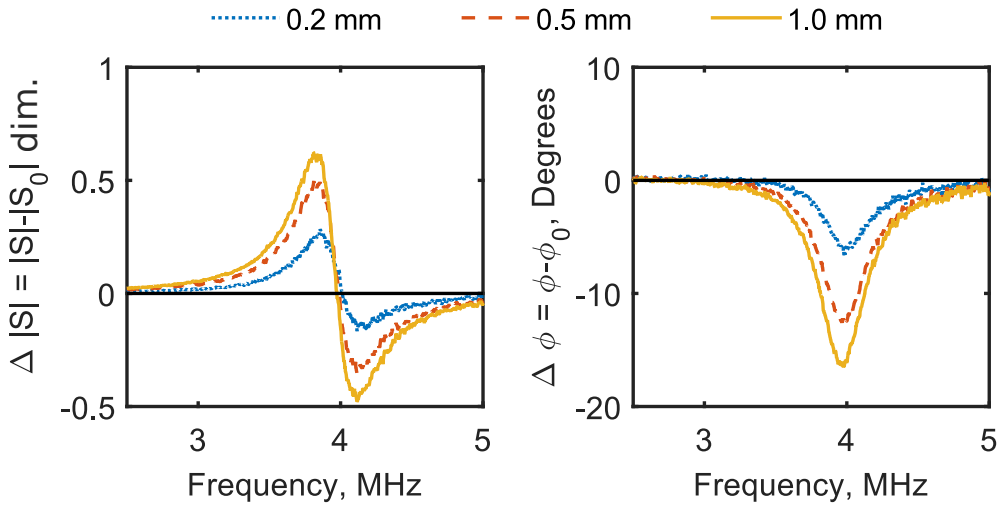


Figure 6.7: Background subtracted defect signal frequency spectra for 0.2, 0.5 & 1.0 mm deep slots as a function of frequency, showing changes in Magnitude $\Delta|S|$ (left) and Phase $\Delta\phi_S$ (right).

This is due to the phase at electrical resonance having the greatest rate of change with frequency i.e. greatest gradient, therefore slight shifting in resonance cause the greatest difference in phase at these frequencies.

As observed using the impedance analyser in section 5.4.3, figure 6.7 identifies a frequency range, close to resonance, where the magnitude of the defect signal reaches a maximum. The next step was to determine how the background noise around resonance changes so as to generate a signal-to-noise spectrum.

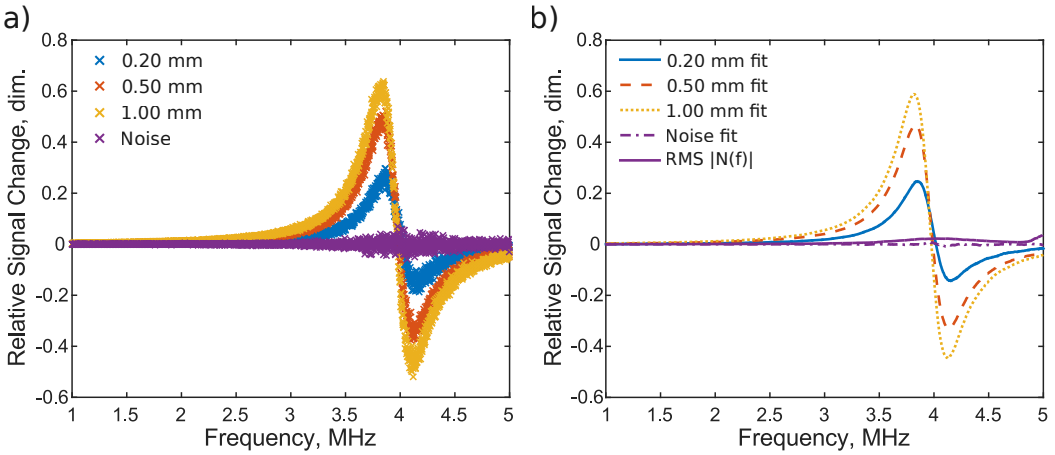


Figure 6.8: Background subtracted discontinuity magnitude signals relative to background signal. Showing smoothed trend curves for each discontinuity as well as the running RMS average of the background noise signal.

### Background Noise

A background noise frequency spectrum, $S_n(f)$ was taken at an arbitrary location within an area of undamaged material from the c-scan data. The $S_0(f)$ background signal was subtracted from $S_n(f)$ to give an example of the noise level in the inspection, $N(f)$. A running root-mean-square (rms) average (frequency bin depth of 20) was made of the absolute magnitude of the balanced noise level, $rms(|N(f)|)$, and used as the background noise level for the inspection. This averaged out any strong peaks or dips at individual frequencies in the spectrum sweep and gave a smoother, more continuous, trend in the background noise level with frequency, $|N(f)|_{rms}$. Figure 6.8 shows the background-subtracted signal magnitude spectra of all three discontinuities, background noise, each signals trend and the rms background noise magnitude.

Note that the rms background noise reaches a peak at a different frequency from the discontinuity signals. The spread of electrical signal noise is most likely a result of the background noise produced by the XY scanning table and other electronic systems within the vicinity of the experimental setup. The signals were fitted

with spline best fit curves (smoothing coefficient of 0.99) to display the frequency trends of the signals with changing discontinuity depth (figure 6.8).

### Defect Signal Analysis

The two main changes observed in the background subtracted chirp frequency spectrum are the peak signal strength and the frequency shift they produce. These changes can be measured using a number of methods: the amplitude of the signals can be measured by finding the peak amplitude of the chirp frequency spectrum, $S_{max}$, or by calculating the area under the chirp curve, $A$, (see figure 6.9). The frequency shift produced by different discontinuities can be measured by finding the frequency of peak amplitude, $f_{max}$, or the zero crossing point, $f_X$, of the chirp spectrum. Figure 6.9 graphically demonstrates these measurement methods for the three varying depth discontinuities in Ti6-4.

The relationship between peak amplitude, $S_{max}$, and the area under the chirp spectrum curve, $A$, is linear over the range of discontinuities inspected. This implies that they both provide the same information about the discontinuity. The shifting behaviour of peak signal frequency, $f_{max}$, and the zero-crossing point, $f_X$, are not proportional to one another. The analysis of these parameters will be used later to investigate the behaviour of the resonance chirp measurement to varying defect geometry.

### Signal-to-Noise Ratio

The signal-to-noise ratio (SNR) of the discontinuity measurements were calculated by dividing the signal spectra by the rms noise, $N_{rms}$, it is easy to see within what range of frequencies this phenomenon produces a sensitivity improvement in the measurement (Figure 6.10).

Figure 6.10 again shows that there is band of frequencies close to electrical resonance where the sensitivity of an ECT measurement is enhanced via variations

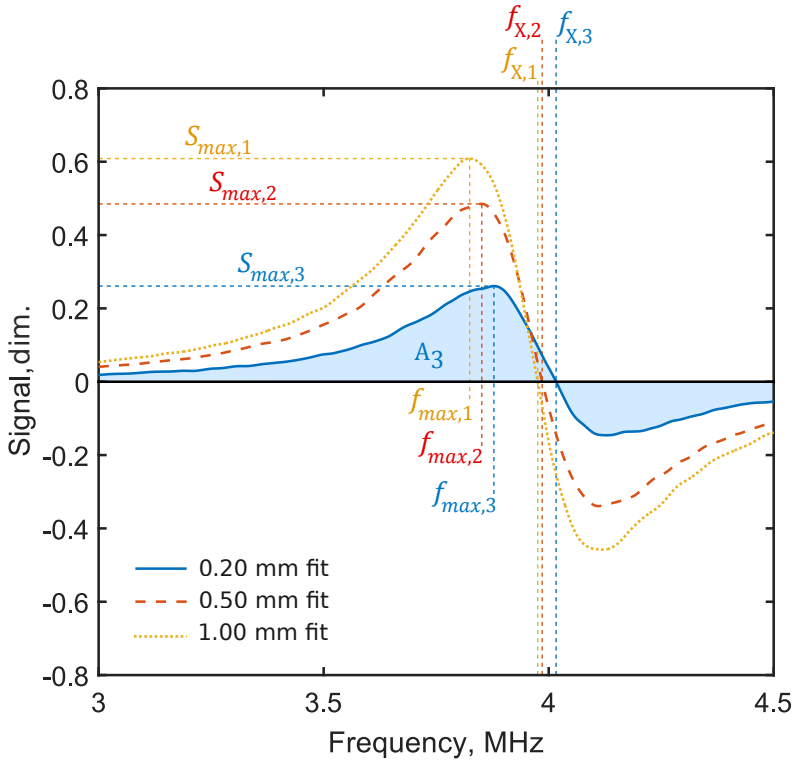


Figure 6.9: Background subtracted chirp frequency spectrum of 3 large discontinuities in Ti6-4 of increasing depth, showing the measurable features of the chirp signals.

in the resonant frequency of probe. As was discussed in section 5.4.3, the shifting of the resonant frequency of the probe comes about due to changes in the mutual induction between probe and material surface in the presence of discontinuities.

The SNR peaks occur in a region conventionally avoided by probe manufacturers and operators, owing to the unpredictable and unstable nature of the electrical peak resonance. Conventional probe operating frequencies finish significantly short of the electrical resonance of the probe, keeping safely within a range where the sensitivity scales linearly with frequency due to the inductive reactance component of impedance ($\omega L$).

Beyond resonance, the reactive component of the system is dominated by capacitive changes within the cable, such that successful measurements of the inductive changes are difficult so this region is avoided. Between the conventional limit and

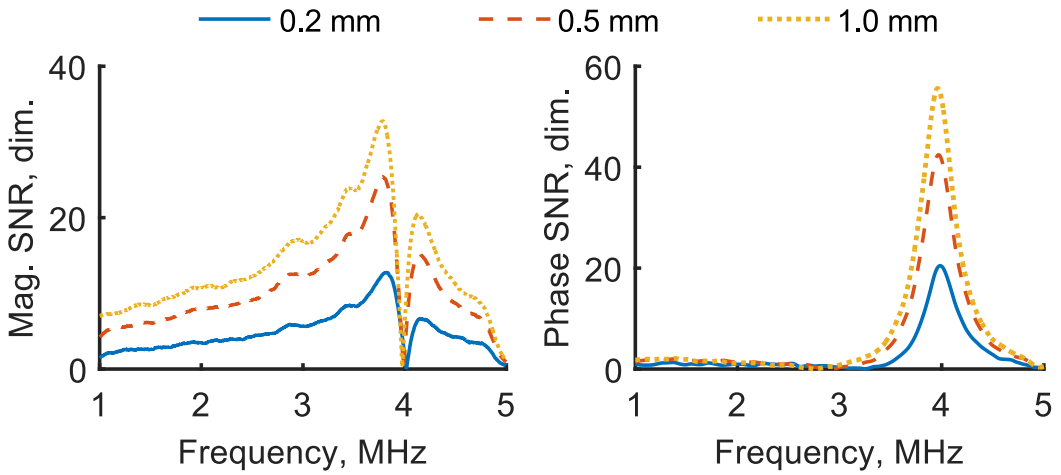


Figure 6.10: Signal-to-Noise Ratio's of 3 large discontinuities in Ti 6-4. Experimental plots showing the SNR trends as a function of frequency for each material discontinuity in both magnitude (left) and phase (right).

the electrical resonance of the system lies a region of probe sensitivity dominated by the effects of defect-decoupling resonance-shifts, where significant SNR enhancement occurs. The bandwidth region will be dependent on the probe inductance, cable length, test material and defect size.

Table 6.3: SNR peak details in experimental data for three discontinuities of increasing depth with reference to SNR at 1MHz.

| Defect Depth (mm) | SNR @ $1MHz$ ($\pm$0.1) | SNR peak freq. $f_{NERSE}$ ($\pm$0.01 MHz) | SNR @ $f_{NERSE}$ ($\pm$0.1) | Factor increase from 1 MHz |
|---|---|---|---|---|
| 0.20 | 1.5 | 3.81 | 12.7 | 8.5× |
| 0.50 | 4.3 | 3.78 | 25.4 | 5.9× |
| 1.00 | 7.1 | 3.78 | 32.8 | 4.6× |

Table 6.3 shows that the sensitivity of the system significantly improves within this sensitivity enhancing band of frequencies, hereafter referred to as the near electrical resonance signal enhancement (NERSE) frequencies. As well as the amplitude of the NERSE peak changing with the dimensions of the discontinuity, the peak sensitivity frequency, $f_{NERSE}$, of a measurement also shifts in relation

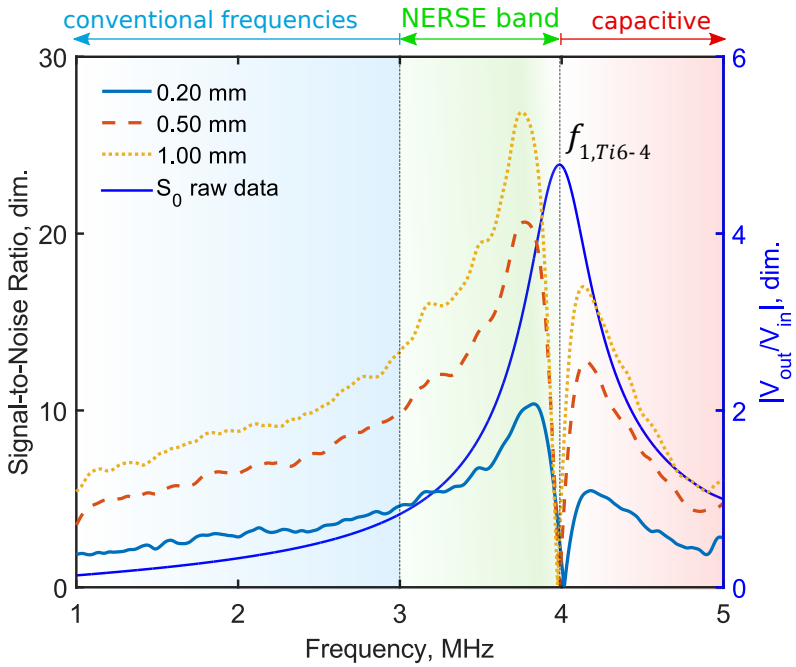


Figure 6.11: Near Electrical Resonance Signal Enhancement (NERSE) signal-to-noise ratio (SNR) plot of signal magnitude for three discontinuities of varying depth in relation to electrical resonance on Ti6-4, after [165].

to the dimensions of the discontinuities. Table 6.3 indicates that the enhancement effect, relative to the measurement at 1 MHz, improves for shallower discontinuities. These effects were investigated further by measuring the frequency sweep change for defects of controlled dimensions.

### 6.3.4 Defect Geometry Study

Chirp inspections were performed, from 1-5 MHz, for a range of machined defects in a Ti6-4 sample in order to investigate the relationship between notch dimensions (see figure 6.12) and the properties of the chirp frequency spectrum. The dimensions of the machined defects inspected are given in table 6.4.

The machined (simulated) discontinuities in table 6.4 are broken up into two groups:

1. Group A. Infinitely long simulated defects i.e. defects with surface length much

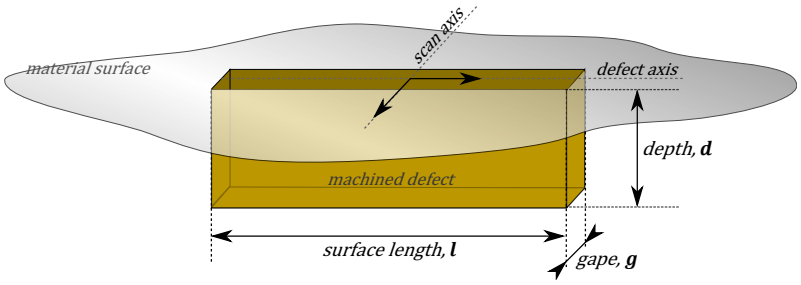


Figure 6.12: Diagram of machined defect dimension geometry.

greater than the probe outer diameter, $d_{out}$, (i.e. $l \ll d_{out}$), and had their chirp signals evaluated in relation to the cross-sectional area of the discontinuity along the scan-axis (Figure 6.12).

2. Group B. Finite length simulated defects i.e. defects with surface length comparable to or less than the probe outer diameter ($l \approx d_{out}$). These had their chirp signals evaluated in relation to the cross-sectional area of the discontinuity along the defect-axis, perpendicular to the scan-axis.

The simulated defect cross-sectional areas for Groups A & B are proportional to the increase in path length experienced by eddy-currents when they encounter such discontinuities, and are therefore forced to flow under or around the obstructions respectively.

The machined defects can be separated into additional sub-groups defined by which dimensions are constant across a number of defects, and which dimensions vary. These sub-groups were then used to study the behaviour of chirp inspection measurements as a function of different defect dimension changes i.e. changes in depth ($d$), gape ($g$), length ($l$) and size ($s$) whilst maintaining a constant aspect ratio of 2:1 (length:depth). As a result, 4 separate studies were performed investigating the effect of changes in machined discontinuity dimensions, on the NERSE chirp measurement.

Table 6.4: Machined defect dimensions.

| Group | Defect No. | Length ($\pm 0.03\ mm$) | Depth ($\pm 0.03\ mm$) | Gape ($\pm 0.03\ mm$) |
|---|---|---|---|---|
| A.d | 1 | - | 0.20 | 0.50 |
| A.d | 2 | - | 0.50 | 0.50 |
| A.d | 3 | - | 1.00 | 0.50 |
| A.g | 4 | - | 0.50 | 0.10 |
| A.g | 5 | - | 0.50 | 0.20 |
| A.g | 6 | - | 0.50 | 0.50 |
| A.g | 7 | - | 0.50 | 1.00 |
| B.l | 8 | 0.50 | 0.50 | 0.10 |
| B.l | 9 | 1.00 | 0.50 | 0.10 |
| B.l | 10 | 1.50 | 0.50 | 0.10 |
| B.l | 11 | 2.50 | 0.50 | 0.10 |
| B.s | 12 | 0.25 | 0.13 | 0.10 |
| B.s | 13 | 0.50 | 0.25 | 0.10 |
| B.s | 14 | 0.75 | 0.38 | 0.10 |
| B.s | 15 | 1.00 | 0.50 | 0.10 |

### 6.3.5 Results & Discussion

For each defect in table 6.4, a 1-5MHz chirp inspection was carried out and the maximum signal response from the defect was evaluated by measuring it's critical features; peak amplitude ($S_{max}$), peak frequency ($f_{max}$), area under curve ($A$) and frequency of zero-crossing ($f_X$) as defined in section 6.3.3. The results of the critical feature analysis are summarised in the following sections.

#### Amplitude Changes

The relationship between peak amplitude, $S_{max}$, and area under the curve, $A$, was examined for group A and B defect geometries in table 6.4. The results are separated into their sub-groups to show the behaviour of the chirp measurement as a function of varying different discontinuity dimensions (Figure 6.13).

For each subgroup a polynomial, best fit curve was plotted of the form,

$$y = p_1 x^2 + p_2 x + p_3, \tag{6.6}$$

where $y$ is the area axis and $x$ is the peak amplitude axis. $p_3$ was forced to zero so that the curves intersected the origin i.e. when the peak amplitude is zero, the area under the curve will also be zero.

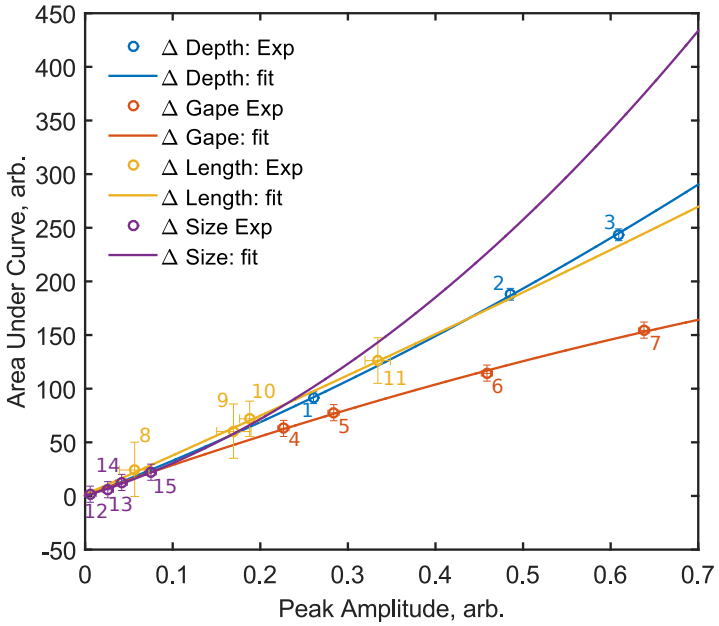


Figure 6.13: Peak amplitude, $S_{max}$, verses area under the background-subtracted frequency-sweep curve, $A$, for large machined defects ($l \gg d_{out}$) of varying dimensions and defects of finite length ($l \approx d_{out}$). Four plots show experimental data points and polynomial best fit curves for the chirp response parameters as a function of varying depth (blue), varying gape (red), varying length (yellow) and varying size (purple). The numbers of the defects (as defined in table 6.4) are indicated next to each data point.

The area under the chirp curve, $A$, is shown in figure 6.14 as a function of the changes in defect area. The results are separated into two subplots of groups A (figure 6.14.a) and B (figure 6.14.b) and displayed as a function of the variable cross-sectional area for that group of defects. Group A is represented by the

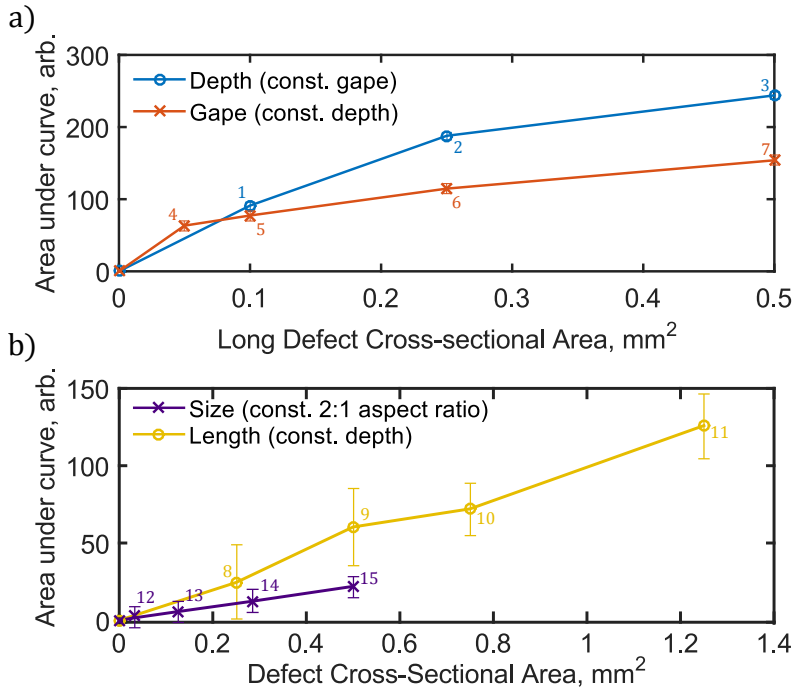


Figure 6.14: Area under the background-subtracted frequency-sweep curve (frequency summation) for machined defects of varying dimensions given in table 6.4. a) Infinitely long defects of constant surface length ($l \gg d_{out}$): comparing defects of varying depth and varying gape, and b) finite length defects of constant gape (0.10 $mm$): comparing defects of varying length and varying overall size. The numbers of the defects (as defined in table 6.4) are indicated next to each data point and the associated measurement error-bars shown.

cross-sectional area along the scan axis (see figure 6.12), and group B defects are represented by their cross-sectional area along the defect axis.

The results in figure 6.13 indicate that there is a distinct difference in how varying gape changes the relationship between $S_{max}$ and $A$ when compared to depth or length. At small dimensions the amplitude trends become indistinguishable from one another so one would expect not to be able to differentiate between different defect dimension changes for defects smaller than the size of the probe coil. However, the measurements of the group A defects (figures 6.13 & 6.14), imply that amplitude changes can be used as a relative measure of changes in depth and gape. In figure 6.13 it appears that the changing gape of a discontinuity, with a fixed depth,

tends towards a plateau of the area under the curve, whilst the peak amplitude continues to increase for higher gapes. In contrast, the changing depth of a discontinuity leads to the inverse effect; plateauing peak amplitude whilst the area under the curve increases for increasing depths. These changes are a result of changes to the full frequency spectrum of the chirp measurement depending on the depth and gape. Lower frequencies penetrate deeper into the material and so an increase in defect depth would be expected to cause a change to ever lower frequencies in the spectrum thereby increasing the area under the chirp curve. Conversely, changes in gape for a fixed depth would not affect the lower frequencies of the spectrum and would only cause changes at higher frequencies i.e. the NERSE peak frequency.

**Frequency Changes**

The relationship between peak frequency, $f_{max}$, and peak amplitude, $S_{max}$, was examined for group A and B defect geometries in table 6.4. The results are separated into their sub-groups to show the behaviour of the chirp measurement as a function of varying different discontinuity dimensions (figure 6.15). No best fit functions were applied to the data.

No error bars are shown in the figure due to the difficulty in determining errors in the frequency measurement which was largely subjective. Larger discontinuities have sharper peaks and clear zero-crossing points, whereas smaller defects are more susceptible to background noise which led to less reliable signal analysis.

The results shown in figure 6.15 show the trajectories of the NERSE peaks signal in frequency-amplitude space. The scattered frequency positions of the different defect group studies is a result of differences in the probe setup as discussed below.

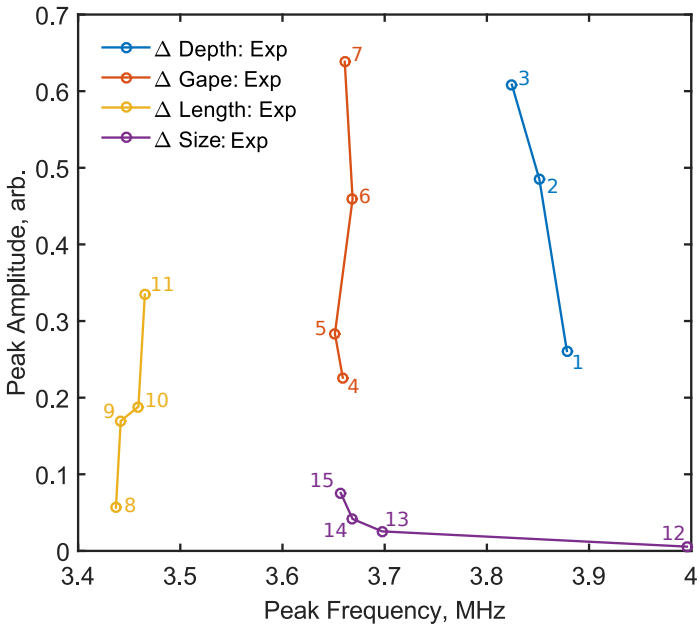


Figure 6.15: Experimental measurement of peak frequency verses peak amplitude of chirp measurements for the four groups of machined defects (defined in table 6.4). The numbers of each defect (as defined in table 6.4) are indicated next to each data point.

### 6.3.6 Abnormalities, Errors & Uncertainty

Although the same coil and coaxial cable length were used for all the inspections, the studies were performed at different points during the project. As a result the coaxial cable may have been damaged or the length varied slightly between defect studies. In addition to this, the protective Teflon tape layer applied to the probe tip may have varied in quality each time it was replaced thereby leading to variations in the lift-off from the surface of the material. Each of these possibilities would have led to differences in the resonant peak position. As a result, no discernible trends in the trajectories of the chirp peaks can be reliably commented upon.

It is likely that there will be no simple trend in peak trajectory with defect geometries, and that the changes will be highly dependent on the coil geometry relative to the defect sizes. The sample set for the data documented here is too

small, and over a limited range of sizes, to draw any definitive conclusions about the effect of defect dimensions on NERSE chirp measurements. Future work should focus on the development of forward and inverse models of the resonance behaviour of ECT probes to assist in determining the expected trends in experimental results.

The measurements made of simulated defects of varying length (defect group B.l) have significantly larger error margins for the measured values. This is a result of damage to the probe head prior to inspection which went unnoticed. The damage to the probe head led to significantly increased background noise levels and as such made the analysis of the chirp signal responses more susceptible to error. For future inspections a replacement probe was produced.

As the size of the simulated defects get smaller, and tend towards dimensions less than the critical dimensions of the excitation coil, the background amplitude of electrical noise in the signals begins to become comparable to the changes due to the discontinuity. This makes the fitting process less reliable for determining the features of the chirp response. This will be even more significant a problem when one comes to inspect for real defects and therefore disqualifies critical parameter analysis of chirp measurements for sub-millimetre defects as a viable inspection technique in its current form. Future work for improving this would require smaller coils in order to get over this limitation.

## 6.4 Harmonic NERSE Excitation

The behaviour of electrical resonance in the presence of a discontinuity was shown to result in a signal enhancement phenomenon in a band of frequencies approaching electrical resonance, referred to as the NERSE band. The sensitivity of conventional inspections is limited for defects smaller than the size of the detection coil, often leading to these signals not being measured above background noise. The effectiveness of chirp excitation measurements for the detection of sub-mm defects in Ti6-4 is

limited by high levels of incoherent background noise. This is due to each frequency in a sweep effectively being measured in a single shot. However, incoherent noise can be eliminated by averaging over a large number of single cycles. An investigation was performed to investigate how operating at a single frequency, in the NERSE frequency band improves the inspection sensitivity of a probe. This was performed by carrying out a series of probability of detection (see appendix A) studies on real fatigue cracks in Ti6-4 samples, operating the probe at a conventional operation frequency, and within the NERSE frequency band.

### 6.4.1 Experimental Setup

Using the same experimental setup as shown in section 6.2.1, individual excitation frequencies were used to operate the ECT probe and the signals averaged over 1000 cycles in each case. For every inspection the gain of the measured signal was set so that the $V_{out}$ signal filled 80% of the dynamic measurement range when it was on undamaged material, thus providing sufficient measurement resolution. The time domain $V_{in}$ and $V_{out}$ waveforms were recorded, converted into the frequency domain via Fourier transform and $V_{out}$ normalised to $V_{in}$. The signal at the specific frequency of excitation within the frequency spectrum was then extracted to give a averaged single frequency measurement at each location in the C-scan.

#### Inspection Probe

Due to mishandling, the probe used in the studies detailed in the previous chapters, was damaged and so a replacement probe (probe 2a) was produced in-house (see figure 6.16). The critical details of the replacement probe are documented below.

A calibration chirp scan was carried out using the new probe on the Ti6-4 calibration block used in previous chapters to determine where the NERSE band of frequencies were for the new probe. Probe 2a was operated using a 1.5 m long RG174, 50 Ohm coaxial cable to replicate the same capacitance as for the original

Table 6.5: Physical and electrical properties of eddy-current probe used to carry out probability of detection (PoD) study on NERSE single frequency excitation.

| **Physical Properties** | **Value** | **Units** |
|---|---|---|
| Number of turns, $n$ | 35 | |
| Number of layers, $N$ | 4 | |
| Wire diameter, $t$ | 0.10 | $mm$ |
| Core material | Ferrite 61* | |
| Core relative permeability, $\mu_r$ | 35 | |
| Core diameter, $d_{in}$ | $0.69 \pm 0.01$ | $mm$ |
| Coil outer diameter, $d_{out}$ | $1.14 \pm 0.05$ | $mm$ |
| Coil height, $h$ | $0.71 \pm 0.01$ | $mm$ |
| Inherent lift-off, $l_0$ | $0.34 \pm 0.01$ | $mm$ |
| Cable length, $h$ | $1.50 \pm 0.01m$ | $m$ |
| **Electrical Properties** | | |
| Coil inductance, $L_L$ | $8.77 \pm 0.09$ | $\mu H$ |
| Cable capacitance, $C_c$ | $158.4 \pm 0.5$ | $pF$ |
| Resonant frequency (air), $f_0$ | $4.27 \pm 0.01$ | $MHz$ |

*From Fair-Rite Products Corp., Wallkill, NY, USA

probe (probe 1). The chirp excitation procedure detailed in section 6.2.1 was used to perform the calibration sweep measurement. The frequency spectrum of probe 2a is shown in Figure 6.17.

The lower inductance of probe 2 coil results in a higher resonant frequency. This means that the probe must be operated at a higher frequency in order to take advantage of the NERSE phenomenon. By comparing the SNR frequency spectrum in figure 6.17 to the equivalent spectrum for the original probe, figure 6.11, it was calculated that the sensitivity of probe (probe 2.a) at the NERSE peak is approximately 60% of the original probe (probe 1).

### 6.4.2 Experimental Procedure

The probe setup detailed above was used to statistically analyse the sensitivity of the NERSE excitation ECT approach. Using the single frequency excitation setup detailed in section 6.4.1 a collection of 38 Ti6-4 fatigue test samples (see appendix A)

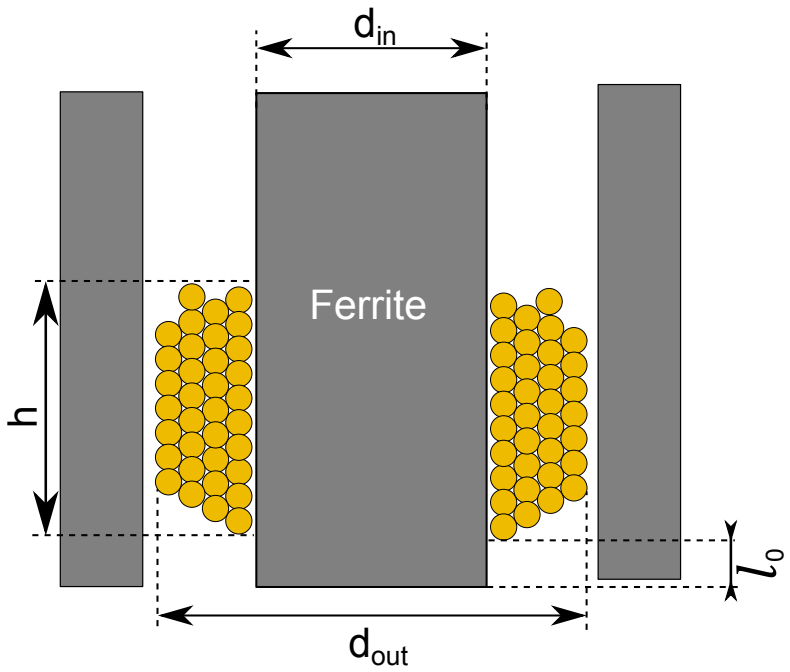


Figure 6.16: Schematic diagram of probe 2a.

were scanned to produce a distribution of ECT signals over a range of defect sizes. Probability of detection (PoD) analysis was performed on each data set to achieve a direct comparison between standard ECT excitation and NERSE frequency measurements.

From the SNR spectrum in figure 6.17, two frequencies were selected at which to perform the PoD study. One inspection would be performed at a frequency representing the best conventional ECT excitation frequency, and another PoD inspection would be carried out operating the probe at its peak NERSE frequency, $f_{NERSE}$.

A control PoD study was also made to determine whether the sensitivity improvement is merely a result of increasing the frequency of excitation and not a result of the resonance shifting. The same excitation coil from probe 2a was operated using a shorter coaxial cable length of 0.25 m ($C = 26.4 \pm 0.5\ pF$). This reduces the capacitance of the system such that the electrical resonance was at a

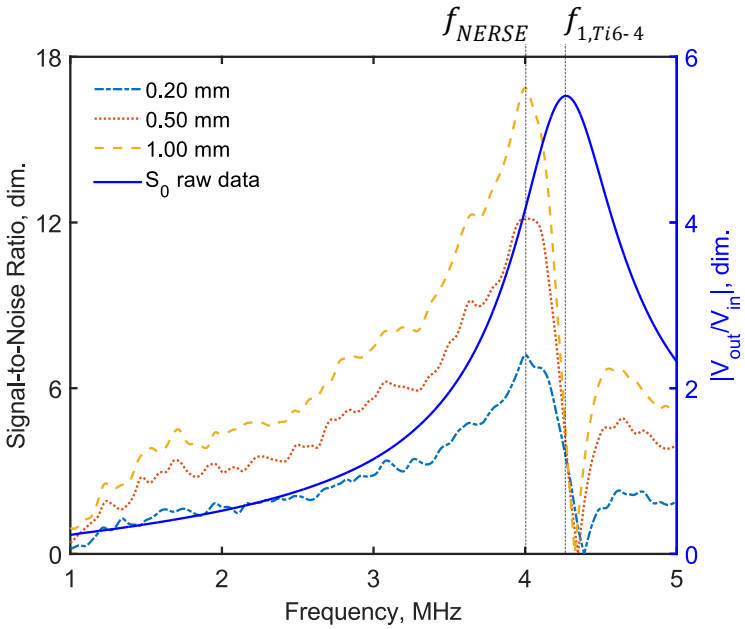


Figure 6.17: Chirp excitation signal-to-noise 1-5MHz frequency spectrum measurement of three calibration slots in Ti6-4 showing the electrical resonance of probe 2 on undamaged material, $f_{1,Ti6-4}$, and the peak NERSE frequency, $f_{NERSE}$.

significantly higher frequency. The probe, referred to from here on as probe 2b, was then used to perform another PoD study operating at the NERSE frequency of probe 2a. Because of the higher resonant frequency this would be equivalent to operating within the conventional frequency range. The results of the studies are directly compared.

A standard excitation frequency of 3.25 MHz was selected to represent the best conventional ECT excitation frequency, i.e. to represent the most sensitive industrial ECT inspections performed on Ti6-4 components. A frequency of 4.0 MHz was selected for the NERSE excitation measurement to coincide with the peak NERSE frequency as shown in figure 6.17. These operation frequencies are higher than those that would have been used for probe 1 due to probe 2a's lower inductance and thus higher resonant frequency. A frequency of 4.0 MHz also used in the control measurement using probe 2b.

A chirp measurement for each of the probe configurations (probes 2a and

2b) on a section of undamaged Ti6-4 are compared in figure 6.18 to demonstrate the difference in measurement frequencies relative to the electrical resonance of probe 2.a.

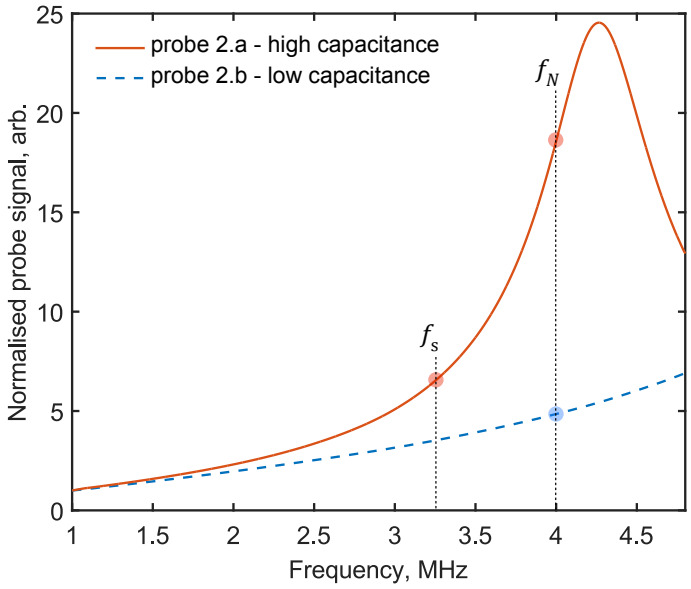


Figure 6.18: Comparison of background frequency sweep signals of probe 2 connected with two different co-axial cable lengths (probe 2a and probe 2b) identifying the frequency of operation for the PoD studies.

Each PoD specimen was scanned with a resolution of 0.25 $mm$ in both the X and Y scan axis to replicate industrial inspections. The capture depth of the measured signal was altered for the two different excitation frequencies so that 1000 cycles of the input frequency signal were captured allowing a direct comparison between inspections (see table 6.6).

Table 6.6: Time for 1000 cycles of excitation frequencies and capture depth of measurements.

| **Frequency, MHz** | $\Delta t_{1000}$ $ms$ | **Capture Depth, Samples** |
|---|---|---|
| 3.25 | 0.33 | 15385 |
| 4.00 | 0.25 | 12500 |

The time domain signals were Fourier transformed into the frequency domain

and the ratio of $V_{out}(f)/V_{in}(f)$ calculated for the harmonic excitation frequency used for each point in the scan. The resulting C-scan data was then analysed to measure the defect signals.

### 6.4.3 Data Analysis Method - Maximised Real Component

For the purposes of this study a phase sensitive peak amplitude type measurement (see section 2.4) was used to record the defect signals. In order to carry out the measurement on the C-scan data a series of signal analysis steps were performed on each scan. With reference to figure 6.19, the raw complex C-scan data, $\tilde{A}$, of size $m \times n$, was analysed using the following procedure.

1. **Balancing/Zeroing (background subtraction)** - The average complex background signal, $\tilde{N}_0$, is calculated from an arbitrary area of the C-scan over undamaged material (figure 6.19.a). This value is then subtracted from every position in the C-scan to zero the scan data (figure 6.19.b) as expressed by,

$$\tilde{B}_{mn} = \tilde{A}_{mn} - \tilde{N}_0. \tag{6.7}$$

2. **Complex Rotation** - The peak defect signal was located (white cross-hairs, figure 6.19.b) and the complex value from that point, $\tilde{B_{max}}$, used in conjugate form to rotate all data-points in complex space via the equation,

$$\tilde{C}_{mn} = \frac{1}{|\tilde{B}_{max}|}\tilde{B}_{mn}\tilde{B}^*_{max}. \tag{6.8}$$

   The denominator in equation 6.8 ensures the overall magnitude of the complex data does not change. This process forces the peak defect signal to have zero phase i.e. entirely real (figure 6.19.c).

3. **Median filtering** - The real and imaginary components of the C-scan data are filtered using an inbuilt Matlab (MathWorks, Natick, Massachusetts, USA)

median filter of pixel size 15 × 15 to smooth out any low spatial-frequency background variations from the image (figure 6.19.d).

4. **Defect Measurement** - The maximum defect signal is selected within the real component C-scan image. The complex data for the pixels within a fixed cursor range (green cursor figure 6.19.e) is displayed in a Lissajous (complex plane) plot in figure 6.19.f. The maximum real component amplitude for the defect signal is recorded.

5. **Background Noise Measurement** - The real component amplitude on a signal from an arbitrary part of the undamaged material is measured and recorded, as above. One could use a background root mean squared average to calculate the background but this technique does not represent the maximum observable background signals. The arbitrary maximum approach used in this study is more representative of the potential for false calls within an inspection.

The result of these processes is a phase sensitive measurement of defect signal and background noise.

### Decision Threshold, $a_{thresh}$

Accurately defining the threshold level for a PoD analysis study is the most influential part of the analysis. If the decision threshold, $a_{thresh}$, is underestimated then the PoD analysis will calculate a much higher probe sensitivity. Overestimate $a_{thresh}$ and the inspection will be calculated to be less sensitive than is achievable. The $a_{thresh}$ level is typically set as 2 or 3 times the maximum background signal observed during a PoD study. This is to minimise the number of false calls. Two different approaches were used to set $a_{thresh}$ and compared against one another.

The first approach took the maximum background noise signal, $N_{max}$, from all of the different PoD sample inspections for a given inspection (i.e. 4.0 MHz NERSE, 4.0 MHz Control or 3.25 MHz Standard), and used that value to set $a_{thresh}$

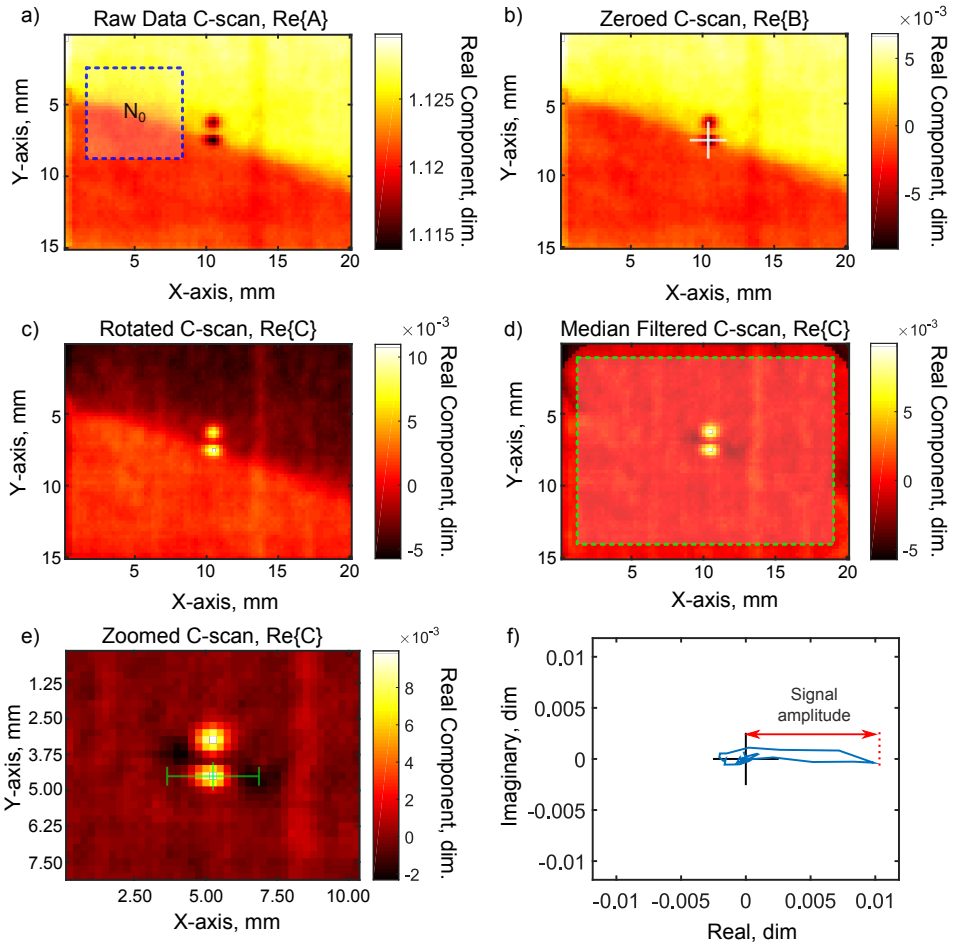


Figure 6.19: Harmonic excitation data analysis process showing a C-scan of the real component at each stage.: a) Raw C-scan data showing arbitrary area of background material used to zero the image. b) Zeroed C-scan showing cross-hairs over the maximum defect signal pixel. The pixels complex value is used to rotate the complex C-scan data. c) Rotated C-scan. d) $15 \times 15$ pixel median filtered C-scan. e) Zoomed in C-scan image showing measurement cursors over the peak defect signal and an arbitrary background point. And f) Lissajous (complex plane) plot showing the real vs imaginary components of the final C-scan data as measured along the x-axis of the green cursors in e) to give defect and noise indications.

as $3N_{max}$. The second approach calculated the root mean squared (rms) average, $N_{rms}$, of all the noise signals from all of the PoD sample measurements in a given measurement type, and used that to set $a_{thresh}$ to $3N_{rms}$.

### 6.4.4 Results & Discussion

Three independent inspections were performed on 38 Ti6-4 fatigue crack samples and the maximum defect signal was recorded along with a measure of the background noise for every scan. For each PoD sample a maximum defect response and a maximum background noise value were recorded.

#### Probability Curves

The eddy-current signal responses of the three PoD inspection studies are shown in figure 6.20 (See Appendix A for a full description of the PoD analysis formula). PoD analysis was performed on the results of all three inspections using, and for both decision threshold setting approaches stated in section 6.4.3. The computation was performed using the statistical analysis software, R, implementing an industrially used software package, MIL-HDBK-1823, in accordance with RPS 906 [154]. The analysis plots defect length verses probability of detection, along with 95% confidence bounds, which can be used to calculate the smallest statistically detectable defect length, following Annis [154] (see Appendix A). This value is known as $a_{90/95}$ and the calculated results for the analysis are summarised in table 6.7. The PoD curve for the NERSE excitation inspection with $a_{thresh} = 3N_{max}$ is shown in figure 6.21. Similar plots were obtained for the other two inspections but were omitted for the sake of concision.

The results displayed in figure 6.21 and table 6.7 are a representative measure of the statistical sensitivity improvement that is achievable through operating ECT probes at frequencies within the NERSE band.

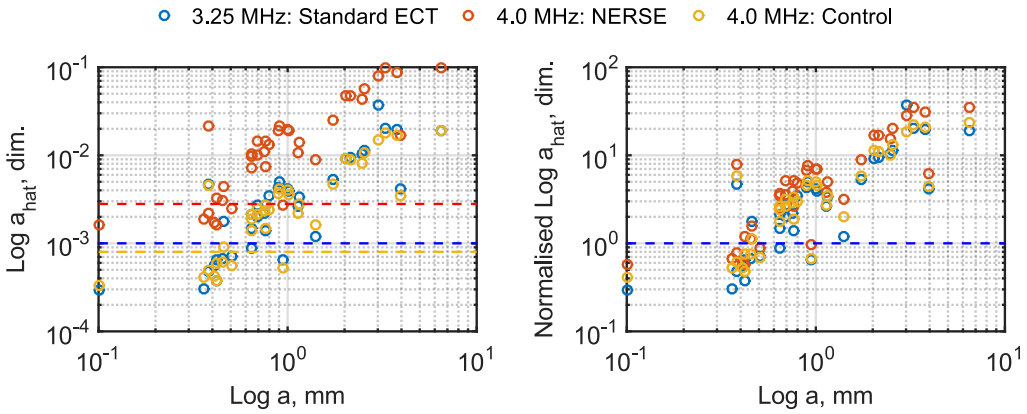


Figure 6.20: Log-log plot of crack size verses signal response: (left) ECT crack signals, $\hat{a}$, for the 3 measurement setups along with their associated decision thresholds ($3N_{max}$), and (right) $\hat{a}$ normalised to the decision threshold to show direct comparison between all 3 measurement techniques.

Table 6.7: Probability of detection (PoD) study results showing the $a_{90/95}$ for the three measurement methods.

| | | $a_{90/95}$ $(mm)$ | |
|---|---|---|---|
| **Operation Setup** | Frequency, MHz | $3N_{max}$ | $3N_{rms}$ |
| **Setup 2a - Standard** | 3.5 $MHz$ | 1.09 | 0.67 |
| **Setup 2a - NERSE** | 4.0 $MHz$ | 0.82 | 0.56 |
| **Setup 2b - Control** | 4.0 $MHz$ | 0.94 | 0.64 |

### Background Noise Analysis

Analysis was performed on the measured background noise using three different measurement approaches. The three measurement methods were performed for each PoD sample C-scan, on an arbitrary area of undamaged material, e.g. $B$ (Figure 6.22). The methods were:

1. RMS Magnitude, $N_1 = |B|_{rms}$ - Calculate the RMS average noise of all the absolute magnitudes of the background area data (phase insensitive averaged peak measurement). This gives the rms average background signal regardless of it's orientation in phase space.

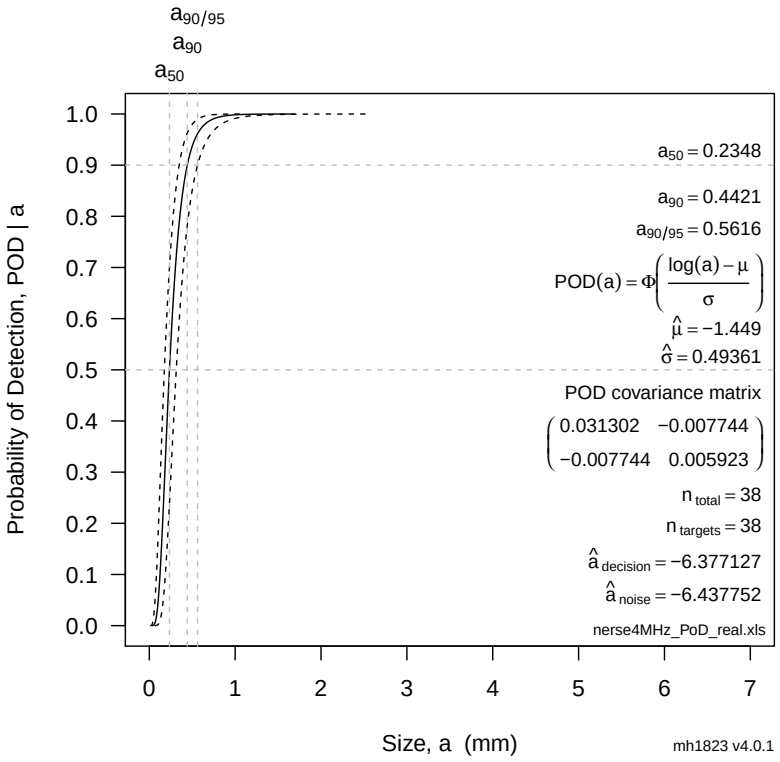


Figure 6.21: Probability of detection curve for probe setup 2a operated at a frequency of 4.0 MHz (within the NERSE operating range for that setup).

2. RMS Real Component, $N_2 = \Re\{B\}_{rms}$ - Calculate the RMS average noise of all the real components of the background area data (phase sensitive averaged peak measurement). This gives the rms average background noise signal observed in the same orientation as the defect signal.

3. Maximum Real Component, $N_3 = \Re\{B\}_{max}$ - Measure the maximum real component noise from the background area (phase sensitive peak measurement). This gives the maximum background value observed in the same orientation as the defect signal.

The last method represents the method used in the PoD analysis to give the results shown in figures 6.21 and table 6.7. Each of the three measurements listed above was performed on each PoD specimen. The noise data-sets were analysed

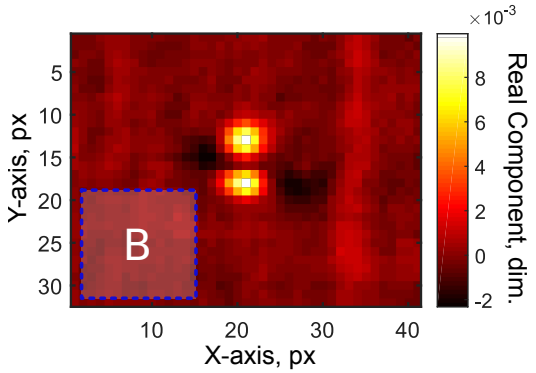


Figure 6.22: Example arbitrary area of background material, $B$, used for background noise level measurements.

to determine the percentage standard deviation of the methods for each inspection approach and noise measurement. The results are shown in figure 6.23.

Figure 6.23 shows that the maximum real component analysis, $\Re\{B\}_{max}$, has the maximum percentage variation compared to the other two methods. This demonstrates the inherent issues with using background noise measurements to set the decision threshold, $a_{thresh}$.

The $\Re\{B\}_{rms}$ provides the most stable measure of the three background signal measurements as expected given the averaging nature of the technique. However, this technique would not give as representative indication of maximum noise levels as the other methods. The results also show that the 4.0 MHz Control inspection exhibits the least variant background noise signals whereas the 3.25 MHz measurement consistently gives the highest variation compared to the other two inspections. The reason behind this greater instability at 3.25 MHz is unknown.

### Sizing Uncertainty

One of the major uncertainties in this study is the accuracy of the crack sizing. The PoD cracks were sized using florescent dye penetrant inspection, but are therefore only a measure of the surface extent of the cracks. The actual geometry of the defects are unknown and this can therefore lead to anomalous results during ECT

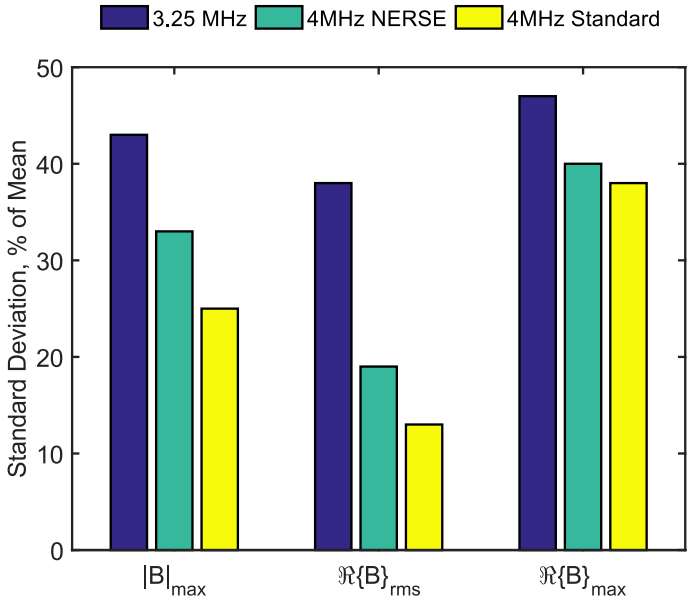


Figure 6.23: Percentage standard deviation of recorded noise values about their mean value for 3 noise measurement methods: $|B|_{rms}$, $\Re\{B\}_{rms}$ and $\Re\{B\}_{max}$, for the 3 different inspection techniques: 3.25 MHz, 4.0 MHz NERSE and 4.0 MHz Control.

inspection. This is reflected by the results shown in Figure 6.20.

The only way to account for this uncertainty is to measure the full extent of the defects via destructively breaking open the samples at the crack location and measuring using optical techniques. Unfortunately this measurement prevents the future use of the samples in PoD studies and was therefore not possible for this Thesis.

### Decision Threshold Variability

As discussed previously, defining the decision threshold, $a_{thresh}$, appropriately in PoD analysis is the most significant source of error as this parameter has the largest effect on the outcome of the PoD calculation. The use of a median filter to remove high frequency variations within the C-scan reduces the chances of arbitrarily high single pixels affecting the background noise measurement, however, there may

be some instances where the maximum background signal is misrepresented. The phase sensitive technique of recording noise, by measuring the maximum real component, $Re\{B\}_{max}$, was demonstrated to offer the most variable background noise measurement which therefore maximises the margin for $a_{thresh}$ error.

**Balance Drift**

Sometimes there may be a drift in the balance point of a C-scan. This can be gradual, which can be filtered out, but they can also be abrupt causing the background rest point of certain areas of the C-scan to not be at zero. This will lead to a misrepresentation of the defect and noise signals. Where possible any abrupt deviations from the zero point were corrected for by examining the Lissajous plots for each inspection. However, the corrections are only rough and so certain defect indications may have been misrepresented.

**Resonance Instability**

One of the major factors affecting the reliability of NERSE exploiting techniques is the stability of the resonant frequency over undamaged material. Because resonance is influenced by all manor of variables within an inspection there is a high probability of these variables causing a shift in the resonant frequency. The width of the NERSE signal peaks in the frequency spectrum offers some protection against these instabilities, however the smaller the defects the smaller the width of the sensitivity enhancing band of frequencies.

Where possible variables such as lift-off and tilt must be suppressed in order for the a NERSE-type operation to be viable. This is easily achieved within robotic scanning inspections which comprise a large proportion of high sensitivity inspections for high value manufacturing components.

There are however other factors that cannot be as easily suppressed to maintain a stable resonance peak. The most important of these is variability in

the coaxial cable environment supplying the coil. External contact with electrically non-neutral materials or bodies will introduce additional shunt capacitance to the transmission line, and will therefore have an effect on the frequency and intensity of resonance. The longer the cable, any environmental change to a small section of the cable will be relatively inconsequential to the fundamental resonance of the system compared to a shorter cable length. Longer cables however are more likely to traverse a wider variety of environments and are therefore more susceptible to slippage and shifting during an inspection. Measures can be taken to reduce the movement of the cable, i.e. by tying down the cables, but the ultimate aim would be to remove the coaxial cable from the measurement system altogether.

## 6.5 Grain Structure Study

To test the capability of the NERSE harmonic excitation method, a study was carried out to detect the grain colony boundaries in a large grained Ti-685 sample. As discussed in section 2.5.2 hexagonal close-packed (HCP) Ti-685 exhibits electrical anisotropy between the basal and c-axis planes of the crystal lattice (see figure 2.12). For Ti-685 samples of large enough colonies of unidirectional grains the boundary between grains of differing orientations acts as a material discontinuity which has been shown to disrupt eddy-currents in a measurable way [116, 119].

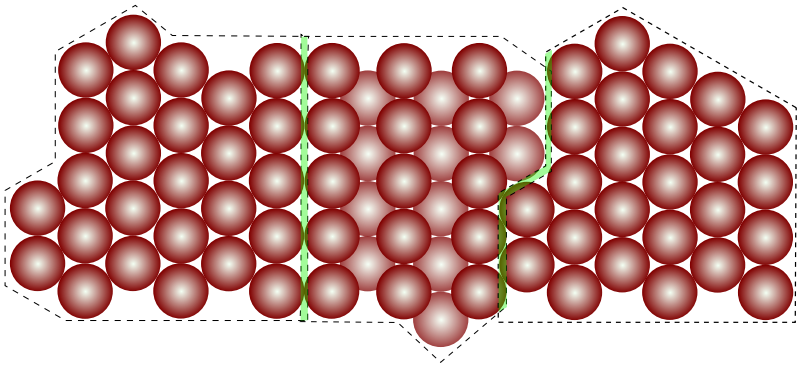

Figure 6.24: Diagram of grain boundary interfaces for a hexagonally close-packed material crystal lattice structure.

### 6.5.1 Experimental Procedure

The same probe setup (probe 2.a) and procedure as in section 6.4.2 was used to measure the effects of grain interfaces. A Ti-6Al-5Zr-0.5Mo-0.25Si (Ti-685 or IMI 685) sample containing large, millimetre scale, gains was used for the investigation figure 6.25.

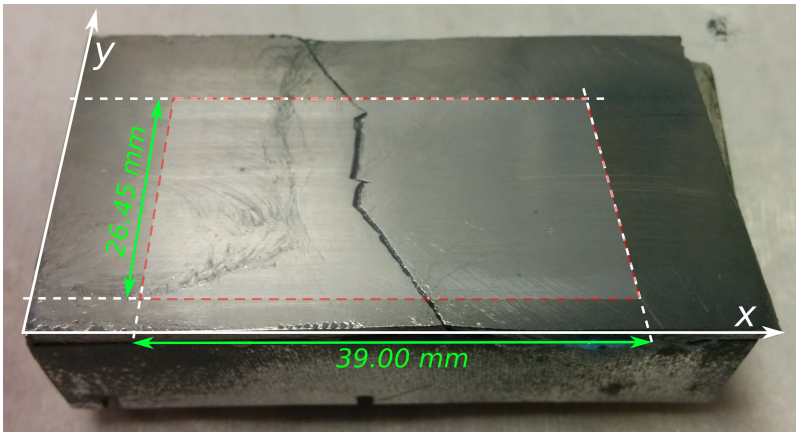


Figure 6.25: Photo of Ti-685 sample showing the $39.00 \times 26.45mm$ area of ECT scan.

Ti-685 is a commonly used aerospace material and is known as a near-alpha alloy as it is mostly alloyed with alpha phase stabilising elements and only 1-2% of beta phase stabilisers [10, 11]. It is therefore predominantly made up of HCP alpha-phase grains (see section 2.5.2) [166].

Spatially Resolved Acoustic Spectroscopy (SRAS) [167, 168] had been performed on the sample to establish the grain structure as shown in figure 6.26.a. SRAS is a laser based surface ultrasound technique which is used to measure the ultrasonic velocity of surface waves over short distances. The velocity of ultrasound materials is closely linked to the lattice structure, and HCP crystal structure exhibits anisotropy in the speed of ultrasound in certain orientations. This allows SRAS to build up an image of the surface grain structure of materials[1]. For more

[1]Sample and SRAS data supplied by Jethro Coulson from the University of Nottingham and Renishaw plc.

detailed information on SRAS, the reader is refereed to Sharples et al. [168].

A 4.0 MHz NERSE peak harmonic excitation measurement scan was made of a $39.00 \times 26.45$ $mm$ area of the surface of the Ti-685 sample (figure 6.25). The scan had a spatial resolution of $\Delta x = \Delta y = 0.15$ $mm$. The resulting scan data was analysed in both amplitude and phase to determine the effect of grain boundaries on the NERSE ECT measurements. The ECT data was measured and recorded as detailed in section 6.4.3. The SRAS and NERSE eddy-current scans of the same sample area are compared in figure 6.26. The SRAS scan data has a spatial resolution of, $\Delta x = 0.025$ $mm$ and $\Delta y = 0.050$ $mm$.

### 6.5.2 Results & Discussion

Figure 6.26.a shows the SRAS velocity map and figure 6.26.b shows the phase shift of the NERSE ECT measurement. The phase signal is used due to it's superior stability during the scan.

It is difficult to draw immediate correlation between the two data sets aside from the large fracture. In order to make a more meaningful comparison between the data sets, the grain boundaries were defined by calculating the local variance of each pixel within the SRAS velocity map for a $15 \times 15$ pixel window. The resulting image produces an outline of the grain boundaries of the material. The new image and the ECT phase shift data are overlaid in figure 6.27 with 50% transparency to demonstrate the correlation between the data sets.

The results shown in figure 6.27 demonstrate that the ECT measurement is significantly affected by grain boundaries in Ti-685. Work by Cherry et al. [119] has demonstrated that it is possible to replicate ECT signals from a map of grain orientations by averaging over circular current loops. However, this is not possible with this data set as the grain orientations are unknown.

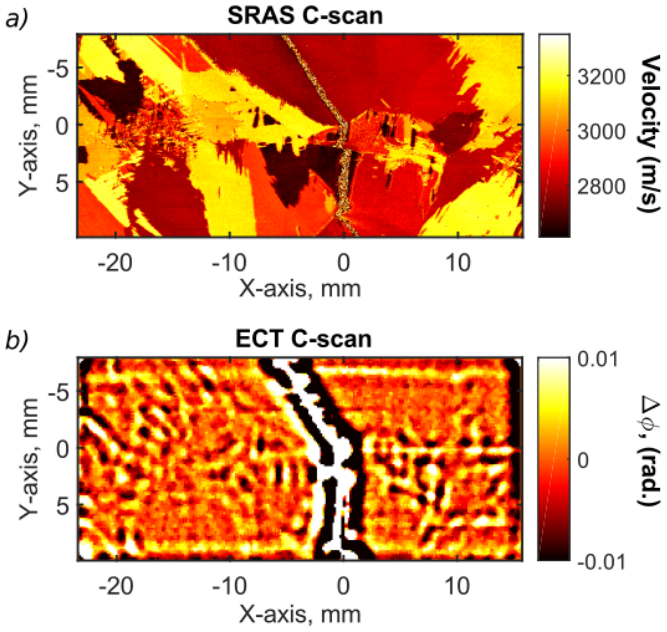


Figure 6.26: C-scan images of the large grain Ti-685 sample showing a) SRAS surface velocity measurements, and b) eddy-current phase difference, $\Delta\phi$, at 4.05 MHz NERSE peak harmonic excitation.

## 6.6 Conclusions

This chapter has experimentally shown that there exists a band of frequencies, outside the conventional operation range, and close to electrical resonance of an eddy current probe, where the magnitude of impedance SNR reaches a peak. This band is referred to as the near electrical resonance signal enhancement (NERSE) band and was examined for three discontinuities of varying depth in Titanium 6-4 using chirp excitation between 1-5 MHz. The SNR of the chirp frequency spectra at the peak NERSE frequency was enhanced by a factor of up to 8.5, from the SNR at 1MHz. NERSE frequency operation has significant potential for ECT inspection, and opens up a range of investigative possibilities.

1-5 MHz chirp excitation measurements were performed on 15 machined discontinuities in Titanium 6-4, and the measured frequency spectra recorded and analysed. It was demonstrated that critical features of chirp frequency spectra of

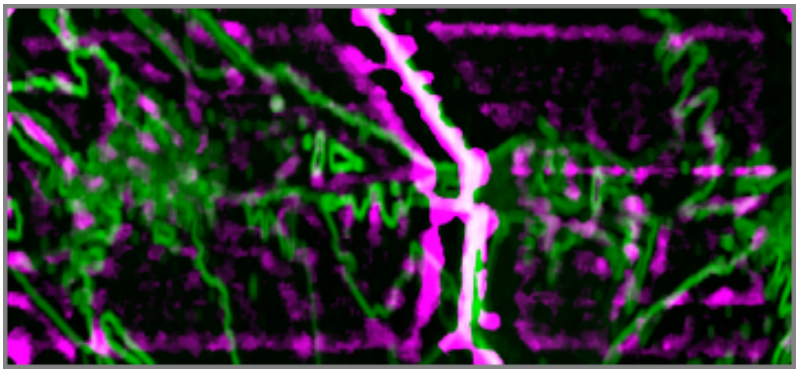

Figure 6.27: C-scan images of the large grain Ti-685 sample showing overlaid transparent images of the local variance of SRAS surface velocity from a $15 \times 15$ pixel window (Green), and eddy-current phase difference, $\Delta\phi$, at 4.05 MHz NERSE peak harmonic excitation (Purple).

a artificial defect (peak amplitude and frequency) are dependant on the geometry of the defects. As the size of a given simulated defect increases the peak amplitude increases. The peak frequency changes as a result of defect geometry were less definitive with some changes in defect dimension causing a continuous decrease in peak frequency, and other defect dimension changes causing a more complicated frequency peak response. The sample set of defects investigated within this study was not large enough to draw any definitive conclusions about the trends in NERSE chirp signals resulting from changes in simulated defect dimensions. However, it is clear that critical parameter analysis of chirp measurements could potentially be used to infer dimensional information about macro-scale discontinuities or material features i.e larger than the coil dimensions.

It was demonstrated that the chirp measurement of sub-mm simulated defects in Ti6-4 was susceptible to error as a result of high background electrical noise. This prevents the accurate analysis of the chirp signals from such defects using this approach in its current state. Real cracks have much more complicated and non-ideal structures compared to machined defects and so their effect on resonance will be less well defined. One of the simplest methods of solving this issue is to operate at a single frequency at the NERSE peak frequency and average over a number of

cycles to remove incoherent noise. Electrical noise will have negligible effect on the electrical resonant frequency of the probe and so as long as the decoupling resonance-shift caused by the material noise, i.e. the microstructure, is less than that caused by any defects, then a signal enhancement effect should be observed.

It has been shown that the harmonic excitation of an ECT probe within the NERSE frequency band (see chapter 6.3), results in a significant improvement in the sensitivity of inspection. The sensitivity of this technique, relative to conventional probe operation methods, was statistically analysed by carrying out a probability of detection (PoD) study on a large number of fatigue cracks in Ti6-4. The results show that harmonic excitation within the NERSE frequency band improves the sensitivity of a standard ECT probe. The 2 mm diameter ferrite-cored probe demonstrated a reliably detectable defect size, defined by PoD analysis as $a_{90/95}$, when operating at the peak NERSE frequency (here 4.0 MHz) of 0.82 mm. This was compared to the same probe operated at the maximum frequency limit for conventional inspection techniques (3.25 MHz), which achieved an $a_{90/95}$ of 1.09 mm. The sensitivity improvement observed by operating at the NERSE peak frequency was validated by performing an additional PoD study, this time operating the same probe with a lower capacitance (i.e. higher electrical resonant frequency) and operating at the same frequency as the previous NERSE operation inspection (4.0 MHz). The $a_{90/95}$ of this measurement, well away from the electrical resonance, was 0.94 mm. An improvement from the 3.25 MHz inspection, but not as sensitive as the NERSE inspection.

It was also shown, via the analysis of background noise data from each of the inspection techniques, that operating at the higher frequency within the NERSE frequency band appeared to result in an improvement in the stability of the background noise signals when compared to the standard operation frequency of 3.25 MHz. This result could be anomalous and may be a feature of the specific coil geometry and design, or even a result of the specific material properties. Further

studies would be required in order to verify if this effect is a feature of operation near electrical resonance.

The effect of material grain structure on background material noise was also investigated. It was shown that the NERSE peak frequency excitation measurement is capable of detecting grain interfaces in large grained Titanium alloys (Ti-685). Detecting these interfaces shows that this measurement is more than sensitive enough to detect tightly closed defects as crack propagation is more likely along grain boundaries. Due to the large dimensions of the measurement probe, the grain boundaries of the material in the resulting c-scan are poorly resolved. However, through comparison with data obtained by spatially resolved acoustic spectroscopy (SRAS) of the same sample, a clear, albeit qualitative, correlation exists between the eddy-current measurements and the grain boundaries. Research has already demonstrated that ECT measurements of grain boundaries can be replicated from grain micro-structure maps [119]. Achieving this sensitivity shows how the grain boundaries in materials such as Titanium 6-4 influence the eddy-current path thereby increasing the background noise level compared to other more isotropic and homogeneous materials. This demonstrates the difficulties in inspecting for sub-millimetre defects in such aerospace alloys as Ti-685 and Ti6-4.

Regardless of the effect on background noise, operating within the NERSE band of an electrically resonating probe results in a significant sensitivity improvement to standard ECT probe geometries and designs. The effect can therefore be exploited to improve the detectable limit of inspections or be used to push to reliably find smaller defects. This can both improve the sensitivity and extend the lifetime of ECT inspections within industry, as the demand for higher sensitivity inspections intensifies. The operational technique shown within this chapter can be easily developed into an industrially applicable ECT system for single coil inspection. The next stage of development would be to incorporate NERSE-type measurements within array probes.

# Chapter 7

# Conclusions & Future Work

## 7.1 Introduction

This thesis has investigated eddy-current inspection methods for the detection of sub-millimetre surface breaking defects in safety critical aerospace superalloys, namely Ti6-4. The surface of these materials can be problematic for ECT inspections, and many other techniques, due to their low electrical conductivity, electrical anisotropy along certain crystal lattice axes, and sometimes large grain structures (see theory section 2.5 and experimental section 6.5). This thesis therefore explored the current limitations of high sensitivity ECT inspections of these materials and summarises novel research into the development of more sensitive ECT techniques for these applications.

## 7.2 Thesis Review

The critical findings of this thesis are summarised in the sections below.

### 7.2.1 High Sensitivity ECAs

A drive towards the use of eddy-current array (ECA) techniques for the inspection of safety critical materials has been identified in industry and so a study into the

limitations of a typical, high sensitivity, eddy-current array (ECA) inspection probe measurement was performed (see chapter 4).

Due to a desire within industry to balance sensitivity, coverage and cost when purchasing an ECA probe, the probes are unlikely to be more sensitive than is required. It is more common for these probes to be on the limits of what is necessary in order to cost effectively offer what the industrial user wants, whilst balancing these three criteria stated. As a result coil elements within probes may sometimes be significantly larger than the target defect so as to achieve the desired coverage of the probe. An investigation into how this affects sensitivity to a given target defect was carried out.

The first study mapped the sensitivity variation of a 1.0 MHz transmit-receive (TR) configuration ECA probe (section 4.2.1), to a machined target defect (0.75×0.38×0.10 mm). The results show that the TR channel measurements form overlapping Gaussian sensitivity bell curves. Due to the larger size of the coil elements (2.4 mm diameter) the overlapping sensitivity bells generate an overall sensitivity profile that varies significantly with target defect position under the array (section 4.3.2). This means there are periodic high and low sensitivity regions in an array which increases the likelihood of smaller defects going undetected if they fall within a sensitivity minimum.

The second study was a statistical analysis of the probe's inherent sensitivity, made via probability of detection (PoD) analysis (see appendix A) of 39 real fatigue cracks of varying size in Ti6-4 samples. The resulting probability for detection curve predicted that the smallest reliably detectable defect, $a_{90/95}$, of the ECA inspection was 1.21 mm long. This value is reflective of the sensitivity variation.

### 7.2.2 Near Electrical Resonance Signal Enhancement (NERSE)

The behaviour of electrical resonance in the presence of material discontinuities was investigated and a band of frequencies just below the resonant frequency of the

ECT probe were identified as exhibiting significant signal enhancements to material discontinuities (section 5.4.3). This phenomenon, termed near electrical resonance signal enhancement (NERSE), is a direct result of the electrical resonance of the inspection probe, shifting frequency (in non-ferromagnetic materials, it shifts to lower frequencies) in the presence of discontinuities. The effect is equivalent to the inspection coil decoupling from the material in the equivalence circuit transformer model (see section 3.7.3). However, it was demonstrated that the behaviour of electrical resonance is different for discontinuities and lift-off changes.

Studies were performed (section 6.3) using MHz chirp excitation techniques to excite a range of frequencies around electrical resonance and observe the frequency response spectrum of the probe in the presence of different artificial defects in Ti6-4 samples. The frequency response spectra from the chirp measurements exhibit intriguing changes as a function of the dimensions of the artificial defects, however, due to the small sample set no conclusive trends can be claimed from the work. Future work will look at developing a greater theoretical understanding of the resonance behaviour with discontinuity geometry, beyond simple circuit diagrams, and use this to assist in the analysis of chirp measurements. It is thought that the frequency spectra produced by such a measurement could be used to more accurately size defects via inversion models that exploit frequency dependant behaviour such as those developed by Tamburrino and Rubinacci [169]. This could be implemented for sizing large defects and features but the current limitation is the size of the excitation coil relative to the target defect. It was observed that defects smaller than this dimension suffer from greater noise in the frequency spectrum making the analysis of the frequency response prone to greater error.

To exploit the NERSE effect for the inspection of sub-millimetre defects, smaller than the coil diameter, single frequency excitation at the peak NERSE frequency should be used. It was shown via another probability of detection (PoD) study in section 6.4 that by operating at a single excitation frequency, carefully

selected to be at the optimum NERSE frequency, a significant improvement in inspection sensitivity was achievable for a given ECT probe (table 6.7).

The observation and characterisation of the NERSE effect has introduced the possibility of increasing the sensitivity to smaller defects via a simple procedural change. Such an approach could improve the SNR for small defects where, at conventional frequency operation, the signal from the defect would be below the electrical background noise. This has significant industrial impact as it would allow standard ECT inspections to achieve greater sensitivity, which would instil greater confidence in the structure of safety critical components thereby extending their service lifetime. Alternatively the increased inspection capability could be fed back into the production of these components such that they can be redesigned with less redundant material, saving weight and cost. This it critical in the aerospace sector.

## 7.3 Future Work

There have been many intriguing developments documented in this thesis arising from the NERSE phenomenon that require further investigation. This thesis predominately analysed the signal magnitude of the NERSE inspections carried out, both for chirp and harmonic modes of operation. However, it was equally noted that the phase around electrical resonance also exhibited significant changes in the presence of discontinuities. Unfortunately due to time constraints, a full analysis and statistical validation of using the phase at resonance was not made. It would therefore be prudent to carry out this work first. The same experimental approach would be used as in chapter 6.4, but this time instead of picking the peak NERSE frequency in the magnitude spectrum, the peak frequency in the equivalent phase spectrum would be selected (see figure 6.10). It is entirely possible that a phase measurement exhibits an even greater stability and sensitivity to discontinuities.

In line with the transfer of technology to industry, the development of prac-

tical industrial techniques should be the dominant focus of future work. It would be a simple step to developing a practical single frequency NERSE technique.

The first stage of future work should be focused on developing a robust system for performing NERSE measurements. Regardless of whether the measurement is made at the NERSE peak frequency in magnitude or phase, the system used must be reliable and ideally adaptable to different applications. One of the limiting factors affecting this is resonance noise or drift. Resonance shifting could be caused by a number of external influences including temperature or even humidity, however one of the major, and more dominant influences is the coaxial cable environment. Changes in the coaxial cables environment can have a significant affect on the electrical resonance (see section 5.3) which, during an inspection would be extremely detrimental.

One way of eliminating this instability would be to capacitively load excitation coils with capacitors that outweigh the capacitance of the coaxial cable (i.e. load capacitance should be 10× cable capacitance). The capacitance of the system could be changed in order to set the electrical resonance of the inspection based on the application criteria i.e. lower excitation frequencies. This would however require careful probe coil design in order to balance the inductance of the system for a given resonant frequency. An advancement in reducing the effect of the coaxial cable would be to integrate the Howland current source electronics into the probe, thereby eliminating the need for coaxial cable and allowing a coil to be operated within a much larger frequency range.

After that, work on incorporating NERSE measurement techniques into ECA probes would be the logical direction of the research. With ECA probes the potential for multi-coil NERSE measurements would become possible. Investigations should be performed on multiple coil configurations and with a range of coil impedance profiles. Closely neighbouring coil elements will couple to one another regardless of whether the coil is excited. This introduces additional inductive and

capacitive elements to the equivalence circuit model. The effect this has on the resonant frequency, as well as the Q-factor, is unknown and so a detailed understanding of how these things vary with coil design proximity and number of coil elements is essential for exploiting NERSE phenomenon in ECAs. Aside from being a complicated problem, the behaviour of resonance in closely packed coils could be beneficial for the detection and sizing of defects and the endless possibilities in terms of transmit-receive measurements operated in pulsed, chirped or single frequency could open up entirely new ways of measuring and characterising surface conditions.

# Appendix A

# Probability of Detection

Probability of detection (PoD) analysis was applied to different ECT methods within this Thesis to establish the reliable sensitivity of an inspection method. The details of how PoD curves are calculated is detailed below.

## A.1 Probability of Detection (PoD)

Probability of detection (PoD) is a quantitative measure of the reliability and sensitivity of NDT techniques. It establishes the smallest defect that can be reliably detected by a given inspection technique by statistically analysing the signal response distribution of a large number of real fatigue defect inspections.

### A.1.1 PoD Specimens

A three-point bending method (Figure A.1) was used to generate a distribution of real surface breaking cracks in Ti6-4 bar samples (figure A.2) [170]. The cracks vary in surface length from 0-6.48mm, as measured by dye-penetrant testing. The specimens vary in surface condition with typical surface roughness ranging from $0.15 - 1.25 \pm 0.05\mu m$ as measured by a Taylor Hobson (Leicester, UK) Surftronic 25.

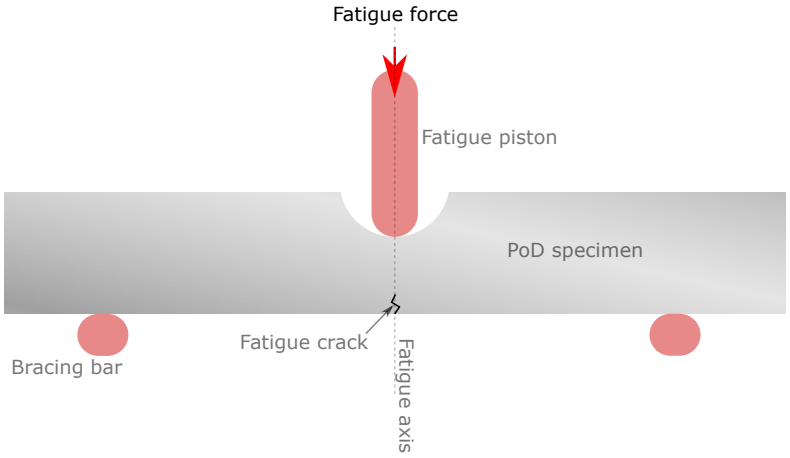


Figure A.1: Schematic of 3-point bend technique for the generation of fatigue cracks.

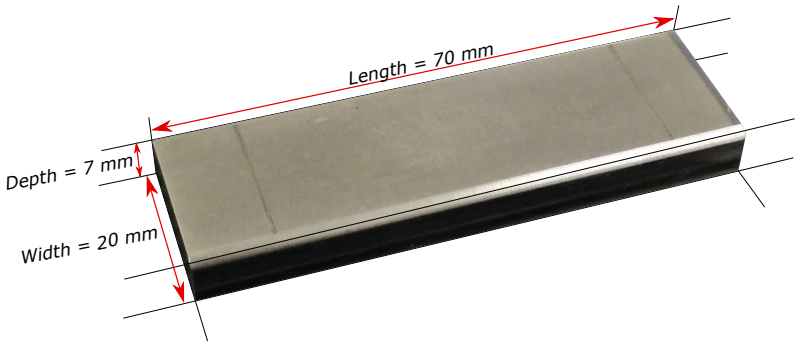


Figure A.2: Image of PoD sample and it's dimensions.

### A.1.2 Signal Response Data PoD

There are two methods of PoD analysis; Hit or Miss (inspection returns a defect or no defect response) or Signal Response (inspection returns a quantitative value for the defect). The method used is dependent upon the type of inspection performed, and for ECT inspections, the latter method is implemented [154].

The initial step of the PoD analysis is to determine a correlation between the defect size ($a$) and signal response ($\hat{a}$) so that an expected signal response can be predicted for a defect of any size. This is why the signal response method is often

referred to as a-hat vs. a analysis. Figure A.3.a shows an example of a distribution of signal responses on a log-log plot with a linear best fit.

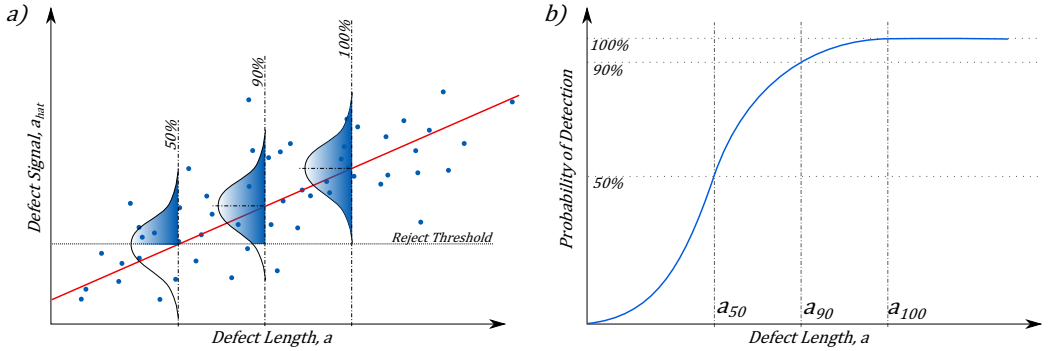


Figure A.3: Example of a-hat vs a log-log plot showing normal distributions around predicted defect signal responses (a) and a Probability of Detection (PoD) curve (b), with 95% confidence band (blue-dotted line). After [171]

Empirical studies have shown that an approximate linear relationship exists between $\ln \hat{a}$ and $\ln a$ [171]. This relationship is expressed by the formula,

$$y = \alpha_1 + \beta_1 x + \gamma \tag{A.1}$$

where,

$$x = \ln a, \tag{A.2}$$

$$y = \ln \hat{a}. \tag{A.3}$$

$\alpha_1$ is the signal response at , $\beta_1$ is the gradient and $\gamma$ represents the random variability of the experimental data. The term $\alpha_1 + \beta_1 x$ is the mean signal response, $\mu$, of the inspection to a given $x$ [171].

The associated uncertainty with the predicted signal response, $\gamma$ , is related to the variability of the experimental response data. This variability arises due to all manner of experimental parameters including variations in lift-off, tilt, scanning resolution, defect geometry and orientation as well as all possible human errors in both

taking and interpreting the data from the inspection. There are many authors who seek to increase the sample size and thereby improve the accuracy of PoD analysis by modelling these experimental variations and reflecting that in the distribution of the experimental data [68].

It is assumed that $\gamma$ is normally distributed with zero mean and a constant standard deviation, $\sigma$ [171]. The expression for a normal distribution function, $\aleph(\xi \mid \mu, \sigma)$ is defined as,

$$\aleph(\xi \mid \mu, \sigma) = \frac{1}{\sigma\sqrt{2\pi}} \exp\left\{\frac{(\xi - \mu)^2}{2\sigma^2}\right\} \tag{A.4}$$

The parameter $\xi$ denotes the axis that the normal distribution is spread across, centred on the mean $\mu$ for a given defect size, $a$, (see figure A.3.a). The denominator in equation A.4 forces the area under the distribution to unity. The standard deviation $\sigma$, and therefore the variance, $\sigma^2$, can be calculated from the residuals of the experimental data relative to the predicted signal response.

The signal threshold $\hat{a}_{th}$ can be set to any desired value to reduce the likelihood of false calls. The typical standard in industry is 2-3 times the maximum value of noise recorded during the inspection. Any signals measured above this level result in the rejection of the part. The probability of detecting a defect of size $a$, is equal to the probability of the defect signal response being larger than the decision threshold, $\hat{a}_{th}$, which can be expressed as,

$$PoD(a) = Probability\{\hat{a} > \hat{a}_{th}\} \tag{A.5}$$

The probability of detection for a defect of a particular size, $PoD(a)$, is therefore equivalent to the area under the normal distribution curve that lies above the decision threshold, $\ln(\hat{a}_{th})$, for that particular size $a$. This can be expressed in log space

as an integration of equation A.4 as given by,

$$PoD(a) = \int_{\ln(\hat{a}_{th})}^{\infty} \aleph\left(y \mid \mu, \sigma\right) \, \mathrm{d}y, \tag{A.6}$$

$$= \frac{1}{\sigma\sqrt{2\pi}} \int_{\ln(\hat{a}_{th})}^{\infty} \exp\left\{\frac{(y-\mu)^2}{2\sigma^2}\right\} \, \mathrm{d}y, \tag{A.7}$$

Equation A.7 cannot be solved analytically. Instead the solution must be expressed using the cumulative distribution function (CDF), $\Phi$, defined as,

$$\Phi\left(\frac{z-\mu}{\sigma}\right) = \frac{1}{\sigma\sqrt{2\pi}} \int_{-\infty}^{z} \exp\left\{\frac{(\xi-\mu)^2}{2\sigma^2}\right\} \, \mathrm{d}\xi \tag{A.8}$$

Due to the symmetry of the normal distribution about the mean and it's unity, $\Phi(-z) = 1 - \Phi(z)$, such that,

$$\frac{1}{\sigma\sqrt{2\pi}} \int_{z}^{\infty} \exp\left\{\frac{(\xi-\mu)^2}{2\sigma^2}\right\} \, \mathrm{d}\xi = 1 - \Phi\left(\frac{z-\mu}{\sigma}\right) \tag{A.9}$$

$$= \Phi\left(-\frac{z-\mu}{\sigma}\right) \tag{A.10}$$

Inputing equation A.1 into equation A.7 and equating it to equation A.10,

$$\frac{1}{\sigma\sqrt{2\pi}} \int_{\ln(\hat{a}_{th})}^{\infty} \exp\left\{\frac{(y-\alpha_1+\beta_1 x)^2}{2\sigma^2}\right\} \, \mathrm{d}y, = \Phi\left(-\frac{\ln(\hat{a}_{th}) - (\alpha_1+\beta_1 x)}{\sigma}\right). \tag{A.11}$$

The probability of detection can therefore be expressed as,

$$PoD(a) = \Phi\left(-\frac{x-\hat{\mu}}{\hat{\sigma}}\right), \tag{A.12}$$

by defining a new variables,

$$\hat{\mu} = \frac{\ln(\hat{a}_{th}) - \alpha_1}{\beta_1}, \tag{A.13}$$

$$\hat{\sigma} = \frac{\sigma}{\beta_1}. \tag{A.14}$$

There is no exact solution to the cumulative distribution function in order to produce the PoD curve. Hence approximate solutions must be used. One such approximation is the inverse-logit function defined as [172],

$$\Phi(\xi) \approx \frac{1}{1+e^{\xi}}. \tag{A.15}$$

A more accurate approximation can be achieved using the Taylor expansion [173],

$$\Phi(\xi) = \frac{1}{2}\left[1 + \frac{2}{\sqrt{\pi}}\sum_{n=0}^{\inf}\frac{(-1)^n(\xi/\sqrt{2})^{2n+1}}{n!(2n+1)}\right]. \tag{A.16}$$

Multiple defects all of the same size $a$, will produce signal responses that form a normal distribution around the predicted $\hat{a}$ value given by the best fit curve (figure A.3). For any value of $a$, the probability of detecting the defect (i.e. a signal above the threshold) is equivalent to percentage of the normal distribution that lies above the threshold $\hat{a}_{th}$ (see figure A.3.a).

The PoD curve is a plot of defect length, $a$, verses the probability of detection (figure A.3.b) and is a measure of how likely is it that a defect of size $a$ will have a signal response greater than the threshold [154].

PoD analysis returns a value for the smallest reliably detectable crack, $a_{90}$, which is defined as the crack size on the PoD curve with a 90% PoD. However, if PoD analysis was performed on a different set of samples, the $a_{90}$ value would be different. If the analysis was performed on an infinite number of samples, the $a_{90}$ value would converge on the true value of the inspection technique.

If 100 independent PoD tests were performed on 100 different sets of samples (each set containing a finite number of samples), then a distribution of $a_{90}$ values would be produced around the true $a_{90}$ value. The distribution would be such that 95 of these values would be greater than the true $a_{90}$. To reflect this, it is common for the $a_{90}$ value to be quoted with a confidence level of 95%, referred to as $a_{90/95}$ i.e. $a_{90/95}$ is greater than the true value of $a_{90}$ 95% of the time [154].

# Bibliography


[1] RS components part 6655870 â rg58 C/u PVc, manufacturer details, retrieved (08/10/12). Online, 2012.

[2] RS components part 6655855 â rg174 A/u PVc, manufacturer details, retrieved (17/09/15). Online, 2015. URL http://docs-europe.electrocomponents.com/webdocs/141f/0900766b8141f0ac.pdf.

[3] Los Angeles Times. 2 killed as engine parts pierce cabin of delta jet, July 1996. URL http://articles.latimes.com/1996-07-07/news/mn-22049_1_jet-engine.

[4] National Transportation Safety Board. Aircraft accident report - united airlines flight 232, mcdonnell douglas dc-10-10, sioux gateway airport, sioux city, iowa, july 19, 1989. Aircraft Accident Report NTSB/AAR-90/06, National Transportation Safety Board, National Transportation Safety Board, Office of Aviation Safety, Washignton D.C. 20594, November 1990.

[5] Aviation Safety Network. Accident description - lot polskie linie lotnicze, flight no. lo5055. Online, May 1987. URL http://aviation-safety.net/database/record.php?id=19870509-0.

[6] Aviation Safety Network. Accident description - lot polskie linie lotnicze, flight no. 007. Online, March 1980. URL http://aviation-safety.net/database/record.php?id=19800314-1.

[7] M.G. Silk, A.M. Stoneham, and J.A.G. Temple. *The reliability of non-destructive inspection: assessing the assessment of structures under stress*. A. Hilger, 1987. ISBN 9780852745335.

[8] W.J. McGonnagle. *NonDestructive Testing, Second Edition,*. Defense Technical Information Center, 1961.

[9] R.A. Adamesku, L.P. Andreeva, P.V. Gel'd, E.A. Mityushov, and N.D. Reimer. Anisotropy of elastic properties of titanium base $\alpha$-alloys. *Strength of Materials*, 14(9):1284–1287, 1982. ISSN 0039-2316. doi: 10.1007/BF00779952. URL `http://dx.doi.org/10.1007/BF00779952`.

[10] Adrian P. Mouritz. 9 - titanium alloys for aerospace structures and engines. In Adrian P. Mouritz, editor, *Introduction to Aerospace Materials*, pages 202 – 223. Woodhead Publishing, 2012. ISBN 978-1-85573-946-8. doi: http://dx.doi.org/10.1533/9780857095152.202. URL `http://www.sciencedirect.com/science/article/pii/B9781855739468500091`.

[11] G. Welsch, R. Boyer, and E.W. Collings. *Materials Properties Handbook: Titanium Alloys*. Materials properties handbook. ASM International, 1993. ISBN 9780871704818. URL `http://books.google.co.uk/books?id=x3rToHWOcD8C`.

[12] D.E. Bray and D. Mcbride. *Nondestructive testing techniques*. New York, NY (United States); John Wiley Sons, Inc., Jan 1992.

[13] D. Francis. 4 - non-destructive evaluation (nde) of composites: introduction to shearography. In Vistasp M. Karbhari, editor, *Non-Destructive Evaluation (NDE) of Polymer Matrix Composites*, Woodhead Publishing Series in Composites Science and Engineering, pages 56 – 83. Woodhead Publishing, 2013. ISBN 978-0-85709-

344-8. doi: http://dx.doi.org/10.1533/9780857093554.1.56. URL http://www.sciencedirect.com/science/article/pii/B978085709344850004X.

[14] D P Almond and S K Lau. Defect sizing by transient thermography. i. an analytical treatment. *Journal of Physics D: Applied Physics*, 27(5):1063, 1994. URL http://stacks.iop.org/0022-3727/27/i=5/a=027.

[15] D.J. Titman. Applications of thermography in non-destructive testing of structures. {*NDT*} *& E International*, 34(2):149 – 154, 2001. ISSN 0963-8695. doi: http://dx.doi.org/10.1016/S0963-8695(00)00039-6. URL http://www.sciencedirect.com/science/article/pii/S0963869500000396.

[16] Adrian P. Mouritz. 23 - nondestructive inspection and structural health monitoring of aerospace materials. In Adrian P. Mouritz, editor, *Introduction to Aerospace Materials*, pages 534 – 557. Woodhead Publishing, 2012. ISBN 978-1-85573-946-8. doi: http://dx.doi.org/10.1533/9780857095152.534. URL http://www.sciencedirect.com/science/article/pii/B9781855739468500236.

[17] S.E. Burrows, S. Dixon, S.G. Pickering, T. Li, and D.P. Almond. Thermographic detection of surface breaking defects using a scanning laser source. {*NDT*} *& E International*, 44(7):589 – 596, 2011. ISSN 0963-8695. doi: http://dx.doi.org/10.1016/j.ndteint.2011.06.001. URL http://www.sciencedirect.com/science/article/pii/S0963869511000740.

[18] W. J. Parker, R. J. Jenkins, C. P. Butler, and G. L. Abbott. Flash method of determining thermal diffusivity, heat capacity, and thermal conductivity. *Journal of Applied Physics*, 32(9): 1679–1684, 1961. doi: http://dx.doi.org/10.1063/1.1728417. URL http://scitation.aip.org/content/aip/journal/jap/32/9/10.1063/1.1728417.

[19] Jack Blitz and Geoff Simpson. *Ultrasonic methods of non-destructive testing*. Springer, 1996. ISBN 9780412604706.

[20] Q. Shan and R. J. Dewhurst. Surface breaking fatigue crack detection using laser ultrasound. *Applied Physics Letters*, 62(21):2649–2651, 1993. ISSN 0003-6951. doi: 10.1063/1.109274.

[21] M. Hirao and H. Ogi. *Emats for Science and Industry: Noncontacting Ultrasonic Measurements,*. Kluwer Academic Publishers, 2003. ISBN 9781402074943.

[22] L.C. Lynnworth. *Ultrasonic measurements for process control: theory, techniques, applications,*. Academic Press, 1989. ISBN 9780124605855.

[23] X. Jian, S. Dixon, K. T. V. Grattan, and R. S. Edwards. A model for pulsed Rayleigh wave and optimal emat design. *Sensors and Actuators A: Physical*, 128(2):296–304, 2006. ISSN 0924-4247. doi: 10.1016/j.sna.2006.01.048.

[24] Christopher B Scruby and Leslie E Drain. *Laser ultrasonics techniques and applications*. CRC Press, 1990.

[25] P. Wilcox, M. Lowe, and P. Cawley. Omnidirectional guided wave inspection of large metallic plate structures using an emat array. *Ultrasonics, Ferroelectrics and Frequency Control, IEEE Transactions on*, 52(4):653–665, 2005.

[26] R. S. Edwards, S. Dixon, and X. Jian. Characterisation of defects in the railhead using ultrasonic surface waves. *NDT & E International*, 39(6):468–475, 2006. ISSN 0963-8695. doi: 10.1016/j.ndteint.2006.01.005.

[27] Y. Fan, S. Dixon, R. S. Edwards, and X. Jian. Ultrasonic surface wave propagation and interaction with surface defects on rail track head. *NDT & E International*, 40(6):471–477, 2007. ISSN 0963-8695. doi: 10.1016/j.ndteint.2007.01.008.

[28] P. Palanichamy, A. Joseph, T. Jayakumar, and Baldev Raj. Ultrasonic velocity measurements for estimation of grain size in austenitic stainless steel. *NDT*

*& E International*, 28(3):179–185, 1995. ISSN 0963-8695. doi: 10.1016/0963-8695(95)00011-l.

[29] C. Wick, R.F. Veilleux, and Society of Manufacturing Engineers. *Tool and Manufacturing Engineers Handbook: Materials, finishing and coating,*. Society of Manufacturing Engineers, 1985. ISBN 9780872631762.

[30] J. Larsen, B. Worth, C. Annis, and F. Haake. An assessment of the role of near-threshold crack growth in high-cycle-fatigue life prediction of aerospace titanium alloys under turbine engine spectra. *International Journal of Fracture*, 80(2):237–255, 1989. ISSN 0376-9429. doi: 10.1007/bf00012671.

[31] R. Halmshaw. *Industrial Radiology: Theory and Practice*. Non-Destructive Evaluation Series. Springer Netherlands, 1995. ISBN 9780412627804. URL `https://books.google.co.uk/books?id=wJqBSA1exqoC`.

[32] J.E. Lenz. A review of magnetic sensors. *Proceedings of the IEEE*, 78(6): 973–989, Jun 1990. ISSN 0018-9219. doi: 10.1109/5.56910.

[33] KF Bainton. Characterizing defects by determining magnetic leakage fields. *NDT International*, 10(5):253–257, 1977.

[34] T. Kundu. *Ultrasonic and Electromagnetic NDE for Structure and Material Characterization: Engineering and Biomedical Applications*. CRC Press, 2012. ISBN 9781466570474. URL `https://books.google.co.uk/books?id=6F_OBQAAQBAJ`.

[35] G. Birnbaum, G.M. Free, and G. Free. *Eddy-Current Characterization of Materials and Structures*. ASTM STP 722. American Society for Testing and Materials, 1981. ISBN 9780803107526. URL `https://books.google.co.uk/books?id=Xm7QUkm_E9QC`.

[36] Bruce W. Drinkwater and Paul D. Wilcox. Ultrasonic arrays for non-destructive evaluation: A review. *NDT & E International*, 39(7):525–541, 2006. ISSN 0963-8695. doi: 10.1016/j.ndteint.2006.03.006.

[37] T. Takagi, J.R. Bowler, and Y. Yoshida. *Electromagnetic Nondestructive Evaluation*. Number v. 1 in Electromagnetic Nondestructive Evaluation. IOS Press, 1997. ISBN 9789051993257. URL `https://books.google.co.uk/books?id=pcbbZ7EPW14C`.

[38] Raimond Grimberg, Lalita Udpa, Adriana Savin, Rozina Steigmann, Valerian Palihovici, and Satish S. Udpa. 2D eddy current sensor array. *NDT & E International*, 39(4):264–271, 2006. ISSN 0963-8695. doi: 10.1016/j.ndteint.2005.08.004.

[39] H. A. Wheeler. Formulas for the skin effect. *Proceedings of the IRE*, 30(9): 412–424, 1942. ISSN 0096-8390. doi: 10.1109/JRPROC.1942.232015.

[40] G. Almeida, J. Gonzalez, L. Rosado, P. Vilaa, and Telmo G. Santos. Advances in {NDT} and materials characterization by eddy currents. *Procedia {CIRP}*, 7:359 – 364, 2013. ISSN 2212-8271. doi: http://dx.doi.org/10.1016/j.procir.2013.05.061. URL `http://www.sciencedirect.com/science/article/pii/S2212827113002680`. Forty Sixth {CIRP} Conference on Manufacturing Systems 2013.

[41] D. E. Hughes. V. induction-balance and experimental researches therewith. *Philosophical Magazine Series 5*, 8(46):50–56, 1879. ISSN 1941-5982. doi: 10.1080/14786447908639649.

[42] W.E. Gardner. *Improving the effectiveness and reliability of non-destructive testing,*. Pergamon Press, Oxford, 1992. ISBN 0080369812.

[43] T. Theodoulidis. Analytical model for tilted coils in eddy-current nondestruc-

tive inspection. *Magnetics, IEEE Transactions on*, 41(9):2447–2454, September 2005. ISSN 0018-9464. doi: 10.1109/TMAG.2005.854331.

[44] Javier García-Martín, Jaime Gómez-Gil, and Ernesto Vázquez-Sánchez. Non-destructive techniques based on eddy current testing. *Sensors*, 11 (3):2525–2565, 2011. ISSN 1424-8220. doi: 10.3390/s110302525. URL `http://www.mdpi.com/1424-8220/11/3/2525`.

[45] Jack Blitz. *Electrical and magnetic methods of non-destructive testing,*. Non-Destructive Evaluation Series. Chapman & Hall, 1997. ISBN 9780412791505.

[46] R. Grimberg, A. Savin, E. Radu, and O. Mihalache. Nondestructive evaluation of the severity of discontinuities in flat conductive materials by an eddy-current transducer with orthogonal coils. *Magnetics, IEEE Transactions on*, 36(1): 299–307, 2000. ISSN 0018-9464.

[47] Javier O. Fava, Liliana Lanzani, and Marta C. Ruch. Multilayer planar rectangular coils for eddy current testing: Design considerations. *NDT & E International*, 42(8):713–720, 2009. ISSN 0963-8695. doi: 10.1016/j.ndteint.2009.06.005.

[48] V. Zilberstein, D. Grundy, V. Weiss, N. Goldfine, E. Abramovici, J. Newman, and T. Yentzer. Early detection and monitoring of fatigue in high strength steels with MWM-arrays. *International Journal of Fatigue*, 27(10):1644–1652, 2005. ISSN 0142-1123. doi: 10.1016/j.ijfatigue.2005.07.028.

[49] Vladimir Zilberstein, Darrell Schlicker, Karen Walrath, Volker Weiss, and Neil Goldfine. MWM eddy current sensors for monitoring of crack initiation and growth during fatigue tests and in service. *International Journal of Fatigue*, 23, Supplement 1(0):477–485, 2001. ISSN 0142-1123. doi: 10.1016/S0142-1123(01)00154-2.

[50] Vladimir Zilberstein, Karen Walrath, Dave Grundy, Darrell Schlicker, Neil Goldfine, Eugen Abramovici, and Tom Yentzer. Mwm eddy-current arrays for crack initiation and growth monitoring. *International Journal of Fatigue*, 25: 1147–1155, 2003. ISSN 0142-1123. doi: 10.1016/j.ijfatigue.2003.08.010.

[51] Philip May, Erping Zhou, and Danny Morton. The design of a ferrite-cored probe. *Sensors and Actuators A: Physical*, 136(1):221–228, 2007. ISSN 0924-4247. doi: 10.1016/j.sna.2006.11.031.

[52] X. Jian and S. Dixon. Enhancement of emat and eddy current using a ferrite back-plate. *Sensors and Actuators A: Physical*, 136(1):132–136, 2007. ISSN 0924-4247. doi: 10.1016/j.sna.2006.10.028.

[53] R. Huang, D. Zhang, and K. J. Tseng. Determination of dimension-independent magnetic and dielectric properties for mn-zn ferrite cores and its EMI applications. *Electromagnetic Compatibility, IEEE Transactions on*, 50(3):597–602, 2008. ISSN 0018-9375. doi: 10.1109/temc.2008.926914.

[54] Theodoros P. Theodoulidis. Model of ferrite-cored probes for eddy current nondestructive evaluation. *Journal of Applied Physics*, 93(5):3071, 2003. ISSN 00218979. doi: 10.1063/1.1543634.

[55] Hamid Baseri and Hoseyn Damirchi. Prediction of the ferrite-core probe performance using a neural network approach. *Materials and Manufacturing Processes*, 25(8):718–723, 2010. ISSN 1042-69141532-2475. doi: 10.1080/10426910903229370.

[56] Zhang Daming and Foo Chek Fok. A practical method to determine intrinsic complex permeabilities and permittivities for mn-zn ferrites. *Magnetics, IEEE Transactions on*, 41(4):1226–1232, 2005. ISSN 0018-9464. doi: 10.1109/tmag.2005.845916.

[57] Zeng Zhiwei, L. Udpa, and S. S. Udpa. Finite-element model for simulation of ferrite-core eddy-current probe. *Magnetics, IEEE Transactions on*, 46(3): 905–909, 2010. ISSN 0018-9464. doi: 10.1109/tmag.2009.2034651.

[58] Yi Lu, John R. Bowler, and Theodoros P. Theodoulidis. An analytical model of a ferrite-cored inductor used as an eddy current probe. *Journal of Applied Physics*, 111(10): 103907, 2012. doi: http://dx.doi.org/10.1063/1.4716189. URL `http://scitation.aip.org/content/aip/journal/jap/111/10/10.1063/1.4716189`.

[59] L. Janousek, K. Capova, N. Yusa, and K. Miya. Multiprobe inspection for enhancing sizing ability in eddy current nondestructive testing. *Magnetics, IEEE Transactions on*, 44(6):1618–1621, 2008. ISSN 0018-9464. doi: 10.1109/TMAG.2008.916547.

[60] H. Ramos, O. Postolache, F.C. Alegria, and A. Lopes Ribeiro. Using the skin effect to estimate cracks depths in mettalic structures. In *Instrumentation and Measurement Technology Conference, 2009. I2MTC 2009. IEEE*, pages 1361–1366, May 2009. doi: 10.1109/IMTC.2009.5168668.

[61] Noritaka Yusa, Yasutomo Sakai, and Hidetoshi Hashizume. An eddy current probe suitable to gain information about the depth of near-side flaws much deeper than the depth of penetration. *NDT & E International*, 44(1):121–130, 2011. ISSN 0963-8695. doi: 10.1016/j.ndteint.2010.10.003.

[62] V. Uchanin. Specific features of the space distribution of the signal of an eddy-current converter caused by cracks of different lengths. *Materials Science*, 43 (4):591–595, 2007. ISSN 1068-820X. doi: 10.1007/s11003-007-0068-2.

[63] B. A. Auld and J. C. Moulder. Review of advances in quantitative eddy current nondestructive evaluation. *Journal of Nondestructive Evaluation*, 18(1):3–36, 1999. ISSN 0195-9298. doi: 10.1023/a:1021898520626.

[64] Mun Ho-Young and Kim Chang-Eob. Comparison of characteristics of ect probes in detecting defects. In *Electrical Machines and Systems (ICEMS), 2011 International Conference on*, pages 1–6, 2011.

[65] Peng Xu, Songling Huang, and Wei Zhao. Differential eddy current testing sensor composed of double gradient winding coils for crack detection. In *Sensors Applications Symposium (SAS)*, pages 59–63. IEEE, 2010. ISBN 978-1-4244-4988-0. doi: 10.1109/SAS.2010.5439405.

[66] Xu Peng, Huang Songling, and Zhao Wei. Differential eddy current testing sensor composed of double gradient winding coils for crack detection. In *Sensors Applications Symposium (SAS), 2010 IEEE*, pages 59–63, 2010.

[67] S. K. Burke and R. J. Ditchburn. Mutual impedance of planar eddy-current driver pickup spiral coils. *Research in Nondestructive Evaluation*, 19(1):1–19, 2008. ISSN 0934-9847. doi: 10.1080/09349840701528341.

[68] Anders Rosell. Efficient finite element modelling of eddy current probability of detection with transmitterreceiver sensors. *{NDT} & E International*, 75:48 – 56, 2015. ISSN 0963-8695. doi: http://dx.doi.org/10.1016/j.ndteint.2015.07.001. URL `http://www.sciencedirect.com/science/article/pii/S0963869515000791`.

[69] Y. Choua, Santandre, x, L. a, Y. Le Bihan, and C. Marchand. Mesh refinement in eddy current testing with separated t-r probes. *Magnetics, IEEE Transactions on*, 46(8):2795–2798, 2010. ISSN 0018-9464.

[70] Haoyu Huang, Nozomu Sakurai, Toshiyuki Takagi, and Tetsuya Uchimoto. Design of an eddy-current array probe for crack sizing in steam generator tubes. *NDT & E International*, 36(7):515–522, 2003. ISSN 0963-8695. doi: 10.1016/s0963-8695(03)00050-1.

[71] A. Zaoui, H. Menana, M. Feliachi, and G. Berthiau. Inverse problem in non-destructive testing using arrayed eddy current sensors. *Sensors (Basel)*, 10 (9):8696–8704, 2010. ISSN 1424-8220 (Electronic) 1424-8220 (Linking). doi: 10.3390/s100908696. Basel, Switzerland Sensors (Basel). 2010;10(9):8696-8704. Epub 2010 Sep 20.

[72] Xianglin Chen and Tianhuai Ding. Flexible eddy current sensor array for proximity sensing. *Sensors and Actuators A: Physical*, 135(1):126–130, 2007. ISSN 0924-4247. doi: 10.1016/j.sna.2006.06.056.

[73] A. Nishimizu, H. Endo, M Tooma, K. Otani, Ouchi. H., I. Yoshida, and Y. Nonaka. Non-destructive examination using a flexible multi-coil eddy current probe for weld surfaces of core internal components of nuclear power plants. *Insight*, 54(3):134–137, 2012.

[74] Ze Liu, Lixiong Zhu, Shengwei Ren, A. Koffman, B.C. Waltrip, and Yicheng Wang. Electromagnetic rail inspection using ac bridge measurements. In *Precision Electromagnetic Measurements (CPEM), 2012 Conference on*, pages 724–725, July 2012. doi: 10.1109/CPEM.2012.6251134.

[75] R.S. Sharpe. *Research techniques in nondestructive testing*. Academic Press, 1982. ISBN 9780126390551.

[76] Z. Liu, K. Tsukada, K. Hanasaki, and M. Kurisu. Two-dimensional eddy current signal enhancement via multifrequency data fusion. *Research in Nondestructive Evaluation*, 11(3):165–177, 1999. ISSN 0934-9847. doi: 10.1007/pl00003919.

[77] K. A. Bartels and J. L. Fisher. Multifrequency eddy current image processing techniques for nondestructive evaluation. In *Image Processing, 1995. Proceedings., International Conference on*, volume 1, pages 486–489vol.1, 1995. doi: 10.1109/icip.1995.529752.

[78] Liu Zheng, D. S. Forsyth, J. P. Komorowski, K. Hanasaki, and T. Kirubarajan. Survey: State of the art in nde data fusion techniques. *Instrumentation and Measurement, IEEE Transactions on*, 56(6):2435–2451, 2007. ISSN 0018-9456. doi: 10.1109/tim.2007.908139.

[79] T. Chady and R. Sikora. Optimization of eddy-current sensor for multifrequency systems. *Magnetics, IEEE Transactions on*, 39(3):1313–1316, 2003. ISSN 0018-9464. doi: 10.1109/tmag.2003.810412.

[80] Yiming Deng and Xin Liu. Electromagnetic imaging methods for nondestructive evaluation applications. *Sensors*, 11(12):11774–11808, 2011. ISSN 1424-8220. doi: 10.3390/s111211774.

[81] Pei Xiao-Mei, Liang Hong-Sheng, and Qiao Yong-Ming. A frequency spectrum analysis method for eddy current nondestructive testing. In *Machine Learning and Cybernetics, 2002. Proceedings. 2002 International Conference on*, volume 3, pages 1194–1197vol.3, 2002. doi: 10.1109/icmlc.2002.1167389.

[82] Giovanni Betta, Luigi Ferrigno, Marco Laracca, Pietro Burrascano, Marco Ricci, and Giuseppe Silipigni. An experimental comparison of multi-frequency and chirp excitations for eddy current testing on thin defects. *Measurement*, 63:207 – 220, 2015. ISSN 0263-2241. doi: http://dx.doi.org/10.1016/j.measurement.2014.12.015. URL `http://www.sciencedirect.com/science/article/pii/S0263224114006125`.

[83] L. A. Williams, S. E. Faidi, S. B. Lyon, R. A. Cottis, and K. R. Baldwin. Non-destructive testing using electromagnetic impedance spectroscopy. *Corrosion Science*, 35(14):833–839, 1993. ISSN 0010-938X. doi: 10.1016/0010-938x(93)90222-3.

[84] W Yin, S J Dickinson, and A J Peyton. A multi-frequency impedance analysing instrument for eddy current testing. *Mea-*

*surement Science and Technology*, 17(2):393, 2006. URL http://stacks.iop.org/0957-0233/17/i=2/a=022.

[85] S. Giguare, B. A. Lepine, and J. M. S. Dubois. Pulsed eddy current technology: Characterizing material loss with gap and lift-off variations. *Research in Nondestructive Evaluation*, 13(3):119–129, 2001. ISSN 0934-9847. doi: 10.1080/09349840109409692. URL http://dx.doi.org/10.1080/09349840109409692.

[86] M.S. Safizadeh, B.A. Lepine, D.S. Forsyth, and A. Fahr. Time-frequency analysis of pulsed eddy current signals. *Journal of Nondestructive Evaluation*, 20(2):73–86, 2001. ISSN 0195-9298. doi: 10.1023/A:1012244208475. URL http://dx.doi.org/10.1023/A%3A1012244208475.

[87] Gui Yun Tian and Ali Sophian. Reduction of lift-off effects for pulsed eddy current ndt. *NDT & E International*, 38(4):319–324, 2005. ISSN 0963-8695. doi: 10.1016/j.ndteint.2004.09.007.

[88] Tian Gui Yun, Li Yong, and C. Mandache. Study of lift-off invariance for pulsed eddy-current signals. *Magnetics, IEEE Transactions on*, 45(1):184–191, 2009. ISSN 0018-9464. doi: 10.1109/tmag.2008.2006246.

[89] Ilham Zainal Abidin, Catalin Mandache, Gui Yun Tian, and Maxim Morozov. Pulsed eddy current testing with variable duty cycle on rivet joints. *NDT & E International*, 42(7):599–605, 2009. ISSN 0963-8695. doi: 10.1016/j.ndteint.2009.04.001.

[90] J. Bowler and M. Johnson. Pulsed eddy-current response to a conducting half-space. *Magnetics, IEEE Transactions on*, 33(3):2258–2264, May 1997. ISSN 0018-9464. doi: 10.1109/20.573841.

[91] M. Gibbs and J. Campbell. Pulsed eddy-current inspection of cracks under installed fasteners. *Materials Evaluation*, 49(1):51–&, 1991. ISSN 0025-5327.

ISI Document Delivery No.: ER254 Times Cited: 13 Cited Reference Count: 0 Gibbs, m campbell, j Amer soc non-destructive test Columbus.

[92] B. F. Yang, F. L. Luo, and D. Han. Pulsed eddy current technique used for non-destructive inspection of ageing aircraft. *Insight*, 48(7):411–414, 2006. ISSN 1354-2575. doi: 10.1784/insi.2006.48.7.411.

[93] J. Zhang, W. J. Kim, M. Yuan, H. J. Kim, S. J. Song, C. W. Lee, and J. D. Chung. Analytical approach to pulsed eddy current nondestructive evaluation of multilayered conductive structures. *Journal of Mechanical Science and Technology*, 26(12):3953–3958, 2012. ISSN 1738-494X. doi: 10.1007/s12206-012-0911-8.

[94] Yunze He, Feilu Luo, Mengchun Pan, Feibing Weng, Xiangchao Hu, Junzhe Gao, and Bo Liu. Pulsed eddy current technique for defect detection in aircraft riveted structures. *NDT & E International*, 43(2):176–181, 2010. ISSN 0963-8695. doi: 10.1016/j.ndteint.2009.10.010.

[95] J. S. R. Giguere, B. A. Lepine, and J. M. S. Dubois. *Detection of cracks beneath rivet heads via pulsed eddy current technique*, volume 615 of *Aip Conference Proceedings*, pages 1968–1975. Amer Inst Physics, Melville, 2002. ISBN 0094-243X 0-7354-0061-X. ISI Document Delivery No.: BU96R Times Cited: 1 Cited Reference Count: 11 Giguere, JSR Lepine, BA Dubois, JMS Proceedings Paper 28th Annual Conference on Quantitative Nondestructive Evaluation Jul 29-aug 03, 2001 Brunswick, me 2 huntington quadrangle, ste 1no1, melville, ny 11747-4501 usa.

[96] D.P.R. Desjardins, T.W. Krause, and N. Gauthier. Analytical modeling of the transient response of a coil encircling a ferromagnetic conducting rod in pulsed eddy current testing. {*NDT*} *& E International*, 60:127 – 131, 2013.

ISSN 0963-8695. doi: http://dx.doi.org/10.1016/j.ndteint.2013.07.007. URL `http://www.sciencedirect.com/science/article/pii/S0963869513001084`.

[97] D.R. Desjardins, T.W. Krause, A. Tetervak, and L. Clapham. Concerning the derivation of exact solutions to inductive circuit problems for eddy current testing. *NDT & E International*, 68(0):128–135, 2014. ISSN 0963-8695. doi: 10.1016/j.ndteint.2014.07.008.

[98] J.R. Klauder, A.C. Price, S. Darlington, and W.J. Albersheim. The theory and design of chirp radars. *Bell System Technical Journal, The*, 39(4):745–808, July 1960. ISSN 0005-8580. doi: 10.1002/j.1538-7305.1960.tb03942.x.

[99] M. Pollakowski and Helmut Ermert. Chirp signal matching and signal power optimization in pulse-echo mode ultrasonic nondestructive testing. *Ultrasonics, Ferroelectrics, and Frequency Control, IEEE Transactions on*, 41(5):655–659, Sept 1994. ISSN 0885-3010. doi: 10.1109/58.308500.

[100] Y. Shen, C. Lee, C. C. H. Lo, N. Nakagawa, and A. M. Frishman. Conductivity profile determination by eddy current for shot-peened superalloy surfaces toward residual stress assessment. *Journal of Applied Physics*, 101(1):014907, 2007. doi: http://dx.doi.org/10.1063/1.2403970. URL `http://scitation.aip.org/content/aip/journal/jap/101/1/10.1063/1.2403970`.

[101] Nenad Novkovski. *Progress and Limitations In Magnetic Field Measurements, Geomagnetics for Aeronautical Safety*, volume 13 of *NATO Security through Science Series*, pages 201–212. Springer Netherlands, 2006. ISBN 978-1-4020-5023-7. doi: 10.1007/978-1-4020-5025-1-15.

[102] D. F. He, M. Tachiki, and H. Itozaki. Highly sensitive anisotropic magnetoresistance magnetometer for eddy-current nondestructive evaluation. *Review of Scientific Instruments*, 80(3):

036102, 2009. doi: http://dx.doi.org/10.1063/1.3098946. URL http://scitation.aip.org/content/aip/journal/rsi/80/3/10.1063/1.3098946.

[103] Nathan A. Stutzke, Stephen E. Russek, David P. Pappas, and Mark Tondra. Low-frequency noise measurements on commercial magnetoresistive magnetic field sensors. *Journal of Applied Physics*, 97 (10):10Q107, 2005. doi: http://dx.doi.org/10.1063/1.1861375. URL http://scitation.aip.org/content/aip/journal/jap/97/10/10.1063/1.1861375.

[104] Albrecht Jander, Carl Smith, and Robert Schneider. Magnetoresistive sensors for nondestructive evaluation. In *Nondestructive Evaulation for Health Monitoring and Diagnostics*, pages 1–13. International Society for Optics and Photonics, 2005.

[105] C. H. Smith, R. W. Schneider, T. Dogaru, and S. T. Smith. GMr magnetic sensor arrays for nde eddy-current testing. *AIP Conference Proceedings*, 657 (1):419–426, 2003.

[106] T. Dogaru and S. T. Smith. Giant magnetoresistance-based eddy-current sensor. *Magnetics, IEEE Transactions on*, 37(5):3831–3838, 2001. ISSN 0018-9464. doi: 10.1109/20.952754.

[107] J.R. Hook and H.E. Hall. *Solid State Physics*. Manchester Physics Series. Wiley, 2013. ISBN 9781118790885. URL https://books.google.co.uk/books?id=1ageAAAAQBAJ.

[108] M. v Kreutzbruck, K. Allweins, T. Ruhl, M. Muck, C. Heiden, H. J. Krause, and R. Hohmann. Defect detection and classification using a squid based multiple frequency eddy current nde system. *Applied Superconductivity, IEEE Transactions on*, 11(1):1032–1037, 2001. ISSN 1051-8223. doi: 10.1109/77.919525.

[109] Nestor G. Sepulveda, Daniel J. Staton, and John P. Wikswo. A mathematical analysis of the magnetic field produced by flaws in two-dimensional current-carrying conductors. *Journal of Nondestructive Evaluation*, 11(2):89–101, 1992. ISSN 0195-9298. doi: 10.1007/bf00568292.

[110] David Jeffery Griffiths. *Introduction to electrodynamics*. Prentice Hall, 1999. ISBN 9780138053260.

[111] Mohammadreza Sadeghi and Mohamed Missous. Highly sensitive ingaas-algaas-gaas 2deg quantum well hall effect integrated circuits. In *11th European Conference on Non-Destructive Testing (ECNDT 2014)*, 2014.

[112] M Behet, J Bekaert, J De Boeck, and G Borghs. Inas/al0.2ga0.8sb quantum well hall effect sensors. *Sensors and Actuators A: Physical*, 81(13):13 – 17, 2000. ISSN 0924-4247. doi: http://dx.doi.org/10.1016/S0924-4247(99)00162-4. URL `http://www.sciencedirect.com/science/article/pii/S0924424799001624`.

[113] R.R. Boyer. Titanium for aerospace: Rationale and applications. *Advanced Performance Materials*, 2(4):349–368, 1995. ISSN 0929-1881. doi: 10.1007/BF00705316. URL `http://dx.doi.org/10.1007/BF00705316`.

[114] R.W. Messler and R.W. Messler. *The Essence of Materials for Engineers*. Jones & Bartlett Learning, 2010. ISBN 9780763778330. URL `https://books.google.co.uk/books?id=VN9BTDdOLYcC`.

[115] G.T. Meaden. *Electrical resistance of metals*. International cryogenics monograph series. Plenum Press, 1965. URL `https://books.google.co.uk/books?id=my5RAAAAMAAJ`.

[116] Mark Blodgett and Peter B Nagy. Anisotropic grain noise in eddy current inspection of noncubic polycrystalline metals. *Applied physics letters*, 72(9): 1045–1047, 1998.

[117] Robert Pederson. *Microstructure and Phase Transformation of Ti-6Al-4V*. PhD thesis, Lulea University of Technology, 2002.

[118] M. P. Blodgett and P. B. Nagy. The role of grain noise in eddy current inspection of titanium alloys. In *Symposium JJ Nondestructive Characterization of Materials in Aging Systems*, volume 503 of *MRS Proceedings*, 1997. doi: 10.1557/PROC-503-53. URL http://0-journals.cambridge.org.pugwash.lib.warwick.ac.uk/article_S19464274002

[119] Matthew R. Cherry, Shamachary Sathish, Adam L. Pilchak, Aaron J. Cherry, and Mark P. Blodgett. Characterization of microstructure with low frequency electromagnetic techniques. *AIP Conference Proceedings*, 1581(1):1456–1462, 2014. doi: http://dx.doi.org/10.1063/1.4864993. URL http://scitation.aip.org/content/aip/proceeding/aipcp/10.1063/1.4864993.

[120] M. P. Blodgett and P. B. Nagy. Eddy current assessment of near-surface residual stress in shot-peened nickel-base superalloys. *Journal of Nondestructive Evaluation*, 23(3):107–123, 2004. ISSN 0195-9298. doi: 10.1023/B:JONE.0000048866.40648.fe.

[121] Mark Blodgett, Waled Hassan, and Peter B Nagy. Theoretical and experimental investigations of the lateral resolution of eddy current imaging. *Materials evaluation*, 58(5):647–654, 2000.

[122] B. Sasi, B. Rao, T. Jayakumar, and Baldev Raj. Characterisation of solution annealed vt-14 titanium alloy using eddy current based electrical resistivity measurements. *Transactions of the Indian Institute of Metals*, 63(5):773–777, 2010. ISSN 0972-2815. doi: 10.1007/s12666-010-0118-6.

[123] J. White. *An Introduction to RF and Microwave Engineering,*. High Frequency Techniques. [Piscataway, N.J.?] : Hoboken, N.J.: IEEE Press ; Wiley-Interscience, 2004, 2004.

[124] Nathan Ida and JoÃ£o Bastos. *Electromagnetics and calculation of fields*. Springer, 1997. ISBN 9780387948775.

[125] L.B. Felsen and N. Marcuvitz. *Radiation and Scattering of Waves*. IEEE Press Series on Electromagnetic Wave Theory. Wiley, 1994. ISBN 9780780310889. URL `https://books.google.co.uk/books?id=GR71VojdFdQC`.

[126] C. V. Dodd and W. E. Deeds. Analytical solutions to eddy-current probe-coil problems. *Journal of Applied Physics*, 39(6):2829–2838, 1968.

[127] Robert A Smith, Geoffrey R Hugo, and David J Harrison. Essential factors in improving the characterization of cracks and corrosion using transient eddy currents. In *Proc 6th Joint FAA/NASA/DoD Conf on Aging Aircraft, San Francisco*, 2002.

[128] A.M. Urling, V.A. Niemela, G.R. Skutt, and T.G. Wilson. Characterizing high-frequency effects in transformer windings-a guide to several significant articles. In *Applied Power Electronics Conference and Exposition, 1989. APEC' 89. Conference Proceedings 1989., Fourth Annual IEEE*, pages 373–385, Mar 1989. doi: 10.1109/APEC.1989.36989.

[129] P.L. Dowell. Effects of eddy currents in transformer windings. *Electrical Engineers, Proceedings of the Institution of*, 113(8):1387–1394, August 1966. ISSN 0020-3270. doi: 10.1049/piee.1966.0236.

[130] A. Reatti and M.K. Kazimierczuk. Comparison of various methods for calculating the ac resistance of inductors. *Magnetics, IEEE Transactions on*, 38 (3):1512–1518, May 2002. ISSN 0018-9464. doi: 10.1109/20.999124.

[131] Xi Nan and C.R. Sullivan. An improved calculation of proximity-effect loss in high-frequency windings of round conductors. In *Power Electronics Specialist Conference, 2003. PESC '03. 2003 IEEE 34th Annual*, volume 2, pages 853–860 vol.2, June 2003. doi: 10.1109/PESC.2003.1218168.

[132] A. Danisi, A. Masi, R. Losito, and Y. Perriard. Modeling of high-frequency electromagnetic effects on an ironless inductive position sensor. *Sensors Journal, IEEE*, 13(12):4663–4670, Dec 2013. ISSN 1530-437X. doi: 10.1109/JSEN.2013.2271546.

[133] M. Bartoli, N. Noferi, A. Reatti, and M.K. Kazimierczuk. Modeling litz-wire winding losses in high-frequency power inductors. In *Power Electronics Specialists Conference, 1996. PESC '96 Record., 27th Annual IEEE*, volume 2, pages 1690–1696 vol.2, Jun 1996. doi: 10.1109/PESC.1996.548808.

[134] John R. Bowler, Stephen J. Norton, and David J. Harrison. Eddy-current interaction with an ideal crack. ii. the inverse problem. *Journal of Applied Physics*, 75(12):8138–8144, 1994.

[135] Stephen J. Norton and John R. Bowler. Theory of eddy current inversion. *Journal of Applied Physics*, 73(2):501–512, 1993. doi: 10.1063/1.353359.

[136] Q. M. Jiang, C. H. Chen, and L. P. Khoo. Analytical algorithm of inductive field for realising a smart eddy current ndt system. *Engineering Computations*, 20(7-8):835–854, 2003. ISSN 0264-4401. doi: 10.1080/02644400310502009.

[137] Theodoros P. Theodoulidis and Epameinondas E. Kriezis. Impedance evaluation of rectangular coils for eddy current testing of planar media. *NDT & E International*, 35(6):407–414, 2002. ISSN 0963-8695. doi: 10.1016/s0963-8695(02)00008-7.

[138] Theodoros Theodoulidis and Epameinondas Kriezis. Series expansions in eddy current nondestructive evaluation models. *Journal of Materials Processing Technology*, 161(12):343 – 347, 2005. ISSN 0924-0136. doi: http://dx.doi.org/10.1016/j.jmatprotec.2004.07.048. URL `http://www.sciencedirect.com/science/article/pii/S0924013604009410`.

3rd Japenese-Mediterranean Workshop on Applied Electromagnetic Engineering for Magnetic and Superconducting Materials and 3rd Workshop on Superconducting Flywheels.

[139] Theodoros Theodoulidis, Nikolaos Poulakis, and Athanasios Dragogias. Rapid computation of eddy current signals from narrow cracks. *NDT & E International*, 43(1):13–19, 2010. ISSN 09638695. doi: 10.1016/j.ndteint.2009.08.005.

[140] Antonio Massarini and Marian K Kazimierczuk. Self-capacitance of inductors. *Power Electronics, IEEE Transactions on*, 12(4):671–676, 1997.

[141] Gabriele Grandi, Marian K Kazimierczuk, Antonio Massarini, and Ugo Reggiani. Stray capacitances of single-layer solenoid air-core inductors. *Industry Applications, IEEE Transactions on*, 35(5):1162–1168, 1999.

[142] A.B. Williams and F.J. Taylor. *Electronic Filter Design Handbook,*. McGraw-Hill, 1995. ISBN 9780070704411.

[143] R.W.P. King. *Transmission-line theory,*. McGraw-Hill, 1955.

[144] D.M. Pozar. *Microwave Engineering,*. Wiley, 1997. ISBN 9780471170969.

[145] P. Holmberg, M. Leijon, and Torbjorn Wass. A wideband lumped circuit model of eddy current losses in a coil with a coaxial insulation system and a stranded conductor. *Power Delivery, IEEE Transactions on*, 18(1):50–60, Jan 2003. ISSN 0885-8977. doi: 10.1109/TPWRD.2002.803753.

[146] F.E. Terman. *Radio engineer's handbook*. McGraw-Hill Book Company, inc., 1943. URL `https://books.google.co.uk/books?id=b7Q8AAAAIAAJ`.

[147] C. N. Owston. A high frequency eddy-current, non-destructive testing apparatus with automatic probe positioning suitable for scanning applications. *Journal of Physics E-Scientific Instruments*, 3(10):814–&, 1970. ISSN 0022-3735. doi: 10.1088/0022-3735/3/10/317.

[148] Cunyue Liu and Yonggui Dong. Resonant enhancement of a passive coil-capacitance loop in eddy current sensing path. *Measurement*, 45(3):622–626, 2012. ISSN 0263-2241. doi: 10.1016/j.measurement.2011.12.006.

[149] B.I. Bleaney. *Electricity and Magnetism*. Oxford University Press, 1976. ISBN 9780198511410.

[150] C. N. Owston. Eddy-current testing at microwave frequencies. *Non-Destructive Testing*, 2(3):193–196, 1969. ISSN 0029-1021. doi: 10.1016/0029-1021(69)90111-x.

[151] Liu Bo, Luo Feilu, Jin Zhongqing, and Liu Jiali. Eddy current array instrument and probe for crack detection of aircraft tubes. In *Intelligent Computation Technology and Automation (ICICTA), 2010 International Conference on*, volume 2, pages 177–180, May 2010. doi: 10.1109/ICICTA.2010.85.

[152] Gerhard Mook, Fritz Michel, and Jouri Simonin. Electromagnetic imaging using probe arrays. *Strojniški vestnik-Journal of Mechanical Engineering*, 57 (3):227–236, 2011.

[153] G. Grubb. Discussions with rr level iii eddy current engineer, 2015.

[154] C. Annis. *Nondestructive Evaluation System Reliability Assessment*, 1999.

[155] Rolls-Royce. Rrp 58000 - control of ndt. Technical report, Rolls-Royce, 1999.

[156] Xuezhe Wei, Zhenshi Wang, and Haifeng Dai. A critical review of wireless power transfer via strongly coupled magnetic resonances. *Energies*, 7(7):4316–4341, 2014.

[157] Ray T Ko, Mark P Blodgett, Shamachary Sathish, and Thomas R Boehnlein. Resonant frequency eddy current liftoff measurements for shot peening intensity assessment in materials (preprint). Report, DTIC Document, 2007.

[158] R. T. Ko, M. P. Blodgett, S. Sathish, and T. R. Boehnlein. *Application of resonant frequency eddy current technique on a shot-peened nickel-based engine-grade material*, volume 894 of *Aip Conference Proceedings*, pages 1608–1615. Amer Inst Physics, Melville, 2007. ISBN 0094-243X 978-0-7354-0399-4.

[159] C. Y. Liu and Y. G. Dong. Resonant coupling of a passive inductance-capacitance-resistor loop in coil-based sensing systems. *Ieee Sensors Journal*, 12(12):3417–3423, 2012. ISSN 1530-437X. doi: 10.1109/jsen.2012.2190057.

[160] G.W.C. Kaye and T.H. Laby. *Tables of Physical and Chemical Constants*. Longman, 1995. ISBN 9780582226296. URL `https://books.google.co.uk/books?id=c_VQAAAAMAAJ`.

[161] J. Anudev and I.J. Raglend. Analytical study of howland current source model. In *Computing, Electronics and Electrical Technologies (ICCEET), 2012 International Conference on*, pages 314–318, March 2012. doi: 10.1109/ICCEET.2012.6203843.

[162] A.S. Tucker, R.M. Fox, and R.J. Sadleir. Biocompatible, high precision, wideband, improved howland current source with lead-lag compensation. *Biomedical Circuits and Systems, IEEE Transactions on*, 7(1):63–70, Feb 2013. ISSN 1932-4545. doi: 10.1109/TBCAS.2012.2199114.

[163] F Adamo, F Attivissimo, M Marracci, and B Tellini. Characterization of a system for measurements on soft ferrites. *Measurement Science and Technology*, 23(8):085602, 2012. URL `http://stacks.iop.org/0957-0233/23/i=8/a=085602`.

[164] G.D. Hammond, C.C. Speake, and M. Stiff. Noise analysis of a howland current source. *International Journal of Electronics*, 95(4):351–359, 2008. doi: 10.1080/00207210801976503. URL `http://dx.doi.org/10.1080/00207210801976503`.

[165] R. Hughes and S. Dixon. Near electrical resonance signal enhancement (nerse) for sub-millimetre detection in aerospace superalloys. *International Journal of Aerospace and Lightweight Structures (IJALS)*, 4(2):107–120, 2014. doi: 10.3850/S2010428615100096.

[166] R.R. Boyer. An overview on the use of titanium in the aerospace industry. *Materials Science and Engineering: A*, 213(12):103 – 114, 1996. ISSN 0921-5093. doi: http://dx.doi.org/10.1016/0921-5093(96)10233-1. URL `http://www.sciencedirect.com/science/article/pii/0921509396102331`. International Symposium on Metallurgy and Technology of Titanium Alloys.

[167] Richard J Smith, Wenqi Li, Jethro Coulson, Matt Clark, Michael G Somekh, and Steve D Sharples. Spatially resolved acoustic spectroscopy for rapid imaging of material microstructure and grain orientation. *Measurement Science and Technology*, 25(5):055902, 2014. URL `http://stacks.iop.org/0957-0233/25/i=5/a=055902`.

[168] Steve D. Sharples, Matthew Clark, and Mike G. Somekh. Spatially resolved acoustic spectroscopy for fast noncontact imaging of material microstructure. *Opt. Express*, 14(22): 10435–10440, Oct 2006. doi: 10.1364/OE.14.010435. URL `http://www.opticsexpress.org/abstract.cfm?URI=oe-14-22-10435`.

[169] A. Tamburrino and G. Rubinacci. Fast methods for quantitative eddy-current tomography of conductive materials. *Magnetics, IEEE Transactions on*, 42 (8):2017–2028, Aug 2006. ISSN 0018-9464. doi: 10.1109/TMAG.2006.877542.

[170] E. E. Gdoutos and G. Papakaliatakis. *Crack Growth in Three-Point Bend Specimens Made of Polymeric Foams*, volume 9999 of *Conference Proceedings of the Society for Experimental Mechanics Series*, book section 14, pages 99–

105. Springer New York, 2011. ISBN 978-1-4614-0221-3. doi: 10.1007/978-1-4614-0222-0-14.

[171] G.A. Georgiou. Probability of detection (pod) curves: Derivation, applications and limitations. *Health & Safety Executive Books*, Research Report(454), 2006.

[172] Shannon R Bowling, Mohammad T Khasawneh, Sittichai Kaewkuekool, and Byung Rae Cho. A logistic approximation to the cumulative normal distribution. *Journal of Industrial Engineering and Management*, 2(1):114–127, 2009.

[173] L.C. Andrews. *Special Functions of Mathematics for Engineers*. Oxford science publications. SPIE Optical Engineering Press, 1992. ISBN 9780819426161. URL `https://books.google.co.uk/books?id=2CAqsF-RebgC`.

[174] Alan P Berens. Nde reliability data analysis. *ASM Handbook.*, 17:689–701, 1989.